Project no.:	101095738		
Project full title:	6G Short range extreme communication IN Entities		
Project Acronym:	6G-SHINE		
Project start date:	01/03/2023	**Duration**	30 months

D3.4 RIS MANAGEMENT STRATEGIES FOR IN-X SUBNETWORKS

Due date	30/6/2025	**Delivery date**	30/06/2025
Work package	WP3		
Responsible Author(s)	Davide Dardari (CNIT)		
Contributor(s)	Filipe Conceicao (IDE), Davide Dardari (CNIT), Vittorio Degli Esposti (CNIT), Andrea Abrardo (CNIT), Fredrik Rusek (SONY), Enrico Maria Vitucci (CNIT)		
Version	V1.0		
Reviewer(s)	Fotis Foukalas (COGN), Gilberto Berardinelli (AAU)		
Dissemination level	Public		

Co-funded by the European Union

Horizon Europe Grant Agreement No. 101095738. Views and opinions expressed are however those of the author(s) only and do not necessarily reflect those of the European Union or SNS JU. Neither the European Union nor the granting authority can be held responsible for them.

VERSION AND AMENDMENT HISTORY

Version	Date (MM/DD/YYYY)	Created/Amended by	Changes
0.1	12/10/2024	D. Dardari	TOC started/finalization
0.2	03/03/2025	F. Conceicao, F. Rusek, E. Vitucci, V. Degli Esposti	Initial contributions from partners
0.3	15/03/2025	D. Dardari	Editor revision and feedback
0.4	02/05/2025	D. Dardari, F. Conceicao, F. Rusek	Editor review completed
0.5	19/05/2025	D. Dardari	Version ready for internal review
0.6	30/05/2025	Fotis Foukalas, Gilberto Berardinelli	Feedback from the internal reviewers
0.7	19/6/2025	D. Dardari	Minor updates
0.9	27/06/2025	Berit H. Christensen	Final proofreading and layout check
1.0	30/06/2025	D. Dardari	Submitted version

TABLE OF CONTENTS

FIGURES

TABLES

ABBREVIATIONS

Abbreviation	Meaning
3GPP	3rd Generation Partnership Project
AC	Access point
ARSB	Anomalous Reflection Shadow Boundary
AO	Alternating optimization
ATSB	Anomalous Transmission Shadow Boundary
BLER	Block error rate
BS	Base station
CSI	Channel state information
DL	Downlink
DR	directional cosines
DMA	Dynamic metasurface antenna
EM	Electromagnetic
FDMA	Frequency division multiple access
FiRa	Fine Ranging Alliance
GO	Geometrical optics
FPC	Flexible packet coding
HC	High capability
JCPC	Joint Channel and Packet Coding
LC	Low capability
LDPC	Low-Density Parity-Check
LOS	Line of sight
i.i.d.	Independent identically distributed
ISB	Incidence Shadow Boundary
MAC	Medium access control
MCS	Modulation coding scheme
MIMO	Multiple-input multiple-output
MMSE	Minimum mean square error
NC	Network coding
NCR	Network controller repeater
NLOS	Non-line of sight
KPI	Key performance indicator
KVI	Key value indicator
PDU	Protocol data unit
PHY	Physical layer
PO	Physical optics
P-RIS	Permuted RIS
PUSH	Physical uplink shared channel
QoS	Quality of service
RIS	Reconfigurable intelligent surfaces
RSSI	Received signal strength indicator
RSRQ	Reference Signal Received Quality
RSRP	Reference Signals Received Power
SAW	Surface Acoustic Wave
SDU	Service data unit

SMD	Spatial modulated dyadic
SNE	Subnetwork element
SNR	Signal to noise ratio
SINR	Signal to interference-noise ratio
SoA	State of the art
SOCP	Second order cone programming
TC	Technology component
TDD	Time division duplexing
UE	User equipment
UL	Uplink
UTD	Uniform geometrical theory of diffraction
UWB	Ultrawide bandwidth

EXECUTIVE SUMMARY

This deliverable reports the activities carried out in the second period of the project, as planned in Task 3.3 "Reconfigurable intelligent surfaces", by extending the preliminary investigations described in the preceding deliverable D3.2 "*RIS technologies and models for In-X subnetworks*" [1] which was mainly focused on presenting a survey and classification of available and under-study reconfigurable intelligent surfaces (RIS) technologies, and the main models used to characterize and design them. It also presented a preliminary analysis of the main design issues and the promising RIS technologies for the use cases defined in WP2 and hence the potential impact of their deployment in subnetworks in terms of key performance indicators (KPIs), key value indicators (KVIs), and standardization. This analysis has served as a foundational reference for the subsequent research activity aimed at developing RIS-aided PHY/MAC methods and RIS optimization algorithms, specific for subnetworks, which are described in this deliverable.

In the 6G-SHINE project, two general scenarios typical of subnetworks supported by RISs have been addressed. The first scenario focuses on improving communications within a single subnetwork. Here, the aim is to reduce the overall transmitted power while ensuring the required transmission rates, all with minimal overhead for channel state information (CSI) signalling and reduced intra-subnetwork interference. This is achieved by leveraging one or more RISs to assist communication within the subnetwork. The second scenario deals with the coexistence of adjacent subnetworks, which can either be coordinated or uncoordinated, each also aided by RISs. In this case, the challenge lies in mitigating the interference caused by unintended signal reflections from RISs positioned in neighbouring subnetworks. For example, while an RIS in one subnetwork may be configured to reflect signals toward a specific user, it could inadvertently reflect signals originating from another subnetwork in unintended directions, thereby creating interference for other users within the first subnetwork.

To tackle these challenges, 6G-SHINE introduced advanced RIS models based on multi-port theory, which were subsequently used for RIS optimization and performance analyses. Additionally, macroscopic ray-based models for RIS behaviour were defined and validated through experimental measurement campaigns. The project also explored novel RIS structures, particularly non-diagonal RIS configurations, which offer greater flexibility in managing interference, alongside designs capable of forming wide beams.

Further efforts included developing optimization strategies aimed at minimizing power consumption while meeting data rate constraints, even in the presence of multiple conventional RISs and multiple users. Complementary to this, flexible packet coding techniques were investigated to enhance the reliability of communication links. The project also examined methods for reducing inter-subnetwork interference, either through non-diagonal RIS configurations or by introducing some degree of coordination between neighbouring subnetworks.

Moreover, during this work on RIS technologies and signal processing methods, one partner discovered an unexpected double beamforming effect when combining RISs with ultrawideband (UWB) signals. Initially considered a potential issue, this effect was successfully transformed into a useful feature through careful engineering, offering additional opportunities, particularly in consumer-oriented applications.

1 INTRODUCTION

Many key performance indicators (KPIs) needed to realize wireless subnetworks capable of supporting next-generation applications in industrial, consumer, and vehicular scenarios, as identified in WP2 (see Deliverable D2.2 [2]) can be approached only through a sufficiently dense deployment of radio access points (APs) or base stations (BSs), i.e., high capability (HC) nodes. Examples are coverage (i.e., spatial and temporal availability) and reliability to non-line-of-sight (NLOS) propagation conditions. Unfortunately, this is often in contrast with other KPIs/KVIs such as energy efficiency, scalability, latency, and complexity which might be particularly critical in subnetworks.
Reconfigurable intelligent surface (RIS) is an emerging technology whose main purpose is to replace active devices such as APs and BSs, and hence HC nodes, with electromagnetically passive devices characterized by extremely low-power consumption, complexity and that do not generate additional "electromagnetic pollution".
Despite the initial enthusiasm of the scientific community for RISs, fostered by early promising results, later research realized that a complete understanding of the implications of the introduction of RIS technology in specific scenarios was necessary before assessing their advantages and disadvantages.
In fact, many effects have been often overlooked, mainly because of the oversimplified models adopted in the analysis, that might be detrimental, especially in subnetworks where coordination between them is not always guaranteed. Examples are given by the uncontrolled additional interference caused by RISs both within a subnetwork and between subnetworks, and the additional overhead necessary to manage the RIS configuration. That calls for improved and validated physically consistent models for RIS, the design of optimization strategies including them characterized by low overhead and low power consumption, the design of novel RIS structures capable of providing the required configuration flexibility to enhance the coexistence. At the same time, the presence of RIS can be exploited by ad hoc methods to improve communication reliability such as those based on network coding.

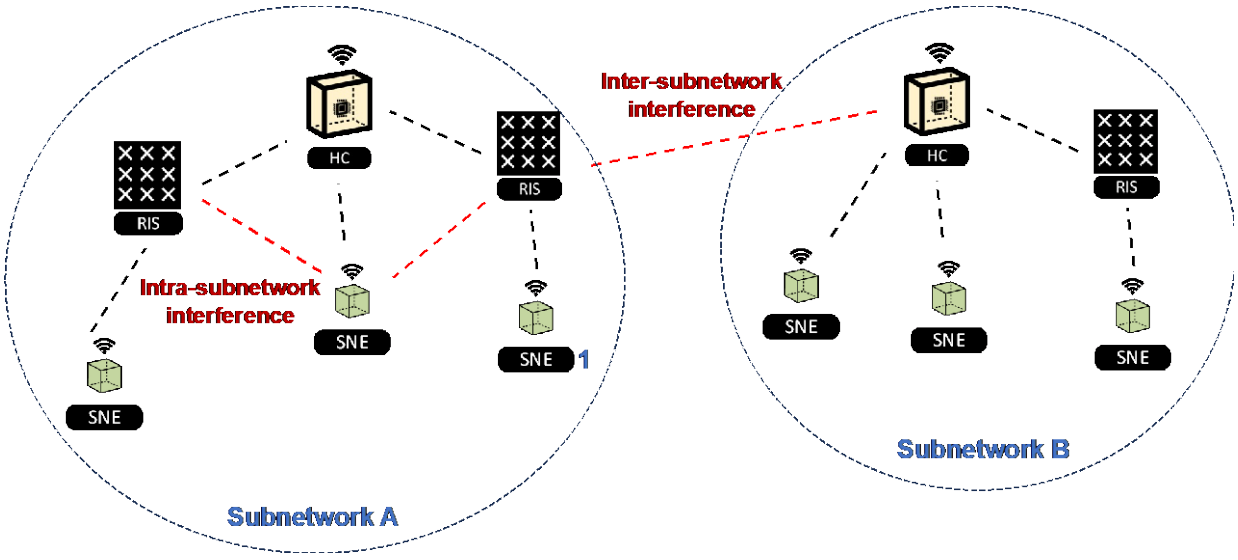

Figure 1. Intra- and inter-subnetwork interference caused by the presence of RISs.

Within this context, in 6G-SHINE the following two general situations, illustrated in Figure 1, typical of subnetworks have been addressed. The first situation refers to strategies conceived for improving intra-subnetwork communications aided by one or more RISs. In particular, the main purpose is to decrease the overall transmitted power while ensuring the desired transmission rate with as much as possible reduced overhead for channel state information (CSI) signalling and intra-subnetwork interference.
The second situation considers the presence of adjacent coordinated or uncoordinated subnetworks, each aided by RISs, in which the main purpose is to mitigate the interference caused by unwanted reflections from RISs. In

fact, while the RIS in subnetwork *A* is configured to serve subnetwork element (SNE) 1 through the reflection of the signal coming from the HC node, it might reflect unpredicted signals coming from the neighbour subnetwork B to unwanted directions this creating interference to other SNEs belonging to subnetwork A.

The previous situations have been addressed in 6G-SHINE through:

- The introduction of more advanced models for RIS based on multi-port theory that have been adopted in the subsequent analysis where an offline optimization method, relying solely on statistical knowledge of the channel, has been proposed to reduce the overhead associated with channel state information (CSI).
- The definition of macroscopic ray-based models for RIS that can be embedded into system simulation tools, and their validation through reference models such as physical optics and full-wave electromagnetic simulations.
- The design of novel structures for RIS, in particular, those referred to as non-diagonal RISs offering improved flexibility in mitigating unwanted interference, and the development of RISs capable of forming wide beams.
- The design and analysis of low-complexity optimization strategies for power minimization with rate constraints in the presence of multiple conventional RISs and multiple SNEs.
- The investigation of flexible packet coding strategies providing higher reliability benefits to communication links.
- The design and analysis of optimization strategies for inter-subnetwork interference reduction based on non-diagonal RISs or some level of coordination between subnetworks.

In addition, the activity carried out on RIS technologies and signal processing methodologies has spurred some by-products, initially not foreseen in the project proposal, which could have an impact especially in consumer applications. Specifically, double beamforming effect of RISs when used in conjunction with ultrawide bandwidth (UWB) signals has been discovered and turned from a potential issue into a benefit by properly engineering the RIS.

This document is structured as follows: In section 2, we summarize the main outcomes of the novel RIS structures, modelling approaches, optimization strategies, and RIS-enhanced communication schemes developed in the project whose details are reported in the subsequent sections.
Specifically, section 3 discusses the necessary control signalling for operating a RIS in subnetworks, according to a variety of operational modes, then it introduces a general macroscopic approach that allows the computation of the near-field and far-field reradiated by a RIS and is independent from the specific RIS technology as well as a multiport model suitable for low complexity optimization of RIS' parameters. Then a RIS model with non-diagonal transfer function based upon tunable permutations and studies of RISs capable of forming wide beams are introduced.
In section 4, scenarios involving one subnetwork with potential high number of nodes, and in the presence of RIS, are explored. The scenarios focus on the support that RIS can provide for the communication process in the subnetwork, both in terms of coverage extension by providing additional transmission links, and conversely, how the RIS can be used to serve multiple nodes at the same time.
The analysis involving more, possibly uncoordinated, subnetworks in the presence of one or more RISs is presented in Section 5, where the dual aspect of the benefits and impairments that the presence of RISs can bring to cooperative and non-cooperative subnetwork scenarios is addressed. Typical implementations of a RIS are narrowband and limited studies are available on wideband RISs. IN this direction, section 6 proposes some analyses of ultra-wideband RISs by showcasing the impact and potential in subnetwork applications. Finally, in Section 7 the conclusions are drawn.

2 MAIN OUTCOMES OF RIS-BASED SOLUTIONS FOR SUBNETWORKS

2.1 Introduction

The activity carried out in the project related to RISs has mainly addressed the Technology Component **TC7 *(RIS Enhancements)***" but also involved **TC13 (Distributed/hybrid radio resource management).**

Novel solutions for RIS technology and optimization schemes have been proposed to tackle the following KPIs and verified with reference to Objective 3 of the proposal "*Design new physical layer (PHY) enablers for scalable requirements in terms of latency, reliability or throughput, tailored to devices with constrained computational capabilities by leveraging the opportunities offered by short range subnetworks*":

- *Spectral efficiency* (Amount of transferred bits at given time and frequency resources): In the context of RISs, the focus was on increasing the coverage and data rate per node in the subnetwork without the deployment of additional HC nodes and latency thanks to the introduction of RISs.
- *Energy consumption* (Energy spent by the radio equipment - with particular focus on devices - in transmitting and receiving data, i.e., reduction of transmission power): The goal was to obtain a reduction of the transmitting power by several dBs to achieve the same target in terms of desired data rate per node in the subnetwork with respect to the state-of-the-art (SoA); this is particularly beneficial for reducing interference in adjacent subnetworks.
- *Computational Complexity* (Amount of compute and memory resources for completing a given task): The introduction of RISs instead of additional HC nodes intrinsically reduces hardware and computational complexity. Moreover, computational complexity was a specific target of the proposed solution for efficient prediction of the field reradiated by a RIS and RIS optimization: by adopting the approach of dividing the RIS into tiles and relying on a fully ray-based description, a reduction in complexity of at least one order of magnitude has been achieved compared to the SoA, depending on the size of the RIS.

The main outcomes of the project include technological and modelling aspects as well as novel RIS optimization strategies and RIS-enhanced communication schemes addressing the project KPIs and the use cases defined in Deliverable D2.2 [2]. Regarding the first aspect, the solutions proposed are presented in Section 3 and are application-agnostic. They concern:

- Advanced models for RISs, including macroscopic ray-based models and their validation in WP2 through measurement campaigns.
- Design of novel structures for RIS especially suited for their application to subnetworks, including wide beams and wideband RISs.

In the following, we summarize the main outcomes of the novel RIS optimization strategies and RIS-enhanced communication schemes developed in the project. Details are provided in Sections 4, 5, and 6. Even though many of the proposed solutions can be applied in principle to several use cases, in the following they have been validated in some relevant use cases and associated KPIs/KVIs as defined in Deliverable D2.2 [2].

RIS design for wide beams
Reference use case: Industrial use case 'Subnetwork Swarm: Coexistence in Factory Hall'.
Target KPIs: Computational complexity • Up to a maximum of 20 nodes to be controlled; • Minimum data rate of 10 Mbps per node;
Main results: In this use case, many devices should be connected at a rather low data rate, but with high requirements on latency and reliability. In view of a RIS, the tough requirements on latency and reliability in conjunction with the moderate requirement on data rate imply that (i) the beamforming gain may be lower compared with other use

cases, and (ii) the beam management process must be both fast and reliable. A solution addressing both these points is to let the RIS have a single static configuration that covers the entire subnetwork (or at least a considerable part of it). For example, dead spots may be covered by the RIS. This implies that the reflection pattern of the RIS should be wide, i.e., covering a large span of angles. Furthermore, the computational complexity of the beam management process is null. The design of such a wide RIS beam is by no means trivial. In this context, a key result is the wide beam generation of a RIS. For, e.g., broadcasted signals that are reflected by a RIS, **a wide beam is essential for reaching a goal of 20 nodes**. This is so since a single RIS configuration covers a multitude of nodes. Meanwhile, the array gain of such wide beam is moderate, but as the data rate constraint is moderate, it suffices.

Low-CSI overhead RIS design using a multiport network model

Reference use case: Industrial subnetwork use case 'Subnetworks Swarms: Subnetwork Co-existence in Factory Hall'.

Target KPIs:

- Reduction factor of *N*, equivalent to the number of RIS elements, in the required signalling overhead compared to perfect CSI acquisition;
- Interference reduction through specular reflection reduction;

Main results: A critical challenge in Reconfigurable Intelligent Surface (RIS) technology is the need for Channel State Information (CSI) to optimize RIS configurations. CSI estimation introduces significant signalling overhead and latency. To address this, the proposed approach aims to optimize RIS performance *without* relying on perfect, instantaneous CSI. Instead, the RIS is optimized based on *statistical* CSI, which operates on a longer time scale, thereby reducing CSI overhead. This eliminates the need for frequent RIS reconfigurations based on predetermined patterns. The scenario considered is a sub-network (SN) where multiple sub-network entities (SNEs) communicate with a high-capability (HC) controller, supported by a RIS. The RIS is modelled using a physically consistent multi-port (MP) network model that accounts for mutual coupling between scattering elements and structural scattering, factors often overlooked by traditional RIS models. The scenario dimensions are on the order of several meters, resulting in near-field/far-field boundary propagation conditions, typical of consumer or industrial sub-networks (e.g., indoor gaming, robot control). The specific problem addressed is optimizing the RIS to maximize the average bit rate for a communicating node in the presence of interference from other nodes, using only statistical knowledge of the node positions, rather than instantaneous channel information.

Simulation results (Figs. 4-6) for two users (Nu=2) show the average rate with the intended user and the interfering user at 15 different angular positions at the same distance (10m). The figures compare performance for element spacing $\lambda/2$ and $\lambda/4$ and position uncertainty σ = 0.1, 0.5, 1 m. The proposed scheme OPT-NoCSI (statistical CSI only) approaches the ideal OPT-CSI (exact CSI) performance, especially at lower position uncertainties, and outperforms the OPT-CT scheme (ideal RIS model), particularly when the specular reflection creates strong interference. The OPT-NoCSI shows the great advantage because of the significant reduction in RIS configuration overhead.

RIS-aware flexible packet coding (FPC) strategies

Reference use case: Industrial subnetwork use case 'Visual inspection unit'

Target KPIs:

- x10 improvement in spectral efficiency with respect to a RIS-absent scenario

Main Results

The contribution exploits the main benefit of the RIS, the coverage extension aspects. The RIS introduces a cascaded channel that can be considered both within a subnetwork, between subnetworks, or between a subnetwork and the parent 6G network. The nature of the cascaded channel introduces radio measurements challenges, as the radio measurements of both parts of the link can be measured at different rates, and the measurements of the entire cascaded link are not available to the transmitter. Therefore, in case interference is present, there is a delay when it comes to adapting transmitter decisions in terms of which path to choose in multi-path scenarios. Particularly in time-division duplexing (TDD) systems, synchronization of this information plays a key role.

The FPC strategies introduced help solving this problem as they introduce additional error detection and correction mechanisms, in part by evaluating which of the links contributes more to re-transmission of the scheduled packets.

The reference use case is visual inspection unit. In this use case, transmitted data can originate from RF sensors in the factory, and cameras. Packet sizes are small compared to other use cases, and reliability is a fundamental KPI, as well as low latency for transmissions, and requirements for low buffer. This type of traffic is characterized by constant high volume, requiring also constant high modulation and coding scheme (MCS) allocation. FPC goes beyond the state of the art by increasing reliability and reducing latency, taking advantages of the multi-link subnetwork scenarios, resorting to packet duplication. The use of high MCS values is typically permeable to perturbances in the radio link and increase error rates. IDE simulation results comparing state of the art LDPC with FPC, show BLER values of 10^{-2} and 10^{-3}, respectively, for a fixed value of 19dB for SNR. This represents an approximately x10 improvement in spectral efficiency with respect to not using a RIS.

Power Minimization with Rate Constraints for Multiple RISs with Multiple Nodes in Industrial Environment

Reference use case: Industrial subnetwork use case 'Subnetworks Swarms: Subnetwork Co-existence in Factory Hall'.

Target KPIs:

- Up to a maximum of 20 nodes to be controlled;
- Minimum data rate of 10 Mbps per node;
- Maximum transmitting power 20 dBm

Main results:

The use case considers the connection of many robot nodes with a control entity deployed within the confines of an edge infrastructure. The edge controller point performs advanced management strategies possibly aided by a multiple-input multiple-output (MIMO) transmission system to serve all nodes simultaneously while minimizing latency and interference. Considering the critical role played by the controller, it might be worthwhile to have a backup or redundancy mechanism for providing the required performance. This case requires connecting to 20 robot nodes with a control entity deployed within edge infrastructure confines.

Within this context, we aimed to provide a solution for the optimization of multiple RISs to minimize power consumption while ensuring a minimum transmission rate for each node. The analysis focused on the connection between the HC controller and the SNEs to dispatch control information, utilizing a MIMO transmission system to serve all nodes simultaneously while minimizing latency and interference. Given that the subnetwork must interoperate with other similar subnetworks, minimizing power is a critical target. Therefore, we considered deploying multiple appropriately optimized RIS positioned above all nodes and obstacles, facilitating a strong Line-of-Sight (LOS) propagation condition between the HC and SNEs and the RISs. This is the typical situation in which RISs are beneficial for meeting the required KPIs. This approach effectively addresses the target KPIs, demonstrating the benefits of RIS technology in achieving the desired communication performance in the specified scenario.

The main results are summarized in Figure 24 of Section 4.2. It is demonstrated that the use of RIS, when properly optimized, allows for the achievement of the KPIs **(20 users with 10 Mbps each) while saving from 5 dB up to 60 dB (when the direct path is highly attenuated) of power compared to the scenario where RIS are not present**. This is illustrated by considering different propagation scenarios discussed in Deliverable D2.3 [3]. In some cases, it is also shown that the use of RISs is essential to achieve the target KPIs.

Interference mitigation through non-diagonal RISs
Reference use case: Consumer use case 'Indoor interactive gaming'
Target KPIs: Spectral efficiency • Up to a maximum of 10 nodes to be controlled; • Data rates in the range 100 Mbps - 1Gbps per node;
Main results: As already commented, typical use cases for RISs are to place them sufficiently elevated so that that strong LOS conditions are ensured to/from all nodes. This, however, also makes the RISs vulnerable for impinging interference from transmitters in other cells. This interference will, unless countermeasures are taken, potentially degrade the performance of the subnetwork. It is therefore of interest for said use cases to research ways of RIS implementations so that said interference can be eliminated. Within the project, non-diagonal RISs for interference mitigation of undesired reflections from the RIS have been designed. These are signals not being transmitted by the sub-network but nonetheless are reflected by the RIS and interferers with the subnetwork. In particular, non-diagonal RISs are obtained by tunable permutations. A key result is summarized in Figure 28 of section 5.1, where we report **20-30 dB reduction of interference levels for RIS assisted subnetworks**. This may transition the system from an interference limited regime into noise limited territory, which brings about drastic gains in spectral efficiency/throughput. These impressive gains are obtained by a re-design of the RIS architecture so that it is spatially selective, i.e., it only reflects signals from a given impinging angle. For gaming use cases the requirement on bitrate is extreme, wherefore interference must be kept at a minuscule level. We have reported substantial interference reductions based on our proposed technology. Thus, our RIS design assists in meeting the **KPI of 100Mbps per node**.

RIS design for wide bandwidth signals
Reference use case: Consumer use case 'Indoor interactive gaming'
Target KPIs: Spectral efficiency • Up to a maximum of 10 nodes to be controlled; • Data rates in the range 100 Mbps - 1Gbps per node;
Main results: For extreme data rates, low latency, and extreme positioning precision - features that are all commonplace in indoor interactive gaming use cases - sub-THz, UWB, or wideband operation may be envisioned. In these cases, standard RIS technology breaks down as the differences in propagation delays across a RIS are not negligible compared to the reciprocal of the bandwidth. Hence, we considered ways of operating RISs for these scenarios. Therefore, another key result of the project is that we have extended the RIS technology into wide bandwidth signals, such as will be encountered in sub-THz and/or UWB. For wide bandwidth signals, traditional RIS designs are much less efficient due to propagation delay differences across the RIS. However, in the project we have proposed a method that not only overcomes this problem, but, in fact, turns it into an advantage: The RIS has the potential to perform even better at wide bandwidth compared with normal bandwidth despite the aforementioned problem. **With the proposed method, a RIS can support around 5 times the bandwidth compared with normal RIS**s. Thus, allowing for a rate gain of 5 times, which assists in meeting the data rate KPI.

3 ENHANCED MODELS FOR RIS

The project has advanced the state-of-the-RIS-art in several different directions, all of which are important for subnetworks. Specific contributions are:

- In subsection 3.1, a brief overview of necessary control signalling for operating a RIS, according to a variety of operational modes, for subnetworks is provided.
- Subsection 3.2, treats development of a general macroscopic approach that allows the computation of the near-field and far-field reradiated by a RIS and is independent from the RIS technology as it relies on effective parameters that describe the phase and amplitude modulation on the RIS surface. The model is suitable to be embedded into deterministic ray-based field prediction tools (ray tracing), which are essential for the planning of RIS-aided subnetworks.
- Moreover, subsection 3.2 provides a derivation of reflection/transmission/diffraction coefficients to be used in the macroscopic ray model, from an asymptotic approximation of the Physical Optics (PO) integral: these coefficients can be applied to reflective and transmissive RISs, and to RISs having multiple reradiation modes. Preliminary validation tests suggest that the proposed model is as accurate as the well-established PO method, but faster by about an order of magnitude.
- Subsection 3.3 develops a RIS model with non-diagonal transfer function based upon tunable permutations. This is a continuation of the presented material in Deliverable D3.2 [1]. The ensuing benefits of the RIS modelled developed herein are investigated, within a subnetwork context, in Section 4.
- Subsection 3.4 studies RISs capable of forming wide beams. In a nutshell, this work is based upon previously published methods for array antennas but adapts it to a RIS context. A RIS with wide reflection patterns is important in static deployments in which the RIS should cover the entire subnetwork.
- Finally, Subsection 3.5 presents both a model (the multi-port network model) and a method for the optimization of RIS based on such model with statistical channel knowledge.

3.1 RIS operational modes extension

In Deliverable D3.2 [1], a RIS classification was introduced covering features such as reconfigurability, boundary conditions, power, selectivity, data bearing, operation mode (transmitting or reflecting RIS), and implementation technology. In this section, those definitions are extended to account for new scenarios where RIS applicability is envisioned [4], and with special consideration in the context of subnetworks. This extension covers both operation modes, and control information for the RIS.

The operational modes extended in this document include absorption, backscattering, enhanced transmitting, and receiving modes. A brief characterization of these modes is given below:

- **Absorption mode -** Under the absorption mode, the impinging radio wave of a certain centre frequency and a certain bandwidth can, ideally, be totally absorbed and no reflection wave can be observed. This is typically done by switching each RIS element on a matched load so that all the power captured by the RIS is dissipated. However, a residual “structural scattering” component generated by the structure of the RIS panel is always present in real situations.
- **Backscattering mode -** For a RIS in backscattering mode, the reflected wave is to cover a large area instead of an exact location. Therefore, the balance between gain and effective area is necessary for realizing wide-angle blind spot coverage. Backscattering mode can be used for passive RIS, which are manufactured to reflect an impinging EM signal into a certain direction.
- **Enhanced Transmitting mode -** A RIS in transmitting mode is incorporated in a radio transmitter with the RIS assisting in shaping the transmitted radio wave. As an example, Dynamic Meta surface Antennas (DMAs) have been recently proposed as an efficient realization of extreme massive antenna arrays.

- **Receiving mode -** A RIS in receiving mode is capable of receiving and processing radio signals. This can be accomplished by embedding waveguides at each RIS element, or group of elements, to direct the impinging radio signals to reception hardware. This hardware may include, for example, a low noise amplifier, a mixer down converting the signal from RF to baseband, and an analog-to-digital converter.

These modes represent important considerations for when the RIS is available within, or outside a subnetwork, as their functioning is tailored for particular use cases and topologies. For example, absorption mode can represent the absence of the RIS, which could be very useful for interference management, as it would prevent reflections. Backscattering mode can cover wider subnetwork areas but at the cost of the signal gain. This can have implications on the target requirements for the subnetwork and careful analysis of this trade-off is required. Enhanced transmission mode can be seen as an opposite of the backscattering mode, where highly localized, high gain transmission can be achieved, at the cost of the covered area. The receiving mode can be used in cases where processing of the radio signals is useful to be executed by the RIS.

In this document, it is considered that the RIS can be operating in any of these modes, and the mode selection can be done at the convenience of the use case, its requirements, deployment scenario and other use case considerations, like mobility, interference levels, etc.

3.1.1 Control information for RIS operation

The RIS operating mode can be activated by other control nodes. This can be the responsibility of the parent 6G-network, or any other node that can communicate with it, e.g., an HC. Along with the operational mode, there could be other useful characteristics to control in any RIS. Below is a list of potential characteristics, as well as some details on them:

- **Controlling mode indication**: this would be related to configuring the RIS with the controlling modes, with details both in Deliverable D3.2 [1], and above;
- **Operating mode indication**: this would relate to the indications for switching between the different supported RIS modes, that can be sent to the RIS by any node in the topology;
- **Timing information**: this would be related to the duration of applicability for a given RIS configuration. In the case of the operational mode, this can indicate to the RIS information on how long to operate in different modes;
- **Feedback information**: this would relate to capability information exchanges, activation of ACK/NACK messages of receiving any of the control information, enabling CSI report, if the RIS supports that, etc.
- **Spatial information**: this would relate to explicit or implicit indication related to phase/amplitude, directivity, beamforming information, etc.
- **UL/DL TDD configuration information**: this would relate to resource utilization and interference management, where synchronization plays a key role.

The considered indications and information exchanges can be executed at any point in time, providing additional flexibility and opening the door for further exploitation of RIS components as participating nodes in subnetwork topologies.

3.2 Macroscopic ray-based models for RIS and their validation

3.2.1 Introduction

Reconfigurable Intelligent Surfaces (RIS) have emerged as a transformative technology for enhancing wireless communication by dynamically shaping electromagnetic wave propagation. Two primary approaches to modelling RIS behaviour are microwave network modelling, adopted in the foregoing studies, and ray-based macroscopic modelling addressed in the present section. Each offers unique insights into RIS performance and applicability.

Microwave network modelling provides a circuit-based perspective, representing RIS elements as interconnected microwave components. This approach treats each RIS unit cell as a tunable scatterer within a multi-port network framework, which can offer accurate characterization, allowing for optimization of unit-cell and network parameters, and integration with other RF components. However, it is not suitable for metasurface realizations, i.e. for RISs with electrically-small unit cells [5], nor can it be easily embedded in ray tracing propagation models to achieve efficient system-level simulation of RIS-aided communication systems.

In contrast, ray-based macroscopic modelling of scattering from RIS focuses on large-scale effects of wave interactions with the surface employing an efficient physics-based formulation. This approach considers the RIS as a continuous scatterer described by a few parameters and a *spatial modulation coefficient*, that accounts for the desired phase, amplitude, and polarization modulation of impinging waves disregarding the underlying network technique or microscopic phenomena that generate such a modulation. Microwave network methods, electromagnetic models or measurements are of course necessary to derive the macroscopic parameters used in this approach. Macroscopic models are useful for understanding RIS influence on system-level parameters such as path loss, angular spread, and channel capacity. They are particularly advantageous for efficient, large-scale simulation and network planning, where detailed electromagnetic analysis may be computationally prohibitive.

The following subsections provide a concise description of the ray-based RIS model developed within 6G-SHINE, including its validation and further development.

3.2.2 Fully ray-based macroscopic modelling

The fully ray-based approach offers a Geometrical Optics (GO)-inspired technique for efficient and yet electromagnetically-consistent RIS scattering simulation.

As a first step, multiple *reradiation modes,* including both the desired and the parasitic reradiated waves, must be identified using Floquet's theory under the assumption of *locally periodic* RIS configuration. Each mode is associated to an amplitude coefficient and a Spatial Modulation Dyadic (SMD) $\underline{\mathbf{\Gamma}}$ that determines the phase and amplitude modulation at the RIS surface as described in WP2's Deliverable D2.3 [3]. An overall power-balance must be enforced to make sure that the amplitudes of the incident wave and of all the reradiated waves are compatible with power conservation over the RIS slab. Then for each mode, the procedure described below is followed to achieve a ray-based description of its reradiated field.

Unlike wave-based models, this method discretizes the RIS surface into small *elements* or *tiles*, treating each as a local plane wave interaction point. Using this discretization, the method computes the anomalously reflected rays at each tile while considering the curvature of both the incident and reradiated wavefronts. The key steps involved in this approach include:

1. **Computation of the Anomalous Ray Direction**: determining the reflected ray trajectory based on the surface phase and amplitude (impedance) modulation.
2. **Computation of the Reradiated Field**: evaluating the field reradiated by each tile of the RIS.
3. **Computation of the reradiated wave Spreading Factor**: Calculating wave attenuation as it propagates.

The whole procedure is based on the cited SMD $\underline{\mathbf{\Gamma}}$ that can be expressed as:

$$\underline{\mathbf{\Gamma}}\left(\mathbf{r}'\right) = \underline{\mathbf{\Gamma}}_0\left(\mathbf{r}'\right)\mathrm{e}^{\mathrm{j}\chi^{\mathrm{m}}(\mathbf{r}')} = \mathrm{A}^{\mathrm{m}}\left(\mathbf{r}'\right)\mathrm{e}^{\mathrm{j}\chi^{\mathrm{m}}(\mathbf{r}')}\cdot\underline{\mathbf{R}}^{\mathrm{m}} \tag{1}$$

where $\mathbf{r}'$ is the generic position on the surface, $K^m(\mathbf{r}')$ and $\chi^m(\mathbf{r}')$ are the *amplitude and phase* modulation profiles that the RIS imposes on the reradiated field whereas matrix $\underline{\mathbf{R}}^m$ applies the polarization transformation.

In step 1, the reradiated ray direction is computed on the base of the incident ray field direction and of the phase profile gradient $\nabla\chi^m$. In steps 2 and 3 the reradiated field is computed according to the Geometrical Optics (GO) theory using (1) and the incident field $\boldsymbol{E^i}(\boldsymbol{r}')$ as:

$$\boldsymbol{E}^r(\boldsymbol{r}) = \underline{\boldsymbol{\Gamma}}(\boldsymbol{r}')\boldsymbol{E^i}(\boldsymbol{r}')A^r(s)e^{-jk|\boldsymbol{r}-\boldsymbol{r}'|} = \underline{\boldsymbol{\Gamma}}(\boldsymbol{r}')\boldsymbol{E^i}(\boldsymbol{r}')\sqrt{\frac{\rho_1^r\rho_2^r}{(\rho_1^r+s)(\rho_2^r+s)}}e^{-jks} \tag{2}$$

being **r** the position vector of the observation point P, $s = |\boldsymbol{r}-\boldsymbol{r}'|$ the local coordinate along the reflected ray, *k* the free-space wave number, and ρ_1^r, ρ_2^r the curvature radii of the reradiated wave, assumed a generic astigmatic wave. A more complete formulation can be found in [5].

A similar procedure can be applied to the computation of the diffracted rays on the edge of a finite-size RIS using an adaptation of the Uniform Geometrical Theory of Diffraction (UTD), as shown in Deliverable D2.3 [3] and in [5]. The procedure has been recently generalized to transmit rays for a transmissive RIS, - i.e. a transparent RIS that can apply wave transformation to transmitted waves - and to the rays diffracted by the RIS' vertices as shortly explained below.

3.2.3 Model validation and its extensions

Following the same approach as in [5] we extend the macroscopic ray model to the case of transmissive-RIS (transmissive metasurfaces and transmitarrays), or more in general, to a RIS that is able to reradiate both in the reflection and in the forward (transmission) half-space. The aim is to derive asymptotic expressions for the re-radiated field that can be cast in a GO/UTD format, by extending the method initially proposed in [6] for a "regular" curved surface to the case of a bidirectional RIS [7]. In order to do that, we model the RIS as an impedance sheet with different characteristics at the 2 sides: in particular, the RIS has different phase profiles c+ and c- on the sides $\hat{\mathbf{n}}$ and $-\hat{\mathbf{n}}$, respectively, where the normal $\hat{\mathbf{n}}$ to the surface is oriented toward the backward (reflection) half-space. Moreover, we can take into account large scale variations (e.g. non-local effects) and polarization transformations through dyadic amplitude modulation coefficients $\mathbf{G}_0$ and $\mathbf{T}_0$.

Overall, these effects are considered through the following "spatial modulation" coefficients **G** and **T**, that accounts for reradiation in the backward and forward half-space, respectively:

$$\begin{cases} \underline{\boldsymbol{\Gamma}}(\mathbf{r}') = \underline{\boldsymbol{\Gamma}}_0(\mathbf{r}')e^{j\chi^+(\mathbf{r}')} & \mathbf{r}\cdot\hat{\mathbf{n}} > 0 \\ \underline{\mathbf{T}}(\mathbf{r}') = \underline{\mathbf{T}}_0(\mathbf{r}')e^{j\chi^-(\mathbf{r}')} & \mathbf{r}\cdot\hat{\mathbf{n}} < 0 \end{cases} \tag{3}$$

where $\mathbf{r}'$ is the position vector of the generic "tile" of the RIS surface, while $\mathbf{r}$ is the position vector of the generic observation point P.

The overall reradiated field by a finite-size RIS, according to the Physical Optics (PO) approach, can be expressed by means of the following radiation integral [6]

$$\mathbf{E}^s(\mathbf{r}) = \frac{jk}{4\pi}\iint_S \hat{\mathbf{R}}\times\left[\mathbf{M}(\mathbf{r}') + \hat{\mathbf{R}}\times\eta\mathbf{J}(\mathbf{r}')\right]\frac{e^{-jkR}}{R}dS \quad \text{with } \mathbf{R} = R\hat{\mathbf{R}} = \mathbf{r}-\mathbf{r}' \tag{4}$$

with **J** and **M** electric and magnetic currents, respectively, that are computed according to the equivalence theorem:

$$\begin{aligned} \mathbf{M}(\mathbf{r}) &= \left[\mathbf{E}_0^i e^{-jk\hat{\mathbf{s}}^i\cdot\mathbf{r}} + \underline{\boldsymbol{\Gamma}}\cdot\mathbf{E}_0^i e^{-jk\hat{\mathbf{s}}^i\cdot\mathbf{r}} - \underline{\mathbf{T}}\cdot\mathbf{E}_0^i e^{-jk\hat{\mathbf{s}}^i\cdot\mathbf{r}}\right]\times\hat{\mathbf{n}} \\ \mathbf{J}(\mathbf{r}) &= \frac{\hat{\mathbf{n}}}{\eta}\times\left[\hat{\mathbf{s}}^i\times\mathbf{E}_0^i e^{-jk\hat{\mathbf{s}}^i\cdot\mathbf{r}} + \hat{\mathbf{s}}^r\times\underline{\boldsymbol{\Gamma}}\cdot\mathbf{E}_0^i e^{-jk\hat{\mathbf{s}}^i\cdot\mathbf{r}} - \hat{\mathbf{s}}^t\times\underline{\mathbf{T}}\cdot\mathbf{E}_0^i e^{-jk\hat{\mathbf{s}}^i\cdot\mathbf{r}}\right] \end{aligned} \tag{5}$$

where $\hat{\mathbf{s}}^i$ is the direction of incidence, and $\hat{\mathbf{s}}^r, \hat{\mathbf{s}}^t$ are the directions of anomalous reflection and anomalous transmission, respectively, that can be expressed as [7]

$$\begin{cases} \hat{\mathbf{s}}^r = \left(\underline{\mathbf{1}} - \hat{\mathbf{n}}\hat{\mathbf{n}}\right)\cdot\hat{\mathbf{s}}^i - \dfrac{1}{k}\nabla\chi^+ + \sqrt{1 - \left|\left(\underline{\mathbf{1}} - \hat{\mathbf{n}}\hat{\mathbf{n}}\right)\cdot\hat{\mathbf{s}}^i - \dfrac{1}{k}\nabla\chi^+\right|^2}\ \hat{\mathbf{n}} \\ \hat{\mathbf{s}}^t = \left(\underline{\mathbf{1}} - \hat{\mathbf{n}}\hat{\mathbf{n}}\right)\cdot\hat{\mathbf{s}}^i - \dfrac{1}{k}\nabla\chi^- - \sqrt{1 - \left|\left(\underline{\mathbf{1}} - \hat{\mathbf{n}}\hat{\mathbf{n}}\right)\cdot\hat{\mathbf{s}}^i - \dfrac{1}{k}\nabla\chi^-\right|^2}\ \hat{\mathbf{n}} \end{cases} \tag{6}$$

By substituting (3) in (4) and (5), the radiation integral can then be reduced to the following canonical form [7]:

$$\boldsymbol{E}^s(\boldsymbol{r}) = \frac{jk}{4\pi}\left\{\underbrace{\iint_S \underline{\boldsymbol{G}}^i \cdot \boldsymbol{E}_0^i \frac{e^{-jk(\hat{\mathbf{s}}^i\cdot\mathbf{r}'+R)}}{R}dS}_{\boldsymbol{A}} + \underbrace{\iint_S \underline{\boldsymbol{G}}^r \cdot \underline{\boldsymbol{\Gamma}}_0 \cdot \boldsymbol{E}_0^i \frac{e^{j[\chi^+ - k(\hat{\mathbf{s}}^i\cdot\mathbf{r}'+R)]}}{R}dS}_{\boldsymbol{B}} + \underbrace{\left(-\iint_S \underline{\boldsymbol{G}}^t \cdot \underline{\boldsymbol{T}}_0 \cdot \boldsymbol{E}_0^i \frac{e^{j[\chi^- - k(\hat{\mathbf{s}}^i\cdot\mathbf{r}'+R)]}}{R}dS\right)}_{\boldsymbol{C}}\right\} \tag{7}$$

while the dyadic coefficients $\underline{\mathbf{G}}^i$, $\underline{\mathbf{G}}^r$, $\underline{\mathbf{G}}^t$ are computed as [6]:

$$\underline{\mathbf{G}}^a = \left(\hat{\mathbf{R}}\cdot\hat{\mathbf{n}}\right)\underline{\mathbf{1}} - \hat{\mathbf{n}}\hat{\mathbf{R}} + \left(\underline{\mathbf{1}} - \hat{\mathbf{R}}\hat{\mathbf{R}}\right)\cdot\left[\left(\hat{\mathbf{s}}^a\cdot\hat{\mathbf{n}}\right)\underline{\mathbf{1}} - \hat{\mathbf{s}}^a\hat{\mathbf{n}}\right] \qquad a = i, r, t \tag{8}$$

It is worth noting that, differently from the expression of the scattered field reported in [6] for a "standard" surface, the radiation integral (7) is split into 3 parts (**A**, **B**, **C**), as incident, reflected and transmitted fields have different phases on the RIS surface, due to the phase profiles c+ and c- that modulate the locally reflected and transmitted fields.

This finding justifies the assumption made in [5], where is it explained through heuristic considerations that diffracted rays that compensate for discontinuity of anomalous reflection in the shadow region belong to an "anomalous Keller's cone", that is different from the "ordinary Keller's cone", made of rays that compensate for discontinuity of the incident field. Therefore, the Incidence Shadow Boundary (ISB) and the "Anomalous" Reflection Shadow Boundary (ARSB) belong to different Keller's cones. For the same reason, in the case of transmissive RIS, the presence of the anomalous transmission gives rise to the presence of a further anomalous Keller cone, and of an Anomalous Transmission Shadow Boundary (ATSB), as depicted in Figure 2.

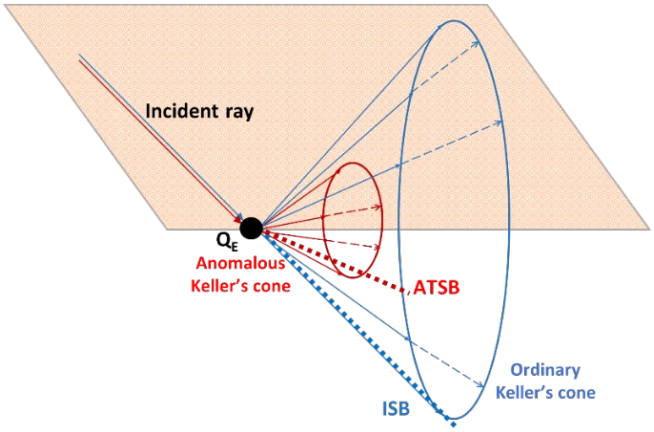

Figure 2. Ordinary Keller's cone and Incidence Shadow Boundary, and corresponding anomalous Keller's cone in the forward half space and Transmission Shadow Boundary.

In fact, following the same approach as in [6], the terms **A**, **B**, **C** in (7) can be asymptotically approximated as:

$$\frac{jk}{4\pi}\boldsymbol{A} \simeq -\boldsymbol{E}^i(P)U^{f,o} + \sum \boldsymbol{E}^{d,o}(P)U^{e,o} + \sum \boldsymbol{E}^{v,o}(P)$$

$$\frac{jk}{4\pi}\boldsymbol{B} \simeq \boldsymbol{E}^{r}(P)U^{r,a} + \sum \boldsymbol{E}^{d,ar}(P)U^{e,ar} + \sum \boldsymbol{E}^{v,ar}(P) \tag{9}$$
$$\frac{jk}{4\pi}\boldsymbol{C} \simeq \boldsymbol{E}^{t}(P)U^{f,at} + \sum \boldsymbol{E}^{d,at}(P)U^{e,at} + \sum \boldsymbol{E}^{v,at}(P)$$

In (9) it is evident the presence of separated diffraction contributions that compensate for abrupt transition of the incident, reflected and transmitted field, respectively.

The function *U* used in (9) is a "step function" which vanishes within the respective ray shadow region, thus bounding the various rays inside their domains of existence. The superscripts *o, ar, at*, refer to "ordinary", "anomalous reflection" and "anomalous transmission", respectively.

The reflected field $\mathbf{E}^r$ and the transmitted field $\mathbf{E}^t$ in (9) are expressed in the following form, according to the GO theory:

$$\begin{cases} \mathbf{E}^{r}\left(\mathbf{r}\right) = \underline{\mathbf{\Gamma}}\left(\mathbf{r}'\right)\mathbf{E}^{i}\left(\mathbf{r}'\right)\sqrt{\dfrac{\rho_1^r\rho_2^r}{(\rho_1^r+s)(\rho_2^r+s)}}\,e^{-jk\cdot s} \\ \mathbf{E}^{t}\left(\mathbf{r}\right) = \underline{\mathbf{T}}\left(\mathbf{r}'\right)\mathbf{E}^{i}\left(\mathbf{r}'\right)\sqrt{\dfrac{\rho_1^t\rho_2^t}{(\rho_1^t+s)(\rho_2^t+s)}}\,e^{-jk\cdot s} \end{cases} \tag{10}$$

where s is the local coordinate along the reflected/transmitted ray, $\rho_1^{r,t}$, $\rho_2^{r,t}$ are the principal curvature radii of the reflected/transmitted wave, which is generally astigmatic, as the phase modulation of the RIS modifies the curvature of the incident wave, as explained in detail in [5]. Here we extend the same approach also to the case of a transmissive RIS. Therefore, the curvature radii of the reflected/transmitted waves are computed as the 2 non-zero eigenvalues of the respective "curvature matrix", in the following way [5],[7]:

$$\underline{\mathbf{Q}}^{r,t} = \left(\underline{\mathbf{1}} - \frac{\hat{\mathbf{n}}\hat{\mathbf{s}}^{r,t}}{\hat{\mathbf{s}}^{r,t}\cdot\hat{\mathbf{n}}}\right)\left[\underline{\mathbf{Q}}^{i} - \frac{1}{k_0}\nabla\nabla\chi^{+,-}\right]\left(\underline{\mathbf{1}} - \frac{\hat{\mathbf{s}}^{r,t}\hat{\mathbf{n}}}{\hat{\mathbf{s}}^{r,t}\cdot\hat{\mathbf{n}}}\right) \tag{11}$$

where $\underline{\mathbf{Q}}^{r}, \underline{\mathbf{Q}}^{t}$ are the curvature matrices of the reflected and transmitted wave, respectively, while $\hat{\mathbf{s}}^{r}, \hat{\mathbf{s}}^{t}$ are the directions the reflected and transmitted ray, respectively, computed through (6). Moreover, from the asymptotic approximation in (9), PO diffraction coefficients can be derived in a straightforward way for both edge and vertex diffraction, following the same procedure as in [6]. The fields diffracted by RIS edges and vertices, respectively, that compensate for the transition of anomalous reflection, are expressed in the following form:

$$\begin{cases} \mathbf{E}^{d,ar}\left(s\right) = \underline{\mathbf{D}}^{ar}\cdot\mathbf{E}^{i}\left(Q_E\right)\sqrt{\dfrac{\rho^{d,r}}{s\left(\rho^{d.r}+s\right)}}\,e^{-jk\cdot s} \\ \mathbf{E}^{v,ar}\left(s\right) = \underline{\mathbf{D}}^{v,ar}\cdot\mathbf{E}^{i}\left(Q_V\right)\dfrac{e^{-jk\cdot s}}{s} \end{cases} \tag{12}$$

And the respective diffraction coefficients are [7]:

$$\underline{\mathbf{D}}^{ar} = -\frac{\left[\mathbf{G}^{r}\cdot\mathbf{\Gamma}_0\right]_{Q=Q_E}\cdot e^{-j\frac{\pi}{4}}}{2\sqrt{2\pi k}\,\sin\beta^{d,ar}\left[\left(\hat{\mathbf{s}}^{i}-\hat{\mathbf{s}}^{d,ar}\right)\cdot\hat{\mathbf{t}} - \dfrac{1}{k}\dfrac{\partial\chi^{+}}{\partial t}\right]}\mathcal{F}\left\{X^{E}\right\} \tag{13}$$

$$\underline{\mathbf{D}}^{v,ar} = \frac{\left|\hat{\mathbf{e}}_1\times\hat{\mathbf{e}}_2\right|\mathbf{G}^{r}\cdot\mathbf{\Gamma}_0\left(Q_V\right)}{4j\pi k\left[\left(\hat{\mathbf{s}}^{i}-\hat{\mathbf{s}}^{v}\right)\cdot\hat{\mathbf{e}}_1 - \dfrac{1}{k}\dfrac{\partial\chi^{+}}{\partial e_1}\right]\left[\left(\hat{\mathbf{s}}^{i}-\hat{\mathbf{s}}^{v}\right)\cdot\hat{\mathbf{e}}_2 - \dfrac{1}{k}\dfrac{\partial\chi^{+}}{\partial e_2}\right]}T\left\{x_1,x_2,w\right\} \tag{14}$$

In (13), $\beta^{d,ar}$ is the aperture of the anomalous Keller's cone for reflection, $\hat{\mathbf{s}}^{d,ar}$ is the direction of the diffracted ray that belongs to that cone, and $\hat{\mathbf{t}}$ is a unit vector tangent to the surface, so that $\hat{\mathbf{t}}\times\hat{\mathbf{n}} = \hat{\mathbf{e}}$ with $\hat{\mathbf{e}}$ unit vector

along the edge. $\hat{\mathbf{s}}^v$ in (14) is the direction of the ray diffracted by the vertex toward the observation point, while $\hat{\mathbf{e}}_1, \hat{\mathbf{e}}_2$ are the unit vectors tangent to the 2 adjacent edges forming the vertex. Finally, the functions *F* and *T* in (13) and (14) are the Fresnel transition functions for edge and vertex diffraction, respectively, and their arguments X^E, x_1, x_1, w have the same definition given in [6]. The curvature radius $\rho^{d,r}$ of the diffracted astigmatic wave is computed with the same procedure explained in [5].

With a similar procedure, the fields diffracted by the RIS edges and vertices, that compensate for discontinuity in anomalous transmission, are expressed as

$$\begin{cases} \mathbf{E}^{d,at}(s) = \underline{\mathbf{D}}^{at} \cdot \mathbf{E}^i(Q_E) \sqrt{\dfrac{\rho^{d,t}}{s\left(\rho^{d,t}+s\right)}}\, e^{-jk\cdot s} \\ \mathbf{E}^{v,at}(s) = \underline{\mathbf{D}}^{v,at} \cdot \mathbf{E}^i(Q_V) \dfrac{e^{-jk\cdot s}}{s} \end{cases} \tag{15}$$

and the respective diffraction coefficients are [7]:

$$\underline{\mathbf{D}}^{at} = -\frac{\left[\mathbf{G}^t \cdot \mathbf{T}_0\right]_{Q=Q_E} \cdot e^{-j\frac{\pi}{4}}}{2\sqrt{2\pi k}\,\sin\beta^{d,at}\left[\left(\hat{\mathbf{s}}^i - \hat{\mathbf{s}}^{d,at}\right)\cdot\hat{\mathbf{t}} - \dfrac{1}{k}\dfrac{\partial\chi^+}{\partial t}\right]} \mathcal{F}\left\{X^E\right\} \tag{16}$$

$$\underline{\mathbf{D}}^{v,at} = \frac{\left|\hat{\mathbf{e}}_1 \times \hat{\mathbf{e}}_2\right| \mathbf{G}^t \cdot \mathbf{T}_0(Q_V)}{4j\pi k\left[\left(\hat{\mathbf{s}}^i - \hat{\mathbf{s}}^v\right)\cdot\hat{\mathbf{e}}_1 - \dfrac{1}{k}\dfrac{\partial\chi^-}{\partial e_1}\right]\left[\left(\hat{\mathbf{s}}^i - \hat{\mathbf{s}}^v\right)\cdot\hat{\mathbf{e}}_2 - \dfrac{1}{k}\dfrac{\partial\chi^-}{\partial e_2}\right]} T\left\{x_1, x_2, w\right\} \tag{17}$$

Similar coefficients, not reported here for the sake of brevity, are obtained for the diffracted rays that compensate for discontinuities of the incident field, i.e. the rays belonging to the "ordinary" Keller's cone. More details can be found in [7].

3.2.3.1 Preliminary validation results

Preliminary validation results are shown in Figure 3 and Figure 4 for a bidirectional reflective/transmissive RIS, configured as an anomalous reflector and anomalous refractor. In both cases, we have a normally incident plane wave, with incident field value $|\mathbf{E}_i|$=1 V/m. In Figure 3, the desired (anomalous) reflection and refraction angles are qr=30° and qt=60°, respectively. In Figure 4, the desired (anomalous) reflection and refraction angles are qr=60° and qt=30°, respectively. The Incident power is equally split between the reflection and the forward (transmission) half-space, in order to satisfy the overall power balance. In both figures, sub-plots (a) represent the re-radiated field computed through numerical solution of the PO integral in (4). Sub-plots (b) are obtained through the ray model, considering edge diffraction only, where the edge diffraction coefficient is modelled according to (13) and (16) for the reflection and transmission half-space, respectively. Finally, in sub-plots (c) also vertex diffraction is added, using the diffraction coefficients of (14) and (17).

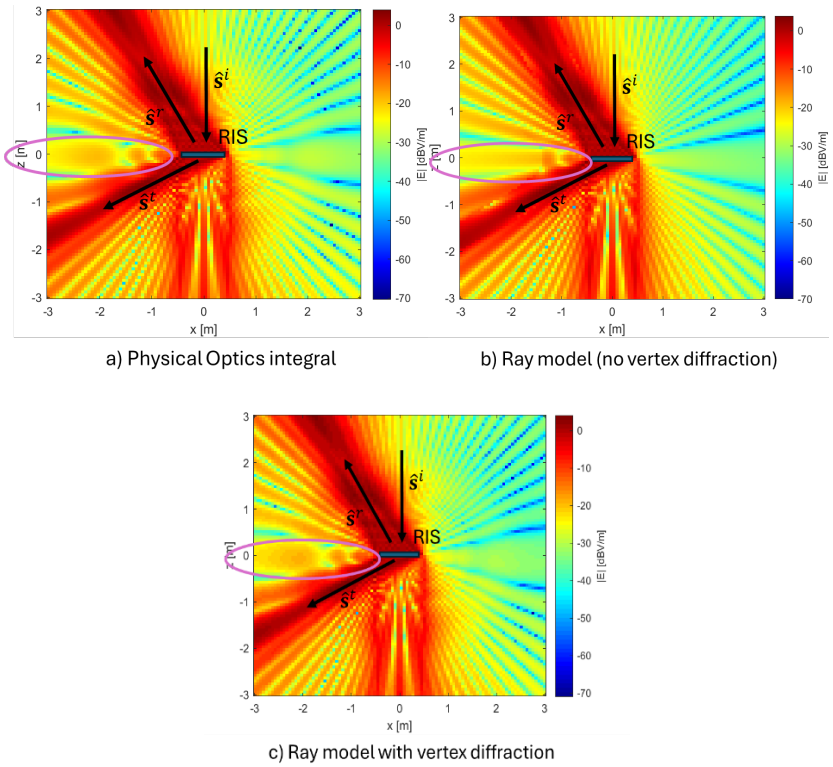

a) Physical Optics integral

b) Ray model (no vertex diffraction)

c) Ray model with vertex diffraction

Figure 3. Visualization of the reradiated field for a bi-directional RIS. Normally incident plane wave with $|\boldsymbol{E}_i|$=1 V/m. Desired anomalous reflection and transmission angles: qr=30°, qt=60°. a) Numerical solution of the PO integral; b) Ray model (only edge diffraction considered); c) Complete ray model (edge and vertex diffraction are considered).

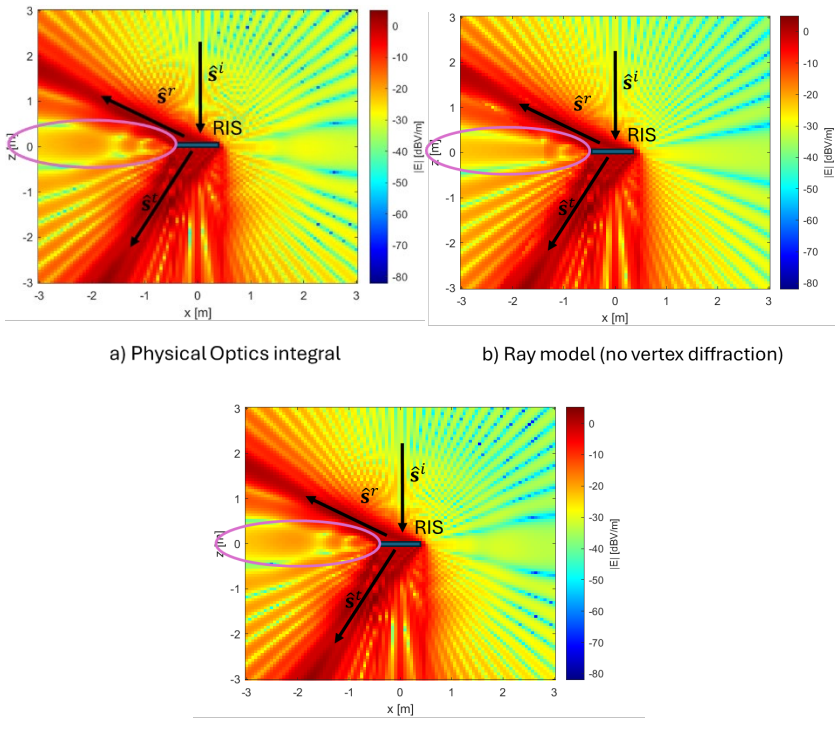

a) Physical Optics integral

b) Ray model (no vertex diffraction)

c) Ray model (with vertex diffraction)

Figure 4. Visualization of the reradiated field for a bi-directional RIS. Normally incident plane wave with $|\boldsymbol{E}_i|$=1 V/m. Desired anomalous reflection and transmission angles: qr=60°, qt=30°. a) Numerical solution of the PO

integral; b) Ray model (only edge diffraction considered); c) Complete ray model (edge and vertex diffraction are considered).

Looking at the results, it can be observed that the ray model, as asymptotic approximation of the PO integral, provides very similar results: however, the computation is about 10 times faster compared to numerical solution of the integral in (4). Moreover, if the vertex diffraction is added in the ray model, results further improve, especially for reradiation at grazing angles from the RIS plane (see for example the region highlighted with magenta ellipses in Figure 3 and Figure 4).

In conclusion, the methodology proposed in [7] allows to overcome the limitations of the ray model introduced in [5] by defining suitable edge and vertex diffraction coefficients for RIS reradiation in both reflection and forward half-spaces, derived through asymptotic approximation of the PO integral. The model can also be applied to the more realistic case of a periodically-modulated RIS with multiple parasitic modes, by iterating the procedure explained above, and relying on a macroscopic SMD coefficient $\underline{\underline{\Gamma}}$ for each of the propagating modes: a further validation has been carried out in this last case, through comparison with full-wave electromagnetic simulation.

Figure 5 shows the simulated scattered field for a phase-gradient reflective RIS configured for a normally incident plane wave, and desired reflection angle q_r=60°. The incident field has intensity $|\mathbf{E}_i|$=1 V/m on the RIS surface, the operating frequency is 3.5 GHz, and the RIS has size 7*D* x 7*D*, where *D* is the modulation period. According to the Floquet's theory, this RIS has 2 parasitic propagating modes at q_r=0° and q_r=−60°, in addition to the desired mode. The black line in Figure 5 shows the reradiated field simulated with the ray model along a semicircle at a distance *r=1 m* from the RIS centre, while the red dashed line is the result obtained with the reference full-wave simulation. As it can be seen from Figure 5, the proposed ray-method can predict the RIS scattering with good accuracy. Overall, the RMS distance between the 2 curves is equal to 0.019, i.e. 1.9 % of the unit incident field.

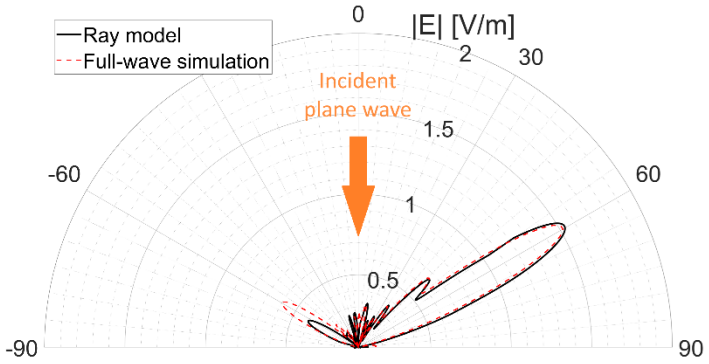

Figure 5. Comparison between ray model and full-wave simulation of the scattered field along a semicircle centred on the RIS, at a distance r=1 m.

3.2.4 Summary and Recommendations

A fully ray-based approach has been introduced for the computation of the re-radiated field by a RIS, both in the far-field and radiative near-field regions. The proposed method is based on an asymptotical approximation of the Physical Optics integral and allows to derive reflection, transmission and diffraction coefficients that are applied to each reradiated ray according to the GO/UTD approach, but it is about one order of magnitude faster than the numerical solution of the integral, despite having a similar accuracy. The model, initially proposed in [5] and described in Deliverable D2.3 [3], has been suitably extended to the case of transmissive RISs, and now includes vertex diffraction that allows more accurate evaluation of the diffracted field, especially for grazing reradiation angles. Being a macroscopic model, it is independent on the RIS technology and only relies on a suitable spatial modulation coefficient that describes the phase and amplitude modulation on each side of the RIS. It can then be applied either to RISs based on the reflectarray/transmitarray technology, or on RISs based on the metasurface technology with electrically small elements. The method can also take into account the effect of multiple

reradiation modes of the RIS (including, for example, parasitic Floquet's modes), simply iterating the method for each mode. Now that the model is complete, it can be integrated into deterministic ray-based field prediction tools to assess the deployment of multiple RISs in a given propagation environment, in order to optimize the planning of RIS-assisted subnetworks.

A preliminary version of the ray model has been implemented into the open-source simulator Sionna Ray Tracing in the framework of a collaboration between 6G-SHINE and CENTRIC projects. However, some of the more advanced functionalities regarding edge and vertex diffraction, as well as the possibility of simulating transmissive RISs are currently missing and will be hopefully added in future releases. More details on the implemented functionalities can be found on the following webpage: Tutorial on Reconfigurable Intelligent Surfaces (RIS) — Sionna 0.19.0 documentation.

3.3 Models for non-diagonal RIS

In contemporary literature, a RIS typically has a diagonal transfer matrix. The diagonal structure emerges since the signal impinging a certain antenna is reflected/re-radiated from the very same antenna. The diagonal form imposes unnecessary limitations, and herein we shall demonstrate that hefty gains are possible by abandoning the diagonal structure.

There is not strict definition of what a RIS is. However, a RIS is typically considered to be a multi-antenna device in which each antenna element, 1) receives an incoming signal, 2) applies a phase shift to said signal, and 3) re-transmits the phase shifted signal. Within a narrowband system model, the input-output relation of such a device may be mathematically described as

$$\boldsymbol{y} = \alpha \mathrm{diag}([e^{J\phi_1}\ e^{J\phi_2}\ \ldots\ e^{J\phi_M}])\boldsymbol{x} \tag{18}$$

where $\boldsymbol{x}$ is the impinging signal on the M antenna elements, ϕ_m the phase shift applied by the m:th antenna, $\boldsymbol{y}$ the re-transmitted signal, $\alpha \leq 1$ a parameter that models various losses of the hardware of the RIS (e.g., insertion losses of the phase shifters), and $\mathrm{diag}(\cdot)$ is a diagonal matrix whose argument appears along the main diagonal. Altogether, we may express this as $\boldsymbol{y} = \boldsymbol{\Theta x}$ where, in the typical case, $\boldsymbol{\Theta}$ is diagonal. An implementation of this is visualized in Figure 6, where the blue boxes are tuneable impedances Z_m. If the impedances are purely reactive, i.e., the resistive components are all zero, then there are no losses and $\alpha = 0$, which, further, implies that $\boldsymbol{\Theta}^{\mathrm{H}}\boldsymbol{\Theta} = \boldsymbol{I}$.

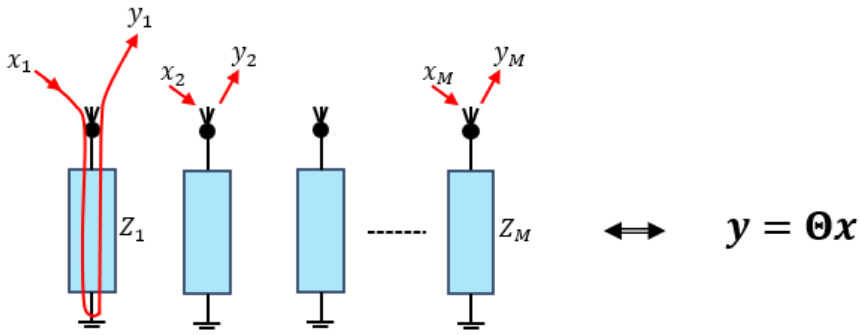

Figure 6. Typical implementation of a diagonal RIS. Blue boxes are tuneable impedances.

To implement a RIS with non-diagonal transfer matrix $\boldsymbol{\Theta}$ can be done in a variety of ways but is in general a far less explored area. However, non-diagonal RISs have some benefits that are not available for diagonal RISs, and in Section 5.1.1 we shall explore the ability of a non-diagonal RIS to mitigate interference on a subnetwork from a neighbour cell. However, before tending to that, we lay down three known implementations for non-diagonal RISs.

In contemporary literature, there are at least three architectures for synthesizing a RIS with a non-diagonal transfer function. One of these (non-diagonal RISs through element permutations) has been partly developed within the 6G-SHINE project and was reported upon in Deliverable D3.2 [1]. The material presented here is an extension of what has been presented in the previous Deliverable, provides simulation results of interference properties of RIS-assisted subnetworks, and highlights the need of tuneable permutation structures.

3.3.1 Non-diagonal RIS implemented as a network-controlled repeater

One method for obtaining a non-diagonal RIs is to implement it as a network-controlled repeater (NCR). NCRs are well explored and standardized by 3GPP [8]. An NCR architecture is depicted in Figure 7.

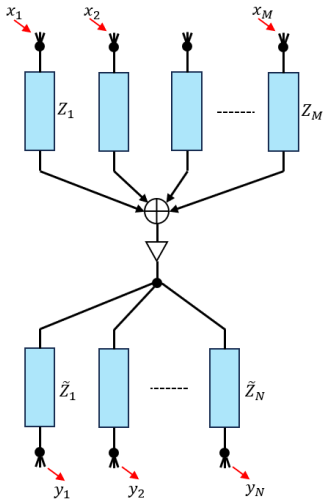

Figure 7. An NCR implementation. Upper antennas are for receiving a signal, and the lower for transmission.

An NCR in its standard form has $M + N$ antenna elements, arranged in two panels, one for receiving and one for transmission. Optionally, a power amplifier may be introduced between the panels. Each antenna is connected to an impedance, Z_m for the receive antennas, and $\tilde{Z}_n$ for the transmit antennas. The phase shifted versions of the received signals are then combined into a single signal, optionally amplified, and then split into N signals. Each of these N signals are phase shifted again and then transmitted. After combining the signals, the input to the power amplifier reads

$$t = \frac{1}{\sqrt{M}} \sum_{m=1}^{M} x_m e^{\jmath \phi_m} = \frac{1}{\sqrt{M}} \boldsymbol{a}(-\boldsymbol{\phi})^{\mathrm{H}} \boldsymbol{x} \tag{19}$$

where the phase shifts ϕ_m are determined by the tuneable (purely reactive) impedances Z_m, the $M \times 1$ vector $\boldsymbol{a}(\boldsymbol{\phi})$ is defined as $\boldsymbol{a}(\boldsymbol{\phi}) = \left[e^{\jmath \phi_1}\ e^{\jmath \phi_2} \ldots\ e^{\jmath \phi_M}\right]^{\mathrm{T}}$, and the impinging signal vector has the form $x = [x_1\ x_2 \ldots x_M]^{\mathrm{T}}$. Thus, the transmitted signal vector $\boldsymbol{y}$ becomes (in the absence of any power amplification)

$$\boldsymbol{y} = \frac{1}{\sqrt{N}} \boldsymbol{a}(\tilde{\boldsymbol{\phi}}) t = \frac{1}{\sqrt{NM}} \boldsymbol{a}(\tilde{\boldsymbol{\phi}}) \boldsymbol{a}(-\boldsymbol{\phi})^{\mathrm{H}} \boldsymbol{x} = \boldsymbol{\Theta} \boldsymbol{x} \tag{20}$$

where, in this case, $\boldsymbol{\Theta} = \boldsymbol{a}(\tilde{\boldsymbol{\phi}}) \boldsymbol{a}(-\boldsymbol{\phi})^{\mathrm{H}} / \sqrt{NM}$. There are two noteworthy properties that differ for an NCR implementation and a diagonal RIS, and we list these next

1. The transfer matrix of an NCR is rank one while that of the diagonal RIS is M.
2. For purely reactive impedances, we have that $\left\|\boldsymbol{\Theta}_{\mathrm{diag}}\right\|^2 = M$ while $\|\boldsymbol{\Theta}_{\mathrm{NCR}}\|^2 = 1$.
3. The NCR is not reciprocal, in the sense that the same impedance configuration cannot be used for the UL as in the DL.

Thus, when there is no direct link between transmitter and receiver, so that the entire communication is forced to go through the NCR, the communication is limited to rank 1 transmissions. The same is not true for a diagonal RIS whose transfer function is full rank. As a remedy, the NCR implementation may be built upon a hybrid beamforming architecture with multiple RF chains.

Further, the NCR can be made to be spatially selective in the sense that the impedances Z_m can be selected in such a way that only signals that impinge the NCR from a certain direction may be re-transmitted. This is a consequence of the fact that the NCR transfer matrix is rank 1, and the same is not true for a diagonal RIS.

Ostensibly, one may regard the second property above as a major drawback for NCRs, since their transfer functions are inherently of lesser energy. However, some elaboration of this shows that it is not really the case. For any input-output relation of the form $\boldsymbol{y} = \boldsymbol{\Theta} \boldsymbol{x}$, we have that $\max \|\boldsymbol{y}\|^2 = \lambda_{\max}(\boldsymbol{\Theta}) \max \|\boldsymbol{x}\|^2$, where $\lambda_{\max}(\boldsymbol{\Theta})$ is the

largest eigenvalue of $\boldsymbol{\Theta}^{\mathrm{H}}\boldsymbol{\Theta}$. However, for a diagonal RIS said largest eigenvalue is unity, despite the fact that its norm $\left\|\boldsymbol{\Theta}_{\mathrm{diag}}\right\|^2 = M$. Likewise, for an NCR, having a rank rank one transfer function, its only eigenvalue equals the norm $\|\boldsymbol{\Theta}_{\mathrm{NCR}}\|^2 = 1$ and thereby coincides with that of the diagonal RIS. Thus, the abilities of a RIS and an NCR to transfer energy are identical.

A clear drawback of NCRs is that they require $2M$ antenna elements (for $N = M$) while a RIS only has M. Further, the number of phase shifters of an NCR is twice that of the RIS, which increases insertion losses. On the other hand, it is a major benefit of NCRs that a single power amplifier is sufficient while a diagonal RIS with amplification would require M amplifiers. Further, the spatial selectivity of NCRs is a clear benefit for interference considerations. Lastly, the diagonal RIS has a clear advantage over the NCR since it is fully reciprocal.

3.3.2 Non-diagonal RISs by (fully) connected impedance networks

Another method to implement a non-diagonal RIS is to introduce further impedances to Figure 6; this method has recently received attention by academia, see for example [9],[10]. An illustration for $M = 3$ antenna elements is shown in Figure 8. In general, antenna elements m and n are connected through impendance Z_{mn}, and impedance Z_{mm} couples antenna element m to a ground plane. According to network theory (see [8]), the input-output relation may be written as $\boldsymbol{y} = \boldsymbol{\Theta}\boldsymbol{x}$ where

$$\boldsymbol{\Theta} = (\boldsymbol{I} + Z_0\boldsymbol{\Upsilon})^{-1}(\boldsymbol{I} + Z_0\boldsymbol{\Upsilon}) \tag{21}$$

In this expression, $\boldsymbol{\Upsilon}$ is the admittance matrix defined as

$$\Upsilon_{mn} = \begin{cases} -Z_{mn}^{-1} & m \neq n \\ Z_{mm}^{-1} + \sum_{k \neq m} Z_{mk}^{-1} & m = n \end{cases} \tag{22}$$

and Z_0 is a reference impedance value, usually set to 50Ω.

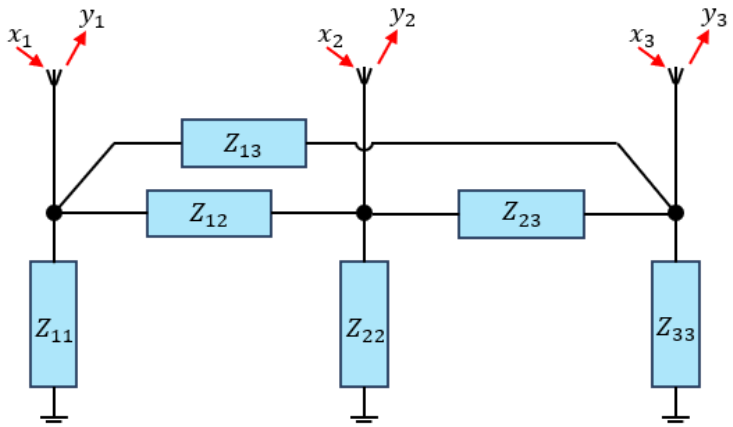

Figure 8. Implementation of non-diagonal RIS from [8] for $M = 3$ antenna elements.

A matrix $\boldsymbol{\Theta}$ of the above form is always symmetric, i.e., $\boldsymbol{\Theta} = \boldsymbol{\Theta}^{\mathrm{T}}$. Moreover, whenever the admittance matrix is purely susceptive, i.e., $Re\{\boldsymbol{\Upsilon}\} = \boldsymbol{0}$ or, equivalently, the impedances are purely reactive, then the matrix $\boldsymbol{\Theta}$ is unitary. The implications of this is that $\lambda_{\max}(\boldsymbol{\Theta}) = 1$ so that the energy transfer ability is no worse than that of NCRs and diagonal RISs. However, for this case we have a gain over both NCRs and diagonal RISs for channels to/from the RIS that have different magnitudes per RIS antenna.

To see this, consider a transmitter and a receiver with a single antenna. The channel from the transmitter to the RIS (column vector) is denoted $\boldsymbol{g}$ and denote the channel from the RIS to the receiver (row vector) by $\boldsymbol{h}$. For a diagonal RIS, the received signal strength at the receiver is at most

$$P_{\text{diag}} = \left| \sum_m |h_m||g_m| \right|^2 \tag{23}$$

while for a non-diagonal RIS we have

$$P_{\text{non-diag}} = \max_{\substack{\boldsymbol{\Theta}:\boldsymbol{\Theta}=\boldsymbol{\Theta}^{\mathrm{T}} \\ \boldsymbol{\Theta}\boldsymbol{\Theta}^{\mathrm{H}}=\boldsymbol{I}}} |\boldsymbol{h}\boldsymbol{\Theta}\boldsymbol{g}|^2 \tag{24}$$

For channels where, e.g., $|g_m| = g$ and $|h_m| = h, \forall m$, we have that $P_{\text{diag}} = P_{\text{non-diag}}$. But for channels with varying amplitude per RIS antenna, this is not the case. For example, with $M = 2$, $\boldsymbol{g} = [1\ 0]^T$, and $\boldsymbol{h} = [0\ 1]$, we readily obtain $P_{\text{diag}} = 0$ while $P_{\text{non-diag}} = 1$ which is achieved for

$$\boldsymbol{\Theta} = \boldsymbol{\Theta}^{\mathrm{T}} = \begin{bmatrix} 0 & 1 \\ 1 & 0 \end{bmatrix} \tag{25}$$

While this is an extreme case, the general result applies: Whenever the channel magnitudes vary across the RIS, a diagonal RIS has performance that is bounded away from that of non-diagonal RIS. In simple words, a non-diagonal RIS has the ability to shuffle energy between the antennas. However, non-diagonal RISs are not fully optimal in this respect due to the constrain $\boldsymbol{\Theta} = \boldsymbol{\Theta}^{\mathrm{T}}$.

Let us summarize. A non-diagonal RIS is superior to a diagonal RIS whenever the channel magnitudes are not constant over the RIS array. However, due to its full rank design, a non-diagonal RIS according to Figure 8 is not spatially selective as any impinging signal will be reflected (although not beamformed). The largest drawback of a non-diagonal RIS is its complicated implementation. A RIS configuration is no longer a phase vector, but a complete set of impedances for all pairs of antenna elements. The latter issue can be somewhat mitigated by methods in [8]. For a practical case in which all impedances can take one out of, say, L values, there appears not to be any publicly available literature on what the losses may be.

3.3.3 Non-diagonal RIS by element permutations

While the non-diagonal RIS models described in Sections 3.3.1 and 3.3.2 are available in literature, the next non-diagonal structure is a novelty within the 6G-SHINE project. In a standard diagonal RIS, a signal impinging a certain antenna element will, after phase shift, leave the RIS from the very same antenna element. In the non-diagonal RISs presented in Sections 3.3.1 and 3.3.2, this is clearly not the case. However, in both of said implementations, an impinging signal on, say, element m re-radiates a fraction of the signal from all antennas (in general). In the non-diagonal structure to be put forth next, this is changed so that the signal impinging antenna m leaves, in its entirety, the RIS from an antenna $m' \neq m$.

In its simplest form, a system model is given in Figure 9. We refer to this type of non-diagonal RIS as permuted RIS, or P-RIS for short. Each antenna element is connected to a circulator, which is in turn connected to an impedance (causing a phase shift). The phase shifted signals from all antennas are then passed on to a permutation; this may be a static or a tuneable permutation. Finally, the permuted signals are fed back to the circulators and then re-radiated from the respective antennas. The input-output relation reads

$$\boldsymbol{y} = \boldsymbol{P}(\sigma)\text{diag}([e^{\jmath\phi_1}\ e^{\jmath\phi_2}\ \dots\ e^{\jmath\phi_M}])\boldsymbol{x} \tag{26}$$

where $\boldsymbol{P}(\sigma)$ is a permutation matrix associated with a permutation σ. Before proceeding any further, we note that the matrix $\boldsymbol{\Theta} = \boldsymbol{P}(\sigma)\text{diag}([e^{\jmath\phi_1}\ e^{\jmath\phi_2}\ \dots\ e^{\jmath\phi_M}])$ is unitary, i.e., it satisfies $\boldsymbol{\Theta}\boldsymbol{\Theta}^{\mathrm{H}} = \boldsymbol{I}$. However, as the permutation is not necessarily symmetric, i.e., $\boldsymbol{\Theta} \neq \boldsymbol{\Theta}^{\mathrm{T}}$, this is not a special case of the construction in Section 3.3.2. For a given permutation σ., finding the optimal phase shift vector $\boldsymbol{\phi}$ is not hard,

$$\begin{aligned} \arg\max_{\boldsymbol{\phi}} |\boldsymbol{h}\boldsymbol{\Theta}\boldsymbol{g}|^2 &= \arg\max_{\boldsymbol{\phi}} \left|\boldsymbol{h}\boldsymbol{P}(\sigma)\text{diag}\left(\left[e^{\jmath\phi_1}\ e^{\jmath\phi_2}\ \dots\ e^{\jmath\phi_M}\right]\right)\boldsymbol{g}\right|^2 = \\ &= \arg\max_{\boldsymbol{\phi}} \left|\tilde{\boldsymbol{h}}\text{diag}\left(\left[e^{\jmath\phi_1}\ e^{\jmath\phi_2}\ \dots\ e^{\jmath\phi_M}\right]\right)\boldsymbol{g}\right|^2 = \left[-\angle\tilde{h}_1 g_1\ \dots\ -\angle\tilde{h}_M g_M\right] \end{aligned} \tag{27}$$

where we defined $\widetilde{\boldsymbol{h}} = \boldsymbol{h}\boldsymbol{P}(\sigma)$. Likewise, finding the best permutation is a trivial task whenever $\boldsymbol{h}$ and $\boldsymbol{g}$ are at hand. It is known from majorization theory that the best permutation is such that the index of the m:th largest (in magnitude) entries of $\widetilde{\boldsymbol{h}}$ and $\boldsymbol{g}$ should coincide (for all $1 \leq m \leq M$).

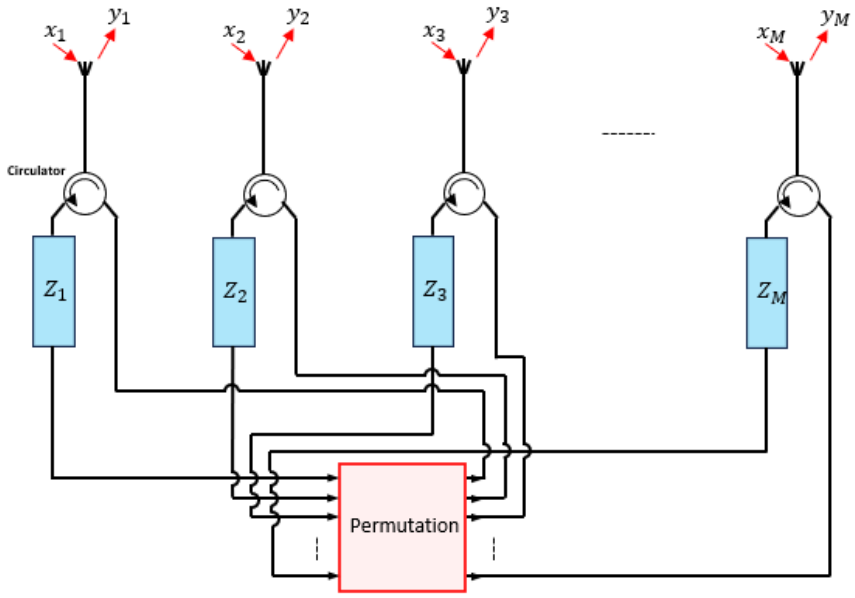

Figure 9. A model of a permuted RIS.

A non-diagonal RIS is not reciprocal in its UL and DL. That is, in general $\boldsymbol{h}\boldsymbol{\Theta}\boldsymbol{g} \neq \boldsymbol{g}^{\mathrm{T}}\boldsymbol{\Theta}\boldsymbol{h}^{\mathrm{T}}$. Moreover, and more crucial, the difference between UL and DL is not limited to, say, a phase shift, and it may very well happen that $\boldsymbol{h}\boldsymbol{\Theta}\boldsymbol{g} \approx 0$ while $|\boldsymbol{g}^{\mathrm{T}}\boldsymbol{\Theta}\boldsymbol{h}^{\mathrm{T}}| \gg 0$. To mitigate this effect, a beam splitting technique has been developed. Let $\boldsymbol{\phi}_{\boldsymbol{hg}}$ be the optimal phase shifts maximizing $\boldsymbol{h}\boldsymbol{\Theta}\boldsymbol{g}$ and let $\boldsymbol{\phi}_{\boldsymbol{hg}}$ be the optimal phase shifts maximizing $\boldsymbol{g}^{\mathrm{T}}\boldsymbol{\Theta}\boldsymbol{h}^{\mathrm{T}}$ (for a fixed permutation). Then, to achieve a reciprocal P-RIS, we propose to use

$$\phi_m^{\mathrm{BS}} = \angle(\mathrm{e}^{\jmath\phi_{\boldsymbol{hg},m}} + \mathrm{e}^{\jmath\phi_{gh,m}}) \tag{28}$$

A full analysis of this construction appears in [11], but we provide its two main properties next, both of which are asymptotically ($M \to \infty$) exact,

1. For $\boldsymbol{\Theta}^{\mathrm{BS}} = \boldsymbol{P}(\sigma)\mathrm{diag}\left(\left[e^{\jmath\phi_1^{\mathrm{BS}}}\ e^{\jmath\phi_2^{\mathrm{BS}}}\ \ldots\ e^{\jmath\phi_M^{\mathrm{BS}}}\right]\right)$, we have $\boldsymbol{h}\boldsymbol{\Theta}\boldsymbol{g} \approx \boldsymbol{g}^{\mathrm{T}}\boldsymbol{\Theta}\boldsymbol{h}^{\mathrm{T}}$ (29)
2. $|\boldsymbol{h}\boldsymbol{\Theta}^{\mathrm{BS}}\boldsymbol{g}|^2 \approx \frac{4}{\pi^2}\left|\boldsymbol{h}\boldsymbol{\Theta}^{\mathrm{hg}}\boldsymbol{g}\right|^2 \left(\approx \frac{4}{\pi^2}\left|\boldsymbol{g}^{\mathrm{T}}\boldsymbol{\Theta}^{\boldsymbol{gh}}\boldsymbol{h}^{\mathrm{T}}\right|^2\right)$ (30)

The first property ensures that the non-diagonal RIS is reciprocal, i.e., the same configuration may be used in the UL as in the DL. The second property gives the cost of ensuring reciprocity, namely, a ≈ 4dB power loss. This loss may be reduced to 3dB if the RIS can control, in addition to phase, also amplitude.

The fact that there are circulators present in Figure 9 is not ideal since they are bulky, costly, and also somewhat leaky. However, they may be dispensed with at essentially no cost. A circulator free implementation is shown in Figure 10. In this implementation, each pair of antennas are directly connected via an impedance, which results in a circulator free implementation, but also in half the number of configurable impedances. Note that this is a static, not reconfigurable permutation σ. If it is desired that the permutation itself should be reconfigurable, then an implementation is shown in Figure 11. In this implementation, we have M antenna ports which are connected to a permutation. Likewise, we have M ports stemming from $M/2$ impedances, which are connected to the same permutation. With that, we establish an overall permutation matrix that is symmetric, i.e., $\boldsymbol{P}(\sigma) = \boldsymbol{P}^{\mathrm{T}}(\sigma)$, but,

and most importantly the permutation implemented in the red box in Figure 11 is not the same permutation as σ in $\boldsymbol{P}(\sigma)$. This may be a little tricky to grasp at first, wherefore we provide a few illuminating examples.

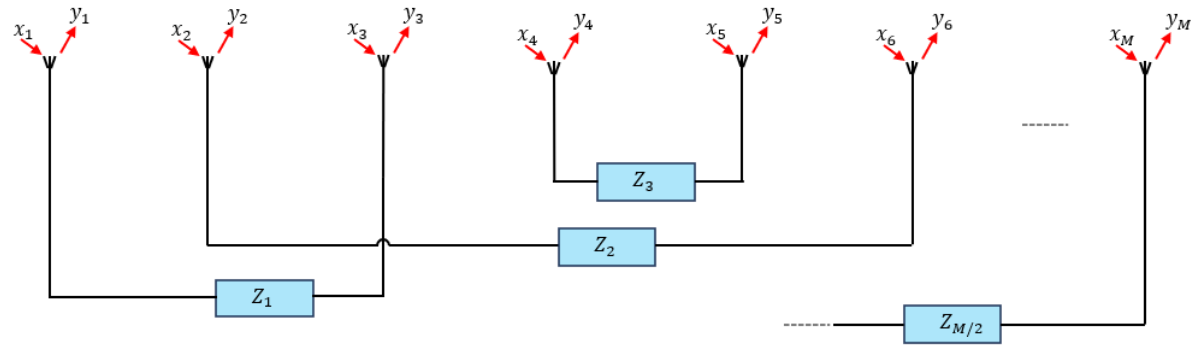

Figure 10. A circulator free P-RIS.

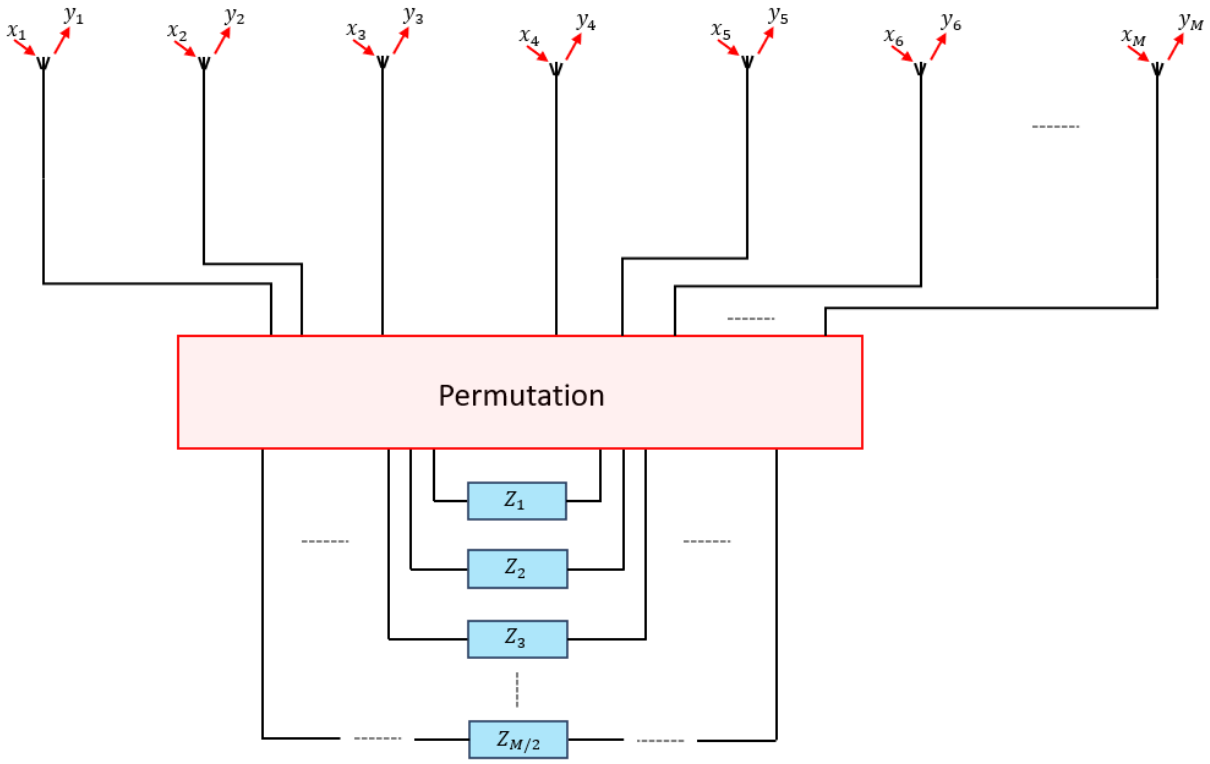

Figure 11. A circulator free P-RIS with reconfigurable permutation.

Example 1. Assume $M = 4$ (for simplicity) and implementations of the red box in Figure 11, namely

$$\sigma' : \{1,2,3,4\} \to \{1,3,2,4\} \text{ and } \{1,2,3,4\} \to \{2,4,3,1\} \tag{31}$$

Then, we obtain P-RISs with symmetric permutations

$$\sigma : \{1,2,3,4\} \to \{4,3,2,1\} \text{ and } \{1,2,3,4\} \to \{3,4,1,2\} \tag{32}$$

whose permutation matrices are

$$\boldsymbol{P}(\sigma) = \begin{bmatrix} 0 & 0 & 0 & 1 \\ 0 & 0 & 1 & 0 \\ 0 & 1 & 0 & 0 \\ 1 & 0 & 0 & 0 \end{bmatrix} \text{ and } \boldsymbol{P}(\sigma) = \begin{bmatrix} 0 & 0 & 1 & 0 \\ 0 & 0 & 0 & 1 \\ 1 & 0 & 0 & 0 \\ 0 & 1 & 0 & 0 \end{bmatrix} \tag{33}$$

This can be readily understood by inspecting Figure 12. For example, in the upper plot, we note that the signal entering antenna port 1, will be inputted to impedance port 1, phase shifted, and transferred to impedance port 4. This port is connected to antenna port 4. However, the signal impinging antenna port 4 will undergo the same route, but in reverse. Therefore, it leaves the RIS from antenna port 1, and a symmetric permutation is obtained.

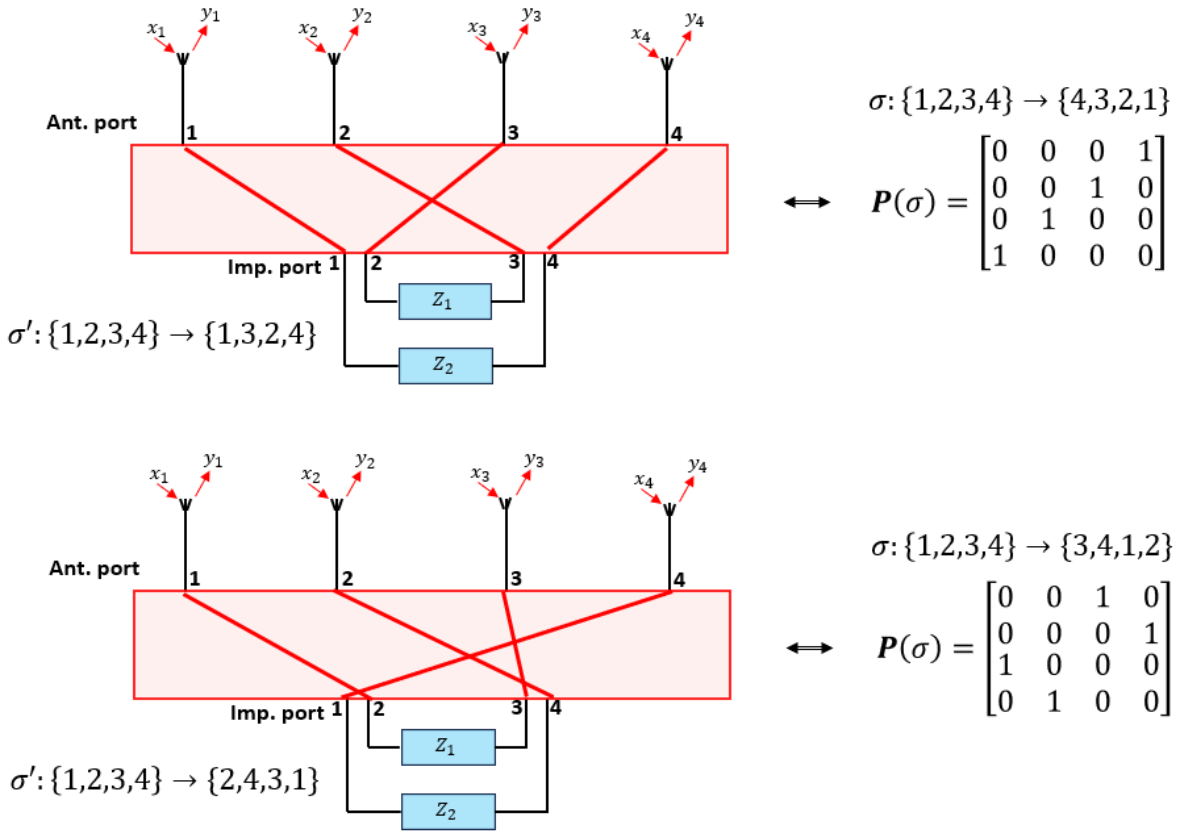

Figure 12. Illustration associated to Example 1.

The fact that the circulator-free implementation only has half the number of impedances is important. This implies that our ability to perform beamforming, i.e., tune the phase shifts ϕ_m reduces. In [11] we have shown that the reduction of phase shifts exacts a beamforming penalty of $4/\pi^2 \approx 4$dB compared with a P-RIS implemented using circulators. However, due to the symmetry of the permutation, the P-RIS is automatically reciprocal. This implies that no beam splitting is required to arrange for reciprocity. But by recalling that beam splitting incurred the very same loss, $4/\pi^2$, we have the result that P-RISs according to and Figure 9 and Figure 11 have equal performance if reciprocity is required. Further, the one from Figure 11 has, 1) half the number of impedances to be tuned, and 2) no circulators. This motivates us to claim that the one in Figure 11 is of superior practical interest.

Similar to the constructions in Sections 3.3.1 and 3.3.2, the P-RIS is also spatially selective and therefore has potential to avoid interference. This is to be studied within a subnetwork scenario in Section 5.1.1. We remark, that a symmetric P-RIS is a special case of the design in Sections 3.3.1-3.3.2, and can therefore not be claimed to be better. However, the P-RIS has far less impedances to be configured and is therefore practically appealing.

3.3.4 Summary

In this section, a model for a non-diagonal RIS through permutations (abbreviated as P-RIS) has been put forth. A P-RIS differs from previously proposed non-diagonal RISs in that, (i) it is full rank (unlike the network-controlled repeater), (ii) it has a transfer function in which exactly one element per row takes a non-zero value (unlike an impedance network RIS). The P-RIS has far less parameters to be controlled than the impedance network RIS, but

comes at the price of a, preferably, tuneable permutation. A number of different implementation forms of a P-RIS has been put forth, and we lean against that the symmetric version (illustrated in Figure 11) is the way forward (implementation complexity vs. performance trade-off).

As a subnetwork is meant to co-exist with other communication entities, interference may be problematic. The rationale of the P-RIS design is to allow for a control of said interference. With that said, an investigation of potential interference mitigation benefits of a P- RIS have not been investigated in this section but is deferred to Section 4.

3.4 Wide beam creation using a RIS

In many scenarios it is of interest to force a RIS to reflect with a wide beam. For example, in a subnetwork it is potentially of interest to install a RIS that is not reconfigurable, but then let it serve the entire area of the subnetwork.

Unfortunately, wide beams are not so easy to create. One issue is that if the RIS beam is designed (i.e., selecting the phase change pattern) to link AoA θ and AoD φ optimally, then the beam gets narrower as the number of antennas at the RIS, M, increases. With, say 4 antennas, a RIS beam designed to link AoA θ and AoD φ would in fact link AoA $\theta + \delta_A$ and AoD $\varphi + \delta_D$ for fairly large values of δ_A and δ_D. However, this drastically changes when M is, say, 64. Now, the values of δ_A and δ_D are grossly smaller. At the same time, these optimal narrow beams are by far easiest to design, and wide beams are more cumbersome. So, a very relevant problem can be posed as "how to generate a wide RIS beam for large M?".

For a normal antenna array, i.e., not a RIS, a very elegant and efficient solution to this problem exists, see [12] and [13]. This technique is not directly applicable to RIS, but an attempt to do so is published in [14]. However, the method in [14] lacks a critical component; we get back to its drawback shortly.

Before extending the method of [12] and [13] to RIS, we explain the method. The approach for traditional beamforming is to make use of dually polarized antennas at both the transmitter (tx) and the receiver (rx). Note that for traditional beamforming, there is no RIS. Let us assume M vertically polarized antenna elements and M horizontally polarized antenna elements at the tx. Assume further that a phase change pattern to be applied at these 2M antennas have been found. Denote the phase values to be applied at the horizontally polarized antennas by $\boldsymbol{w}_{A,1}$ and the phase values to be applied at the vertical polarized antennas by $\boldsymbol{w}_{B,1}$; both of these are $Mx1$ vectors and notation follows [14]. Let the radiation pattern created (azimuth only) be denoted by $P(\theta)$ where θ is the AoD as seen from the tx. Further, if M is small, the beam is fairly wide. Crucially, this radiation pattern is calculated by measuring the received power in both polarizations, and then summing the result.

Now assume that a pattern for an array comprising 2M vertically polarized antenna elements and 2M horizontally polarized antenna elements should be designed. The method in [12],[13] is to first define

$$\boldsymbol{w}_{A,2} = -J_M \boldsymbol{w}_{B,1}^* \quad and \quad \boldsymbol{w}_{B,2} = J_M \boldsymbol{w}_{A,1}^* \tag{34}$$

Where "*" is complex conjugation and J_M is an MxM matrix with ones along its main antidiagonal and zeros elsewhere. Now, the phase patterns to be applied at the 2M horizontally and vertically polarized antennas are

$$\boldsymbol{w}_A = [\boldsymbol{w}_{A,1}^T \quad \boldsymbol{w}_{A,2}^T]^T \quad \boldsymbol{w}_B = [\boldsymbol{w}_{B,1}^T \quad \boldsymbol{w}_{B,2}^T]^T, \tag{35}$$

respectively. Most elegantly, the radiation pattern that emerges from this design is precisely $2P(\theta)$. That is, the shape of the beam remains the same as for a total of 2M antennas, but a power gain of 3dB is achieved. Since the pattern for 2M antennas is fairly wide, the beam for 4M antennas is accordingly so. The process above can then be iterated until a pattern of the desired length is achieved. E.g., if we start out with 4 antennas, a "narrow" beam

for 4 antennas is easy to obtain, and in fact not so "narrow" after all since it was constructed for 4 antennas only. If we apply the above technique 4 times, we obtain the exactly the same radiation pattern with 64 antennas as for 4, but with a power gain of 16 (=12 dB).

The issue of extending the method to RISs, is that there may exist a polarization rotation between the tx and the RIS. If countermeasures are not taken, such rotation ruins the entire method, and the extension in [14] did not take it into account.

We start by describing how a straightforward extension would materialize, i.e., one which does not take any polarization rotation into account.

3.4.1 No polarization rotation between tx and RIS

We shall assume that there is no polarization rotation between the tx and the RIS; that is, the signal sent by the vertically polarized antennas at the tx arrives solely at the vertically polarized antennas at the RIS, and (similar for the horizontally polarized). We assume that two ports at the tx, one for vertical polarization and one for horizontal polarization. Further, we assume that the same signal is sent from both ports, and we denote this signal by x (a scalar). With that, the received signals ($Mx1$ vectors) at the vertical and horizontal antennas at the RIS are (in the absence of noise)

$$r_A = x\boldsymbol{a}(\theta) \quad and \quad r_B = x\boldsymbol{a}(\theta) \tag{36}$$

where $a_A(\theta)$ and $a_B(\theta)$ are steering vectors that specify the LOS propagation channel between tx and RIS, and where θ denotes the AoA at the RIS (we are a bit sloppy with notation here, and θ could be a pair of azimuth and elevation angles). Similarly, the channels from the vertically and horizontally polarized RIS antennas to the dually polarized receive beam at the rx are identical for both polarizations and denoted by $b(\varphi)$ (a $1xM$ vector). At each RIS antenna, a phase change can be applied. With that, the received signals at the rx are

$$\begin{bmatrix} z_A \\ z_B \end{bmatrix} = \begin{bmatrix} \boldsymbol{b}^T(\varphi) & \boldsymbol{0}_{1xM} \\ \boldsymbol{0}_{1xM} & \boldsymbol{b}^T(\varphi) \end{bmatrix} \begin{vmatrix} w_{A,1} & 0 & \cdots & 0 \\ 0 & w_{A,2} & 0 & \vdots \\ \vdots & 0 & \ddots & 0 \\ 0 & \cdots & 0 & w_{A,M} \end{vmatrix} \begin{vmatrix} w_{B,1} & 0 & \cdots & 0 \\ 0 & w_{B,2} & 0 & \vdots \\ \vdots & 0 & \ddots & 0 \\ 0 & \cdots & 0 & w_{B,M} \end{vmatrix} \begin{bmatrix} \boldsymbol{a}(\theta) & \boldsymbol{0}_{Mx1} \\ \boldsymbol{0}_{Mx1} & \boldsymbol{a}(\theta) \end{bmatrix} x \tag{37}$$

Assume now that the phase patterns $\boldsymbol{w}_A = [w_{A,1} \ldots w_{A,M}]$ and $\boldsymbol{w}_B = [w_{B,1} \ldots w_{B,M}]$ are given. The reflection pattern is calculated, for $x = 1$, as

$$P(\theta, \varphi) = |z_A|^2 + |z_B|^2 \tag{38}$$

Our goal is now to find two vectors $\tilde{\boldsymbol{w}}_A$ and $\tilde{\boldsymbol{w}}_B$ of twice the lengths, i.e., $2M$, such that the new reflection pattern satisfies $\tilde{P}(\theta, \varphi)$

$$\tilde{P}(\theta, \varphi) = 2P(\theta, \varphi) \tag{39}$$

But before we put forth our solution, we mention how w_A and w_B are typically found. The RIS designer assumes a pair of angles (θ_1, φ_1) and sets $\boldsymbol{w}_A = \boldsymbol{w}_B = \boldsymbol{a}^*(\theta_1) \circ \boldsymbol{b}^*(\varphi_1)$ where $\circ$ denotes Hadamard (elementwise) multiplication. This results in $P(\theta_1, \varphi_1) = 4M^2$ while $P(\theta, \varphi)$ is much smaller for (θ, φ) not being "close" to (θ_1, φ_1).

Inspired by [12], we have found that the following solves the problem. Define

$$\boldsymbol{w}_{A,2} = -J_M \boldsymbol{w}_B^* \quad and \quad \boldsymbol{w}_{B,2} = J_M \boldsymbol{w}_A^*. \tag{40}$$

Then,

$$\tilde{\boldsymbol{w}}_A = [\boldsymbol{w}_A^T \quad \boldsymbol{w}_{A,2}^T]^T \qquad \tilde{\boldsymbol{w}}_B = [\boldsymbol{w}_B^T \quad \boldsymbol{w}_{B,2}^T]^T, \tag{41}$$

results in $\tilde{P}(\theta, \varphi) = 2P(\theta, \varphi)$, which is the desired goal at the outset.

3.4.2 Polarization rotation between tx and RIS

In realistic cases, there is likely a polarization rotation between the tx and the RIS. Assume that the tx transmits the signal $\boldsymbol{x} = [x_A \quad x_B]^T$ from its two antenna ports (one per polarization). With polarization rotation, the transfer function, not accounting for any steering vector, between the tx and the polarizations at the RIS is

$$R(\vartheta) = \begin{bmatrix} \cos\vartheta & -\sin\vartheta \\ \sin\vartheta & \cos\vartheta \end{bmatrix} \tag{42}$$

which implies that the received signal at the RIS reads

$$\boldsymbol{r}_A = (x_A \cos\vartheta - x_B \sin\vartheta)\boldsymbol{a}(\theta) \quad \text{and} \quad \boldsymbol{r}_B = (x_A \sin\vartheta + x_B \cos\vartheta)\boldsymbol{a}(\theta) \tag{43}$$

so that the signal at the rx reads

$$\begin{bmatrix} z_A \\ z_B \end{bmatrix} = \begin{bmatrix} \boldsymbol{b}^T(\varphi) & \boldsymbol{0}_{1xM} \\ \boldsymbol{0}_{1xM} & \boldsymbol{b}^T(\varphi) \end{bmatrix} \begin{bmatrix} w_{A,1} & 0 & \cdots & 0 & & & & \\ 0 & w_{A,2} & 0 & \vdots & & & & \\ \vdots & 0 & \ddots & 0 & & & & \\ 0 & \cdots & 0 & w_{A,M} & & & & \\ & & & & w_{B,1} & 0 & \cdots & 0 \\ & & & & 0 & w_{B,2} & 0 & \vdots \\ & & \ddots & & \vdots & 0 & \ddots & 0 \\ & & & & 0 & \cdots & 0 & w_{B,M} \end{bmatrix} \begin{bmatrix} \boldsymbol{a}(\theta) & \boldsymbol{0}_{Mx1} \\ \boldsymbol{0}_{Mx1} & \boldsymbol{a}(\theta) \end{bmatrix} R(\vartheta) \begin{bmatrix} x_A \\ x_B \end{bmatrix} \tag{44}$$

It can be seen that

$$\boldsymbol{B}(\varphi, \theta) = \begin{bmatrix} \boldsymbol{b}^T(\varphi) & \boldsymbol{0}_{1xM} \\ \boldsymbol{0}_{1xM} & \boldsymbol{b}^T(\varphi) \end{bmatrix} \begin{bmatrix} w_{A,1} & 0 & \cdots & 0 & & & & \\ 0 & w_{A,2} & 0 & \vdots & & & & \\ \vdots & 0 & \ddots & 0 & & & & \\ 0 & \cdots & 0 & w_{A,M} & & & & \\ & & & & w_{B,1} & 0 & \cdots & 0 \\ & & & & 0 & w_{B,2} & 0 & \vdots \\ & & \ddots & & \vdots & 0 & \ddots & 0 \\ & & & & 0 & \cdots & 0 & w_{B,M} \end{bmatrix} \begin{bmatrix} \boldsymbol{a}(\theta) & \boldsymbol{0}_{Mx1} \\ \boldsymbol{0}_{Mx1} & \boldsymbol{a}(\theta) \end{bmatrix} \tag{45}$$

is diagonal. Therefore, if we can guarantee that $R(\vartheta)\begin{bmatrix} x_A \\ x_B \end{bmatrix}$ have equal amplitude in its two components, then the same reflection pattern would emerge. This is indeed possible by noting that $R(\vartheta)$ is a rotation matrix wherefore the vectors [1;i] and [1; -i] are eigenvectors. Thus, using one of these two vectors as sounding vectors would not alter the reflection pattern. Or in other words, when creating a wide beam from the RIS, the method of [12],[13] can be applied, but the data must be pre-multiplied by either [1;i] or [1; -i]. The paper [14] failed to realize this.

3.4.3 Numerical examples

Consider a dually polarized linear RIS-array comprising $M = 4$ elements and reflecting its signals towards an angle of 15^o. The resulting reflection pattern is visualized by the dashed curves in Figure 13. We may observe that the reflection pattern is identical for both polarizations. In the case of no polarization rotation between the tx and the RIS, the results for a RIS with a wide beam and $M = 8$ are shown by the solid curves. AS can be seen, the reflection

pattern is now different for the two polarizations, but their sum has the same shape as that for $M = 4$. Thus, a wide beam has been created. If a larger M is used, say $M = 64$, the same pattern would emerge again, but scaled according to the antenna number.

In Figure 14 we consider a polarization rotation of 50° and $M = 8$. The dashed curve is the RIS reflection pattern in case of a linearly polarized signal $[1\ 1]^{\mathrm{T}}$. Due to the polarization rotation, the reflection pattern is no longer wide (it is not a scaled version of the black dashed curve of Figure 13). However, if the tx is adopting circularly polarized signals, the solid curve emerges, which is indeed constituting a wide beam.

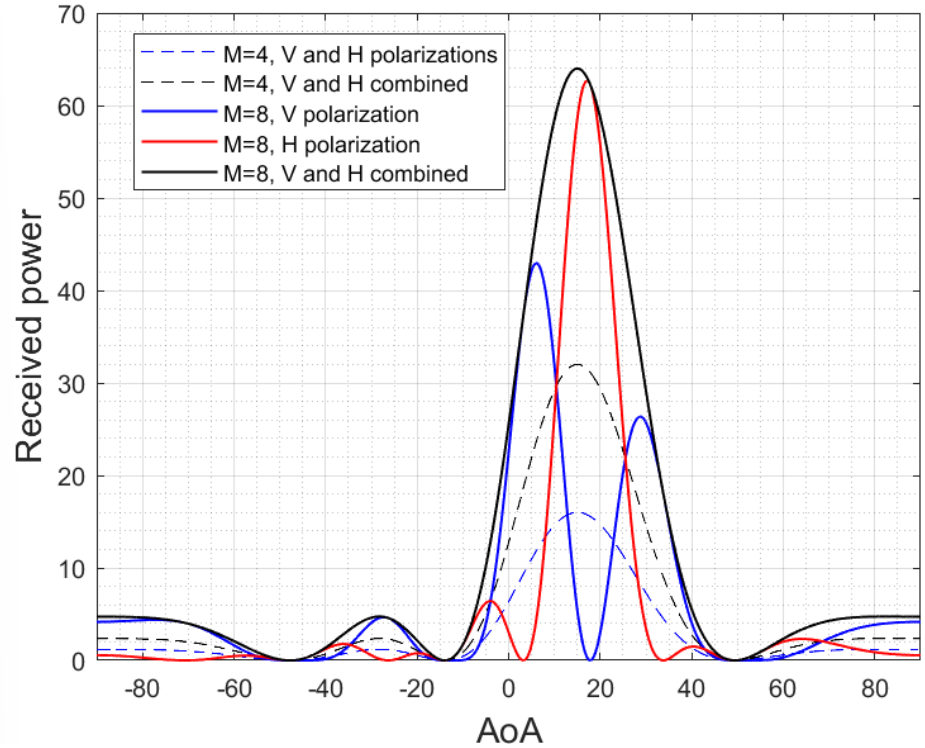

Figure 13. Dashed curves are for $M = 4$ while solid curves are with $M = 8$. No polarization rotation. The black curve for $M = 8$ represents a wide beam as it has the same shape as that for $M = 4$.

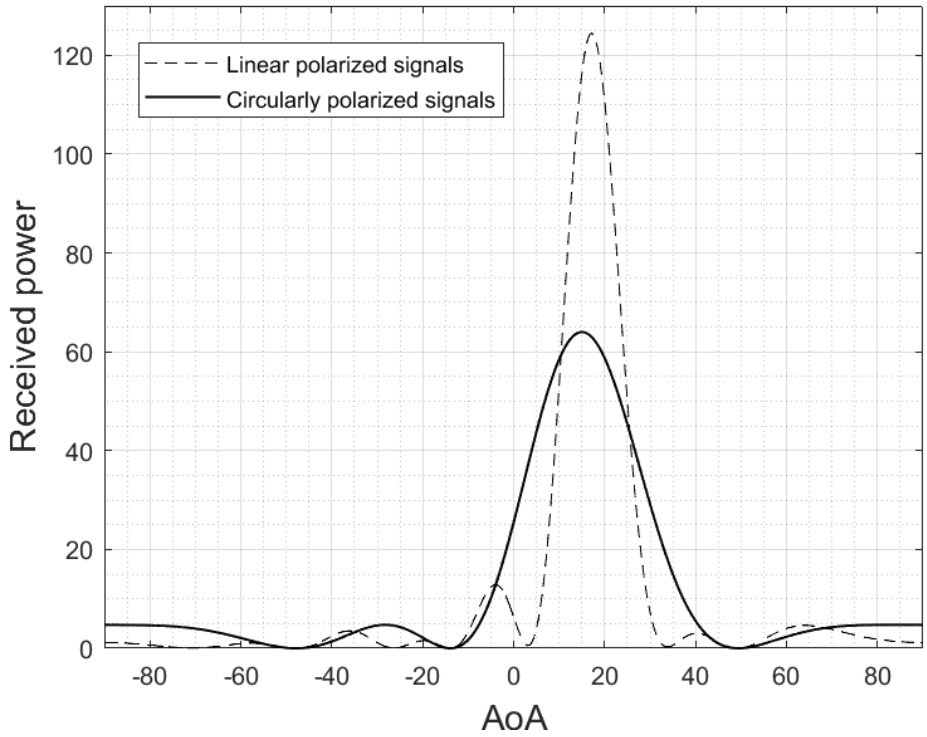

Figure 14. Results for polarization rotation between the tx and the RIS. For linearly polarized signals (dashed) transmitted from the tx, the RIS reflection pattern is no longer representing a wide beam. The solid line adopts circular polarization and represents a wide beam.

3.4.4 Summary and recommendations

Beam management for RIS-assisted systems imposes a severe burden on a subnetwork. Therefore, an appealing choice is to let a single RIS serve an entire subnetwork. The typical small dimension of a subnetwork makes this argument even stronger. To cover the subnetwork, the RIS should adopt a beam that is sufficiently wide to cover the entire subnetwork. This is, however, not easy to accommodate as a RIS with many antennas typically forces its beam to become narrow. In this project we have extended a method for synthesizing wide beams for antenna arrays into a RIS framework. The extension is straightforward, but hinges upon a need for adopting circularly polarized signals at the transmit side. Earlier attempts have been made in the literature, but the need for circular polarization has not been reported in earlier literature. Altogether, implementing a subnetwork with a single RIS with a static wide beam appears most promising in situations where minimal RIS control is desired.

3.5 Low-CSI overhead RIS design using a multiport network model

3.5.1 Introduction

In RIS-aided communications, estimation of the cascaded channel from the User Equipment (UE) to RIS and from the RIS to the BS, is essential for effective phase-shift design and harnessing the benefits offered by RIS technology. However, this task is complex, mainly due to the passive characteristics of the RIS and the complexities posed by high-dimensional channels. Indeed, since all RIS elements are passive and cannot transmit, receive, or process any pilot signals, Channel State Information (CSI) estimation must be performed by a central controller, such as the BS. This incurs significant overhead compared to standard MIMO systems, as it requires substantial resources to estimate the channel. Specifically, research in this field has so far pursued two main approaches. On one hand,

known as *Single time-scale CSI and RIS optimization*, methods have been developed to facilitate instantaneous channel estimation. This is achieved by transmitting pilot signals and subsequently configuring the RIS based on predetermined patterns at a timescale matching the channel coherence time. In this vein, approaches such as those in [15],[16],[17],[18] aim to minimize the number of pilot symbols, while approaches in [19],[20] address the same problem in the presence of electromagnetic interference. A diagram summarizing this type of approaches is shown in Figure 15 (a).

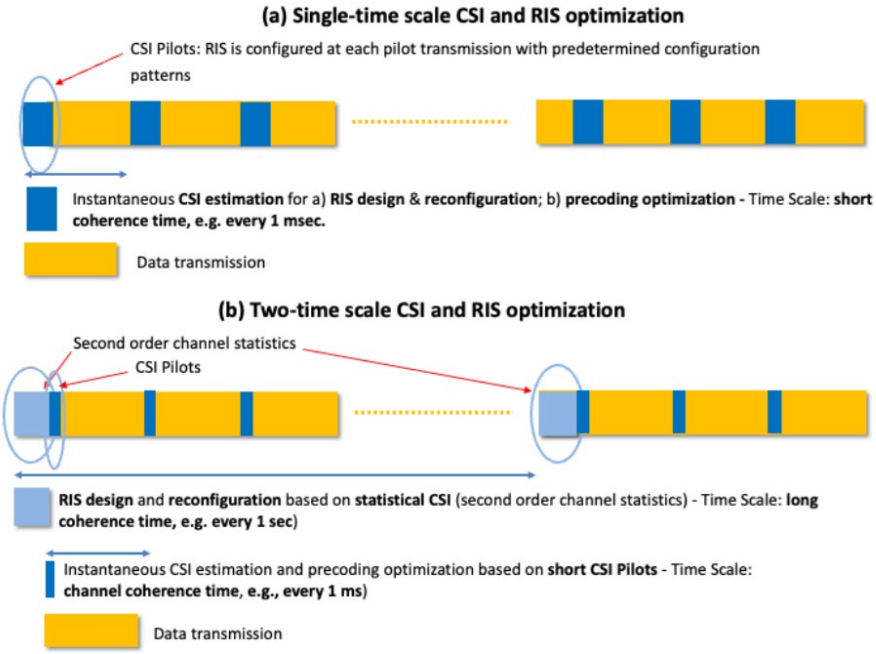

Figure 15. Possible approaches for RIS optimization

However, considering the dynamic nature of the wireless channel and user mobility, optimizing a RIS within a timescale aligned with the coherence time of the channel can be challenging. This is especially true in highly dynamic environments. To address these open research issues, another approach proposed in the literature does not strictly depend on perfect CSI knowledge for RIS optimization. In particular, the RIS is optimized based on the statistical CSI of all links, which operates on a long timescale, effectively reducing the CSI overhead. Estimation of the statistical CSI can be conducted through large time-scale sensing, as proposed in [21], or by leveraging localization information, as suggested in [22]. These approaches can be referred to as *Two-time-scale CSI and RIS optimization* and are summarized in Figure 15(b). The key advantage of this approach is that the RIS can be optimized without the need for repeated reconfigurations with predetermined patterns. Furthermore, the information necessary for RIS optimization can be obtained sporadically. This information may be known beforehand, such as knowledge of UEs confined to a specific area. It can also be learned occasionally during system operation, using a localization infrastructure.

In this work considers a scenario of a subnetwork (SN) in which a certain number of subnetwork entities (SNE) need to communicate with a high-capabilities (HC) controller. The communication is supported by a RIS that is modelled using a physically consistent multi-port (MP) network model that addresses several factors often overlooked by traditional RIS models in communication theory. These include the mutual coupling among scattering elements and the presence of structural scattering. The model and the difference with respect to traditional models used in the literature of RIS is reported in [23].

The dimensions of the scenario are assumed to be on the order of several meters, leading to propagation conditions that lie at the boundary between the near-field and far-field, typical for example of a consumer subnetwork scenario, such as indoor interactive gaming, or an industrial sub-network, such as robot control. Specifically, the problem studied is where the RIS is tasked with supporting the communication of a node, ensuring

it the maximum average bit rate in the presence of interference from other nodes, given that only statistical information about the node positions is known, but not the channel.

3.5.2 System model

The scenario considered generally refers to a subnetwork in a typically indoor environment which, as previously discussed, can adapt to different scenarios considered in the project where communication between SNE and HC occurs, supported by a RIS. Hence, we consider a wireless scenario in which a single-antenna SNE must establish a communication link with an HC equipped with *N* antennas. In this setting, a RIS is present to support the communication of the targeted SNE, while N_u - 1 other users also exist, acting as interferers for that node. Our primary focus is on examining the capabilities of the RIS to enhance the link quality for the intended SNE while simultaneously mitigating interference from the other users. This analysis is performed with only statistical knowledge of the channels to all involved nodes. The reference scenario may involve the interfering nodes communicating with another HC or with the same HC without the assistance of the RIS or potentially utilizing a different RIS.

The RIS is equipped with M passive reconfigurable elements, and, without loss of generality, we designate the first SNE as the reference user. Thus, in the described scenario, the goal of the RIS is to maximize the average data rate of the first SNE while the users *i*, where *i* = 2, …, N_u, function as interferers. A graphical representation of the scenario is shown in Figure 16. Neglecting the direct link between the SNEs and the HC, i.e., assuming that such links are blocked and therefore require the assistance of a RIS, the signal received at the HC can be expressed as:

$$\boldsymbol{y} = \boldsymbol{\phi}(\boldsymbol{b})\boldsymbol{x} + \boldsymbol{\phi}(\boldsymbol{b}) \sum_{i=2}^{N_u} \boldsymbol{w}_i + \boldsymbol{n}, \tag{46}$$

where $\boldsymbol{x}$ is the combination of the transmitted information from the first user and channel $\boldsymbol{t}_1$, while $\boldsymbol{w}_i$ is the combination of the transmitted information from the *i*-th user and the channel. Note that model (46) is based on the assumption of narrowband transmissions, meaning that the coherence bandwidth of the channel is greater than the bandwidth of the signal. This assumption is justified by the fact that, as shown in studies conducted within WP2 of the 6G-SHINE project and described in the deliverable D2.3 in short-range indoor factory scenarios to which we refer, the delay spread stabilizes at values of a few tens of nanoseconds. Therefore, the coherence bandwidth is on the order of 50-100 MHz, a value that can be considered sufficiently large to assume narrowband transmissions.

The term $\boldsymbol{n}$ in (46) denotes the noise, and $\boldsymbol{\phi}(\boldsymbol{b}) = \boldsymbol{S}\boldsymbol{\Delta}(\boldsymbol{b})$ refers to the combination of the RIS-HC channel $\boldsymbol{S}$, which is assumed to be known since the NC and the RIS are considered to be fixed, and the response of the RIS $\boldsymbol{\Delta}(\boldsymbol{b})$ defined according to the model in [23]:

$$\boldsymbol{\Delta}(\boldsymbol{b}) = -2Y_0(\boldsymbol{Z_{SS}} + \boldsymbol{r_0 I_M} + j\, diag(\boldsymbol{b}))^{-1} \tag{47}$$

Here, $\boldsymbol{Z_{SS}}$ denotes the MxM matrix of self and mutual impedances of the RIS, $\boldsymbol{b}$ are tunable reactances connected at the RIS ports, r_0 represents a small parasitic resistance, $\boldsymbol{I_M}$ stands for the identity matrix, and Y_0 is a reference admittance.

The assumption of statistical CSI corresponds to assuming that the HC knows the correlations:

$$\boldsymbol{R_x} = E(\boldsymbol{x}\boldsymbol{x}^H) = \sigma_1^2\, \boldsymbol{R_{t_1}} \tag{48}$$

$$\boldsymbol{R_{w_i}} = E(\boldsymbol{w}_i\boldsymbol{w}_i{}^H) = \sigma_i^2\, \boldsymbol{R_{t_i}} \tag{49}$$

but nor the instantaneous channels $\boldsymbol{t}_i$. Estimation of the correlations can be conducted through large time-scale sensing, as proposed in [21], or by leveraging localization information, as suggested in [22].

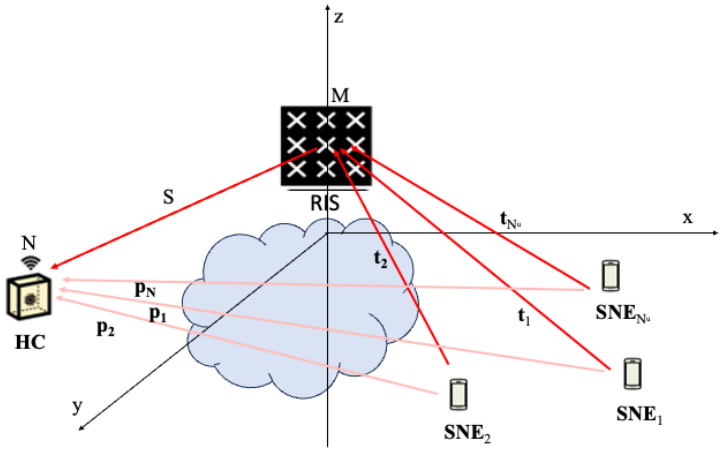

Figure 16. The considered scenario for statistical CSI estimation and rate maximization in the presence of interference

3.5.3 RIS optimization

For the purpose of optimizing the RIS, we consider the worst-case bound presented in [24] to evaluate the ergodic achievable uplink rate in the presence of interference, based on the assumption of uncorrelated additive interference and noise. Accordingly, denoting by **v** the combining vector at the HC, we can write the following expression for the ergodic uplink rate:

$$R(\boldsymbol{b},\mathbf{v}) = E_{\boldsymbol{t}_1}\left[log_2\left(1+\frac{\sigma_1^2\mathbf{v}^H\boldsymbol{\phi}(\boldsymbol{b})\boldsymbol{t}_1\boldsymbol{t}_1^H\boldsymbol{\phi}^H(\boldsymbol{b})\mathbf{v}}{\mathbf{v}^H\left(\boldsymbol{\phi}(\boldsymbol{b})\sum_{i=2}^{N_u}\boldsymbol{R}_{\boldsymbol{w}_i}\boldsymbol{\phi}^H(\boldsymbol{b})+\sigma_n^2 I_N\right)\mathbf{v}}\right)\right] \tag{50}$$

To elaborate from (50), we consider the upper bound $R_b \geq R$ of the rate derived from the concavity of the logarithm function, where:

$$R_b(\boldsymbol{b},\mathbf{v}) = log_2\left(1+E_{\boldsymbol{t}_1}\left(\frac{\sigma_1^2\mathbf{v}^H\boldsymbol{\phi}(\boldsymbol{b})\boldsymbol{t}_1\boldsymbol{t}_1^H\boldsymbol{\phi}^H(\boldsymbol{b})\mathbf{v}}{\mathbf{v}^H\left(\boldsymbol{\phi}(\boldsymbol{b})\sum_{i=2}^{N_u}\boldsymbol{R}_{\boldsymbol{w}_i}\boldsymbol{\phi}^H(\boldsymbol{b})+\sigma_n^2 I_N\right)\mathbf{v}}\right)\right)$$

$$= log_2\left(1+\frac{\mathbf{v}^H\boldsymbol{\phi}(\boldsymbol{b})\boldsymbol{R}_{\boldsymbol{x}}\boldsymbol{\phi}^H(\boldsymbol{b})}{\mathbf{v}^H\left(\boldsymbol{\phi}(\boldsymbol{b})\sum_{i=2}^{N_u}\boldsymbol{R}_{\boldsymbol{w}_i}\boldsymbol{\phi}^H(\boldsymbol{b})+\sigma_n^2 I_N\right)\mathbf{v}}\right), \tag{51}$$

which can be maximized by maximizing the argument of the log. We are then in the position to formulate the optimal joint RIS/combiner design as:

$$(\boldsymbol{b}^*,\mathbf{v}^*) = \text{argmax}_{\mathbf{b},\mathbf{v}}\frac{\mathbf{v}^H\boldsymbol{\phi}(\boldsymbol{b})\boldsymbol{R}_{\boldsymbol{x}}\boldsymbol{\phi}^H(\boldsymbol{b})}{\mathbf{v}^H\left(\boldsymbol{\phi}(\boldsymbol{b})\sum_{i=2}^{N_u}\boldsymbol{R}_{\boldsymbol{w}_i}\boldsymbol{\phi}^H(\boldsymbol{b})+\sigma_n^2\boldsymbol{I}_N\right)\mathbf{v}} \tag{52}$$

The proposed approach is based on alternating optimization (AO). Specifically, a three-steps algorithm is proposed in which, in addition to the two variables **v** and ***b*** present in (52)(52) there is an auxiliary variable $\boldsymbol{\Lambda}$ that will be introduced later. These variables are alternately optimized, i.e., one of the three variables is optimized assuming the other two fixed. To start, let's consider being at iteration *k* of the AO algorithm, and we denote by $\mathbf{v}^{(k)}$ and $\boldsymbol{b}^{(k)}$ the values of **v** and ***b*** found at iteration *k*. Then, a method is derived for computing $\boldsymbol{b}^{(k+1)}$ with the precoder fixed to $\mathbf{v}^{(k)}$, which for simplicity of notation is simply denoted as **v.** To elaborate, we consider the eigen-decomposition $\boldsymbol{R}_{\boldsymbol{x}} = \boldsymbol{U}\boldsymbol{D}\boldsymbol{U}^H$. Since $\boldsymbol{R}_{\boldsymbol{x}}$ is positive semidefinite, the diagonal matrix $\boldsymbol{D}$ has real non-negative entries. Then, we introduce the auxiliary vector $\boldsymbol{\Lambda}$ and the error function:

$$\varepsilon_r(\boldsymbol{\Lambda}, \boldsymbol{b}, \mathbf{v}) = \mathrm{tr}\left\{\boldsymbol{\Lambda}\left[\mathbf{v}^H\left(\boldsymbol{\phi}(\boldsymbol{b})\left(\boldsymbol{R}_{\boldsymbol{x}} + \sum_{i=2}^{N_u}\boldsymbol{R}_{\boldsymbol{w}_i}\right)\boldsymbol{\phi}^H(\boldsymbol{b}) + \sigma_n^2\boldsymbol{I}_N\right)\mathbf{v}\right]\boldsymbol{\Lambda}^H - 2\mathcal{R}\left[\boldsymbol{\Lambda}\mathbf{v}^H\boldsymbol{\phi}(\boldsymbol{b})\boldsymbol{U}\boldsymbol{D}^{1/2}\right]\right\} \quad (53)$$

The auxiliary vector $\boldsymbol{\Lambda}$ is computed given $\boldsymbol{b}$ and $\mathbf{v}$ as:

$$\boldsymbol{\Lambda}^*(\boldsymbol{b}, \mathbf{v}) = \mathrm{argmin}_{\boldsymbol{\Lambda}}\, \varepsilon_r(\boldsymbol{\Lambda}, \boldsymbol{b}, \mathbf{v}) = \frac{\boldsymbol{D}^{1/2}\boldsymbol{U}^H\boldsymbol{\phi}^H(\boldsymbol{b})\mathbf{v}}{\mathbf{v}^H\left(\boldsymbol{\phi}(\boldsymbol{b})\left(\boldsymbol{R}_{\boldsymbol{x}} + \sum_{i=2}^{N_u}\boldsymbol{R}_{\boldsymbol{w}_i}\right)\boldsymbol{\phi}^H(\boldsymbol{b}) + \sigma_n^2\boldsymbol{I}_N\right)\mathbf{v}} \quad (54)$$

Substituting (54) into (53) yields:

$$\varepsilon_r{}^*(\boldsymbol{b}, \mathbf{v}) = -\mathrm{tr}\left\{\boldsymbol{\Lambda}^*(\boldsymbol{b}, \mathbf{v})\mathbf{v}^H\boldsymbol{\phi}(\boldsymbol{b})\boldsymbol{U}\boldsymbol{D}^{\frac{1}{2}}\right\} \quad (55)$$

Denoting $\boldsymbol{s} = \boldsymbol{D}^{1/2}\boldsymbol{U}^H\boldsymbol{\phi}^H(\boldsymbol{b})\mathbf{v}$, from (54), (55) can be rewritten as:

$$\varepsilon_r{}^*(\boldsymbol{b}, \mathbf{v}) = -\frac{\boldsymbol{s}^H\boldsymbol{s}}{\mathbf{v}^H\left(\boldsymbol{\phi}(\boldsymbol{b})\left(\boldsymbol{R}_{\boldsymbol{x}} + \sum_{i=2}^{N_u}\boldsymbol{R}_{\boldsymbol{w}_i}\right)\boldsymbol{\phi}^H(\boldsymbol{b}) + \sigma_n^2\boldsymbol{I}_N\right)\mathbf{v}} = \frac{1}{2^{R_b(\boldsymbol{b},\mathbf{v})} - 1} \quad (56)$$

The problem

$$\boldsymbol{b}^* = \mathrm{argmax}_{\mathbf{b}}\, \frac{\mathbf{v}^H\boldsymbol{\phi}(\boldsymbol{b})\boldsymbol{R}_{\boldsymbol{x}}\boldsymbol{\phi}^H(\boldsymbol{b})}{\mathbf{v}^H\left(\boldsymbol{\phi}(\boldsymbol{b})\sum_{i=2}^{N_u}\boldsymbol{R}_{\boldsymbol{w}_i}\boldsymbol{\phi}^H(\boldsymbol{b}) + \sigma_n^2\boldsymbol{I}_N\right)\mathbf{v}} = 2^{R_b(\boldsymbol{b},\mathbf{v})} - 1 \quad (57)$$

Is then equivalent to:

$$\boldsymbol{b}^* = \mathrm{argmin}_{\boldsymbol{b}}\left[\min_{\boldsymbol{\Lambda}}\varepsilon_r(\boldsymbol{\Lambda}, \boldsymbol{b}, \mathbf{v})\right] \quad (58)$$

To solve problem (58), following the AO approach, the two minimization problems are computed separately. Specifically, we proceed as follows:

- With $\boldsymbol{b} = \boldsymbol{b}^{(k)}$ and $\mathbf{v} = \mathbf{v}^{(k)}$, we compute $\boldsymbol{\Lambda}^{(k+1)} = \boldsymbol{\Lambda}^*\left(\boldsymbol{b}^{(k)}, \mathbf{v}^{(k)}\right)$ (59)
- We evaluate $\boldsymbol{b}^{(k+1)} = \mathrm{argmin}_{\boldsymbol{b}}\, \varepsilon_r\left(\boldsymbol{\Lambda}^{(k+1)}, \boldsymbol{b}, \mathbf{v}^{(k)}\right)$ (60)
- We evaluate $\mathbf{v}^{(k+1)} = \mathrm{argmin}_{\mathbf{v}}\, \varepsilon_r\left(\boldsymbol{\Lambda}^{(k+1)}, \boldsymbol{b}^{(k+1)}, \mathbf{v}\right)$ (61)

The problem (61) is a convex problem and can be solved using standard convex optimization techniques. In contrast, the problem (60) is non-convex due to the nonlinearity of the RIS response reported in (47). This nonlinearity arises from the inverse of a matrix, so to solve the problem, we adopted the strategy of calculating the solution at step k+1 as a small variation from the solution at the previous step, allowing us to linearize the expression of the matrix inverse through the Neumann series approximation. Specifically, we calculate the solution for small variations in the phase φ_m of the reflection coefficient Γ_m of the m-th port of the RIS given by $\Gamma_m = e^{j\varphi_m}$, utilizing the relationship between the reflection coefficient and the load impedance of the port, namely $\Gamma_m = \frac{jb_m - Z_0}{b_m + Z_0}$.

3.5.4 Numerical results

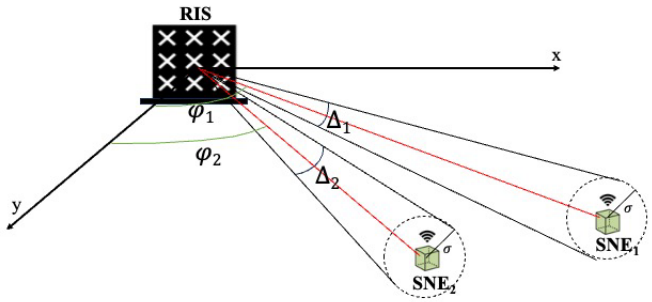

Figure 17. Model for correlation calculation based on the angular spread

Regarding the NLOS component, it is assumed to be Gaussian with covariance matrix dependent on the angular spread Δ_m as proposed in [25],[26], which is set to $\Delta_m = \pi/16$. The low value of the angular spread is justified by the fact that in short-range propagation conditions, the paths arriving from angles significantly greater than the main path are generally highly attenuated and do not contribute, consistent with the observation that the delay spread is also very low.

The results are shown in Figure 18-Figure 20, in which the average rate evaluated through several simulations is reported for N_u = 2. The intended SNE is positioned at $P_0 = (10\cos\pi/8, 10\sin\pi/8, 1)$ while the interfering SNE is positioned at 15 different possible positions $P_0 = (10\cos i\pi/32, 10\sin i\pi/32, 1)$ with i = 1,2,…,15. Accordingly, the interfering user is at the same distance from the RIS as the useful user (10 m) but with different angles. In Figure 18-Figure 20 (a), the case $d_x = \lambda/2$ is considered, whereas in Figure 18-Figure 20 (b) $d_x = \lambda/4$ is reported. Furthermore, the three figures refer to the values of σ = 0.1, 0.5, 1 m, respectively. The OPT-NoCSI curve refers to the proposed scheme in which the RIS is optimized without exact CSI, relying only on statistical information about the SNE positions. The OPT-CT case follows the same scenario, but here the RIS is optimized assuming the classical communication theory (CT) model, where the RIS acts as ideal scatterers, with each element functioning as a pure phase shifter (see [23] for a broader discussion of the different RIS models). Finally, the OPT-CSI cases assume exact CSI (ideal case).

It is noted that at position T_4, the interfering user is, on average, in the same position as the intended SNE; thus, an average rate of one is expected since the Signal-to-Interference Ratio (SIR) equals 1 and interference cannot be mitigated, as occurs in all considered cases. Additionally, at position T_8, the interfering user is at an angle $\pi/4$, corresponding to the specular position of the RIS with respect to the HC. In this instance, it is evident that the CT model fails, as the RIS is optimized without accounting for the specular component, which produces strong interference and is effectively modelled in the multiport RIS model considered here (see [23] for a deeper insight into these aspects).

It is also observed that the OPT-NoCSI optimizer achieves performance that is reasonably close to the OPT-CSI case in many scenarios, particularly where the uncertainty in node position is small, e.g., 0.1 m and 0.5 m. However, when the uncertainty in node positions increases to 1 m, the gap between the two cases also increases, as expected. In any case, the performance of the OPT-NoCSI case is encouraging, considering the significant reduction in RIS configuration overhead.

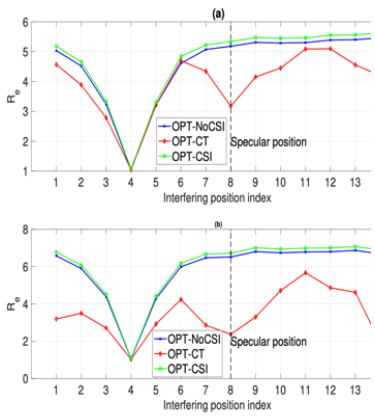

Figure 18. Results for σ = 0.1 m

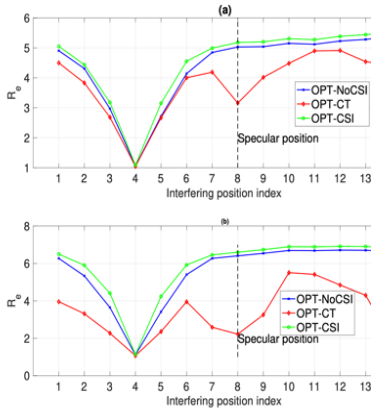

Figure 19. Results for σ = 0.5 m.

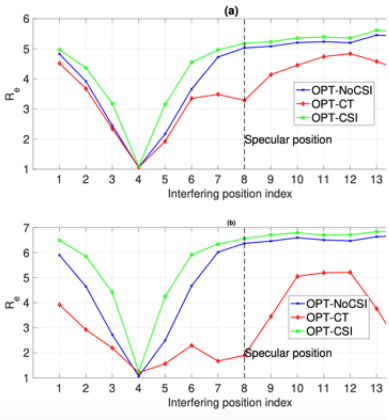

Figure 20. Results for σ = 1 m

3.5.5 Summary and Conclusions

The dynamic nature of the wireless channel and user mobility presents significant challenges when optimizing the RIS within a timescale aligned with the coherence time of the channel. This alignment would entail a prolonged time frame, which is incompatible with the latency constraints of many industrial applications. For instance, considering the industrial subnetwork use case "Subnetworks Swarms: Subnetwork Co-existence in Factory Hall," as described in deliverable D2.2 [2], it requires a maximum end-to-end latency of less than the transfer interval value of the applications.

Thus, the proposed study enables offline optimization of RIS, relying solely on statistical knowledge of the channel. This approach efficiently addresses the latency challenge, as the presence of RIS does not introduce any additional latency, thereby facilitating better performance in real-time industrial applications.

4 INTRA-SUBNETWORK RIS OPTIMIZATION STRATEGIES

In this section, scenarios involving one subnetwork with potential high number of subnetwork nodes, and in the presence of RIS nodes, are explored. The scenarios focus on the support that RIS can provide for the communication process in the subnetwork, both in terms of coverage extension by providing additional transmission links, and conversely, how the RIS can be used to serve multiple nodes at the same time. It will be shown how increased link availability with the RIS can help increasing KPIs such as reliability and latency, while addressing constraints such as operational modes, RIS control signalling, and transmit power.

4.1 RIS-aware Flexible Packet Coding (FPC) strategies

In this section, strategies for transmission of coded packets are devised, for subnetwork nodes transmitting within a subnetwork. It is considered that the transmitting subnetwork node has the ability to generate coded packets, and it has multiple transmission links available, including a RIS link. The considered problem and solution design relates to path selection for the subnetwork transmitter, considering the limitations and characteristics of the deployed RIS. Simulation results are obtained using 3GPP channel model parameter settings, comparing state of the art Low Density Parity Check (LDPC) from 5G-NR specifications, and the FPC techniques presented below. These yield a 10 times improvement in Block Error Rate (BLER) for fixed Signal to noise ratio (SNR) values, in line with verifiability objective 3, the design new physical layer (PHY) enablers for scalable requirements in terms of latency, reliability or throughput, tailored to devices with constrained computational capabilities by leveraging the opportunities offered by short range subnetworks.

4.1.1 Introduction to Flexible packet coding

Flexible packet coding (FPC) or network coding (NC) is a packet level processing function, or more specifically a packet coding function that transforms X input packets, also denoted as X source packets or X NC service data units (SDUs), into Y output packets, also denoted as Y NC protocol data units (PDUs). In general, X is greater than or equal to 2 and Y is greater than or equal to X, with the case X equal to 1 and Y equal to 1 being a special case [27]. The X input packets being coded together form a network coding (NC) generation, also denoted as a generation, and X denotes the generation size. An output packet of the network coding processing is denoted as NC PDU wherein each NC PDU is a linear combination of one or more of the X source packets (X NC SDUs), i.e. a first NC PDU is generated based on a linear combination of one or more of the X NC SDUs using a first set of network coding coefficients, and a second NC PDU is generated based on a second linear combination of one or more of the X NC SDUs using a second set of network coding coefficients that is independent from the first set of network coding coefficients, i.e., the first NC PDU and the second NC PDU are linearly independent.

In order to successfully recover the K NC SDUs at the receiver, the receiver needs to correctly decode at least X linearly independent NC PDUs out of the Y transmitted NC PDUs. Therefore, even if the receiver fails to correctly decode some of the received Y NC PDUs, the receiver can still recover the X NC SDUs. As mentioned earlier, network coding is used to describe packet coding techniques wherein coding may be a) end-to-end coding where coding is performed at the source (i.e. originating node of the packet), decoding is performed at the destination, and no recording at any intermediary node, or b) coding is performed at the source and/or intermediate forwarding node, and decoding is performed at the destination.

The PDUs associated with the same generation may be of same or different characteristics. Such characteristics may be systematic packets (source packets to be encoded), coded packets, less-innovative coded packets, more-innovative coded packets, etc. Furthermore, there may be dependencies between PDUs of the same generation in the sense that: a) the receiver needs to receive X PDUs or more to recover the X SDUs; b) how many more PDUs or specific PDUs are needed by the receiver to receive the X SDUs depends on the PDUs already available at the receiver; c) the scheduling of the PDUs of the same generation is constrained by the same overall delay budget.

4.1.2 Benefits of FPC

Network coding can provide flexible redundancy coding rate for reliability requirements and flexible split of transmission of coded packets over different radio links transmission paths within, or between subnetworks, (e.g. frequency diversity, spatial diversity, code diversity) or over different time instances (for time domain diversity).

Use of network coding may alleviate a scheduler (either at a 6G-BS, or at an HC node integrated to the parent 6G network) from having to select conservative MCS transmission parameters and/or improve the allocation of other transmission resources to improve overall communication performance.

Generally speaking, network coding also leads to better link efficiency, reduced latency, improved reliability, and reduced buffering requirements.

4.1.3 FPC Terminology

Innovative NC PDU: An innovative packet or innovative NC PDU is a coded packet that when received is useful for decoding the generation i.e. increases the rank of the generator matrix used to generate the NC PDUs.

Level of Innovativeness: Usefulness of the packet when decoding a generation of packets. Some packets will only enable the decoding of a small amount of source packets while others will enable the decoding of a large amount of source packets.

On-the-Fly Decoding: Some innovative NC PDUs will enable the recovery of at least one but not all NC SDUs that form a generation. In this case, the receiver can attempt to immediately recover some of the NC SDUs even though more NC PDUs will be needed to recover all the NC SDUs that form the generation. While multiple rounds of decoding require additional computation for the receiver, immediate recovery of some NC SDUs can reduce the delay in the reception of these packets.

Latency requirement or delay budget of NC PDU: A delay budget of an NC PDU associated with an NC generation can be defined as the delay budget of the one or more NC SDUs that form the NC generation. Similarly, a delay budget of an NC generation can be defined as the delay budget of the one or more NC SDUs that form the NC generation.

4.1.4 Path selection for subnetwork node transmission of NC PDUs

A subnetwork with multi-path availability is considered, where the subnetwork transmitter is able to generate coded packets, and has different links available. Figure 21 depicts this scenario, where the SNE is the entity generating coded packets, and transmitting them. For transmission, paths 1, 2 and 3 are available, that represent links with a RIS, an HC node, and an LC node, respectively.

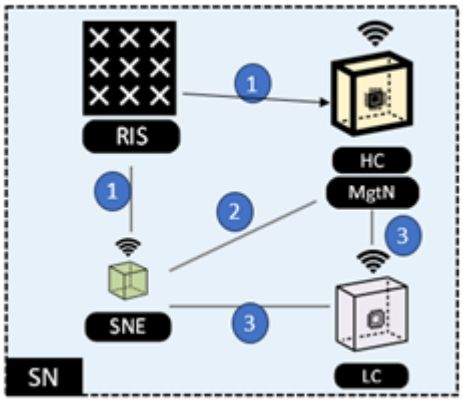

Figure 21. Intra sub-network paths between transmitter (SNE) and receiver (HC)

Different transmission paths may have different link quality, and hence different paths may provide different levels of quality of service (QoS), e.g. data rate, reliability, latency, to the PDUs. Transmission of PDUs on different paths may result in different level of resource (e.g. transmit power, time domain, frequency domain etc.) utilization. Transmissions to different paths assume beamforming, linking this work to the beam management work presented earlier in [28]. Therefore, the problem covered in this section is how to map NC PDUs with different characteristics to different transmission paths (i.e. indirect path via RIS, direct path, indirect path via an LC node) between SNE and HC whilst accounting for dependencies between NC PDUs generated using the same NC generation and improve efficiency of utilized resources.

4.1.4.1 Dependencies between NC PDUs

NC PDUs with different characteristics may contribute differently towards recovery of source NC SDUs at the receiver and as such they may have different importance which can be determined by the SNE as a function of the following examples:

- Remaining delay budget of NC PDU: An NC PDU is of high importance if the remaining delay budget of the NC PDU is below a threshold. Otherwise, NC PDU is of low importance.
- Innovativeness of NC PDU: An NC PDU generated using an NC generation is of high importance if it is an innovative NC PDU i.e. linearly independent from one or more NC PDUs, generated using the same NC generation, which the SNE may have already transmitted (e.g. transmitted in a transport block, or determined by SNE as successfully received at the receiver based on positive acknowledgement received by the SNE from the receiver (e.g. HC)), or selected for submission to HC. Otherwise, the NC PDU is of low importance.
- Type of NC PDU: An NC PDU is of high importance if it is a systematic NC PDU. Otherwise, the NC PDU is of low importance if the NC PDU is non-systematic NC PDU.
- Whether the NC PDU enables recovery of NC SDU(s) using on-the-fly-decoding: An NC PDU is of high importance if the receiver is performing on-the-fly decoding and upon reception of the NC PDU the receiver can use on-the-fly decoding to recover one or more NC SDUs. Otherwise, the NC PDU is of low importance. Moreover, an NC PDU that enables the recovery of more NC SDUs via on-the-fly decoding than another NC PDU is of higher importance.
- Importance of NC SDU(s): An NC PDU is of high importance if the importance of NC SDUs associated with the NC generation used to generate the NC PDU is high. Otherwise, the NC PDU is of low importance. If on-the-fly decoding is used at the HC node, a NC PDU that enables the recovery of more NC SDUs has an importance that is the average/mean of the SDUs that may be recovered via on-the-fly decoding.
- Number of NC PDUs required to recover NC SDUs associated with the NC generation used to generate the NC PDU: SNE may determine number of NC PDUs required to recover NC SDUs associated with an NC

generation based on e.g. radio conditions, NC configuration etc. as the absolute number of NC PDUs required to recover NC SDUs associated with the NC generation used to generate the NC PDUs. SNE can also determine number of NC PDUs required to recover NC SDUs associated with the NC generation based on feedback from the HC, number of NC PDUs already transmitted, and number of NC PDUs selected for transmission. Feedback from HC can indicate number of additional NC PDUs required for decoding the NC SDUs associated with the NC generation.

SNE can determine importance of an NC PDU based on any combination of the above.

4.1.5 Path selection for improved Quality-of-Service (QoS)

A suitable path for transmission of NC PDUs from SNE to HC node can be determined based on link quality of path between SNE and HC and NC PDU importance. PDU importance was addressed above, in this section, the focus is on link quality.

A suitable/preferred path to which the SNE may map an NC PDU can be determined based on suitability of the path to meet QoS requirements of an NC PDU, such as reliability and latency.

4.1.5.1 Path selection for increased reliability

SNE transmits an NC PDU with certain characteristics, e.g. systematic, more innovative, high importance etc., via a path that can support transmission with higher reliability as compared to other paths. SNE may also transmit NC PDUs with remaining delay budget below a threshold via a more reliable path to support transmission of NC PDUs within their delay budget requirement.

A path can be considered more reliable than other paths if the following conditions are satisfied:

- Link quality for the path is better than other paths
- A path is configured with lower layer configurations or radio resources which provide higher transmission reliability. This can include lower MCS values, larger number of repetitions etc. as compared to other paths.

4.1.5.2 Path selection for reduced latency

SNE transmits an NC PDU with certain characteristics, e.g. systematic, more innovative, high importance etc., or with certain requirements such as NC PDU with remaining delay budget below a threshold, via a suitable path that can support transmission with lower latency as compared to other paths.

A path would be more suitable than another path, to support latency requirement of NC PDUs e.g. based on their remaining delay budget, if any of the following conditions is satisfied:

- Link quality of the path is better than other path which may reduce need for retransmissions and hence reduce the latency.
- Buffer status of the entities associated with the path may result in transmission with lower latency than another path. For example, data volume (e.g., in bytes, bits, number of NC PDUs) in transmission buffer of entities associated with the path may be lower than the data volume in transmission buffer of entities associated with another path.
- Remaining delay budget of the NC PDUs in the transmission buffer(s) associated with the path, e.g., the average/minimum remaining delay budget of NC PDUs in the buffer associated with the path, is higher than the remaining delay budget of the NC PDU to be routed. Whereas remaining delay budget of the NC PDUs in the transmission buffer(s) associated with the other path is lower than the remaining delay budget of the NC PDU to be routed.

- The path is configured with characteristics which may reduce transmission latency e.g. lower maximum physical uplink shared channel (PUSCH) duration, multiple configured grant configurations with lower periodicity, different starting offsets to start a transmission etc. as compared to another path.

4.1.6 Link quality assessment

The link quality of a path between a transmitter node (i.e. SNE) and receiver node (i.e. HC) may be determined based on the following:

- RIS operational mode: For example, the link quality of indirect path via RIS may refer to the RIS operational mode and how the operation mode will impact transmission of a PDU from SNE to HC and the corresponding transmission requirement (such as transmit power) for SNE. The link quality cannot always be known to the SNE in the topology of Figure 21. This is because paths 1 and 3 are cascaded channels, and the SNE can only accurately measure its direct link for both these paths. Moreover, in the special case of path 1 with the RIS, the RIS limitations need to be factored in. These include the RIS operational mode, and how often the RIS channels are measured. Both play a major role in this scenario. The operational mode (see section 3.1) on the one hand can be tailored to serve other SNEs, LCs or HCs in the subnetwork, not visible in Figure 21, in terms of total coverage area, range, physical layer characteristics such as phase parameters, etc. This would have an impact on the NC PDU transmitting SNE, as the link quality for path 1 would be affected. For interference or any other subnetwork management reason, the RIS may also work in absorption mode, rendering it unavailable for transmission for the SNE.
- Radio measurements: Layer 1 or Layer 3 measurements of transmission(s) on a path between two nodes, which may include but are not limited to RSRP, RSRQ, SINR, RSSI, Pathloss, BLER, etc. In one approach, the L1 or L3 measurement may be performed at the evaluating node (e.g., evaluating SNE) for the path. In another approach, the L1 or L3 measurement for a path may be performed at the peer node (e.g., LC or RIS) and sent to the evaluating node (e.g., evaluating SNE). For example, the link quality of a path between two nodes may refer to the L3 RSRP of transmission from the peer node on the path. The measurements of the cascade channel can also happen at different rates. For example, the RIS may not have any mechanism for reporting link quality, or the measurements between RIS and HC may be made at different rates. This would create either blindness to the SNE on the link quality of path 1, or asynchronism between measurement reports for paths 1, 2 and 3.
- Distance between two nodes: For example, the link quality of a path between two nodes may be determined based on the distance between the two nodes on the path. For example, the SNE may determine the link quality between two nodes as good if the distance between two nodes is smaller than a threshold. Otherwise, the SNE may determine the link quality between two nodes as not good.
- Expected latency of a data unit traveling the path: For example, the lower the latency, the better the link quality.
- Difference between the expected latency of the path and the remaining delay budget of the data unit for which a routing decision is being made.

4.1.7 Numerical results

To validate the benefits of FPC methods, simulation work was conducted, and results are presented below. The chosen channel is conformant with the 3GPP channel model and is a Rayleigh fading channel causing bursty errors in the received packets. To simulate Joint Channel and Packet Coding (JCPC), FPC as explained above is performed as outer coding to channel coding in the physical layer, i.e., the output of FPC is fed into LDPC. These results were obtained using simulation settings as shown in Table 1 Simulation parameters.

Table 1 Simulation parameters

Parameter	Value
Code Rate	LDPC: 1/3 FPC: 1/3 JCPC: (1/2)x(2/3) (i.e. LDPC:1/2, FPC:2/3)
Modulation Scheme	16-QAM
Transport Block Size	45,096 bits
Transmission scheme	Single Input Single Output (SISO)
Channel Model	TDL-C [28]
Doppler shift	83.5 Hz
Number of HARQ retransmissions	0

Usefulness of packet erasure recovery capability of PC can be observed from Figure 22 which shows BLER performance of LDPC, FPC and JCPC measured against different values of SNR. It can be seen from simulation results that at high SNR, where performance is limited by packet erasures due to bursty errors, the use of JCPC, i.e., FPC+LDPC shows x10 improvement in BLER as compared to LDPC alone. FPC alone shows approx. x5 improvement as compared to LDPC alone.

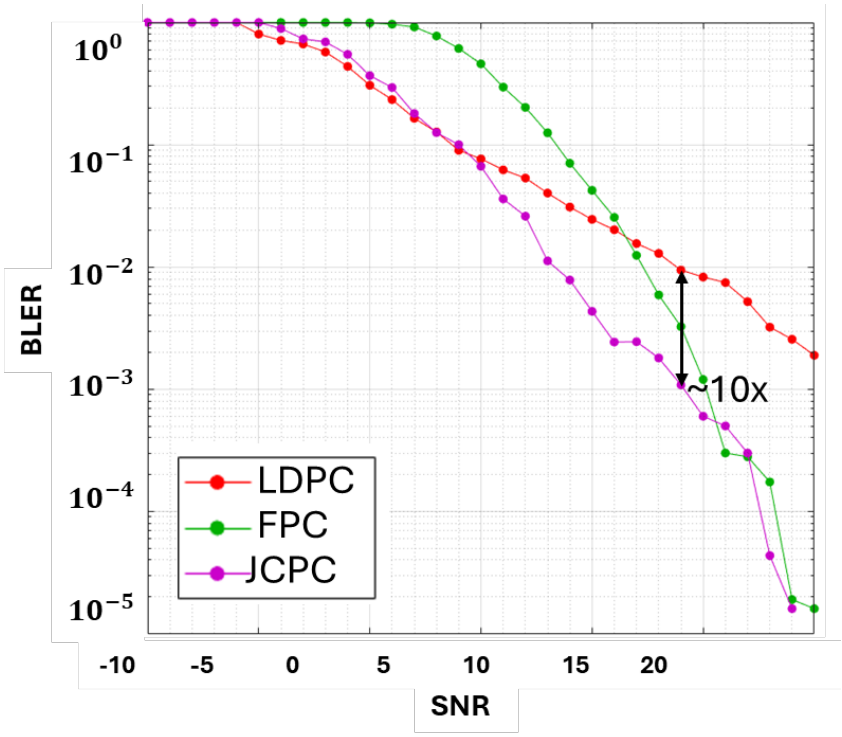

Figure 22. BLER comparison of 5G NR LDPC, FPC and JCPC for different SNR values

For the same channel coding rate, JCPC performs equally or better than LDPC-only due to the added benefit of packet erasure recovery capability of FPC. Therefore, high reliability gain of FPC based error control scheme makes it an attractive solution to be considered in 6G, wherein this gain can be converted into low latency for the same throughput or higher throughput for similar latency requirement as compared to non-FPC based techniques like LDPC.

4.1.8 Conclusion

FPC provides higher reliability benefits to communication links. This is especially important in the context of subnetworks, where many of the use cases consider large volumes of data transmitted and high reliability requirements for data delivery. FPC techniques presented in this section can be applied to any radio layer, providing additional flexibility in deployment. Results obtained consider physical layer forward error correction techniques, that can achieve a lower BLER by a factor of 10 (see Figure 22), for the same SNR value. Current cellular systems do not yet operate with FPC strategies and procedures, and their deployment in subnetwork topologies, where transmitting nodes must, in many instances, transmit high volumes of data, can be vital for their adoption in future cellular system releases.

4.2 Power Minimization with Rate Constraints for Multiple RISs with Multiple Nodes in Industrial Environment

4.2.1 Introduction

A relevant aspect that must be considered in all works dealing with RISs, is the computational complexity. The algorithmic complexity in this field is primarily rooted in two aspects: the *non convexity*, inherently related to the presence of RISs, and the *high dimensionality* of the considered optimization problems.

As for the latter aspect, large-size RISs are usually required in practical network deployments, in order to attain the necessary beamforming gain for coverage enhancement [27],[31]. Large-size RISs are inherently constituted by a large number of reconfigurable scattering elements, also referred as unit cells, each of which being an optimization variable. Therefore, the number of variables in the RIS optimization problem tends to be very large, and the computational complexity increases accordingly. For instance, in existing works, the iterative algorithms employed for optimization exhibit a complexity that scales at least with the cube of the total number of RIS elements.

To reduce the number of possible states, predefined configurations, or codebooks, have been introduced. These methods quantize the possible angles of arrival and departure into discrete sets, as elaborated in [32] for beam sweeping and channel estimation, and in [33] to reduce the optimization complexity under ideal channel estimation assumption. However, this approach reduces the design flexibility and is less effective in multipath environments with multiple nodes.

To overcome this limitation, [34] suggests dividing the RIS into independently optimized tiles using an Alternating Optimization (AO) method. While this allows for a greater design flexibility, it also introduces high complexity, as no predefined configurations are used.

In this work, we build upon the concept of tiles proposed in [34]. To reduce the complexity, we adopt the idea of defining a set of possible base configurations for each tile in order to recast the problem of optimizing a single RIS element into a problem of tile design. To limit the loss in terms of design flexibility and to minimize the dimensionality of the optimization problem, instead of using fixed codebooks as in [32],[33], the base functions are designed to maximize the power of the signal reflected from the tile towards each potential user, assuming perfect channel knowledge. The problem of CSI estimation is considered in a different part of the activity withing the project (see Section 3.5 of this deliverable).

The proposed approach achieves performance comparable to available benchmark schemes that offer the highest flexibility by treating each RIS element as an independent variable, while significantly reducing the dimensionality of the problem.

4.2.2 Scenario and target KPIs

The proposed work aims to cover a small area inhabited by many nodes with a controller device equipped with beamforming capabilities thanks to the presence of multiple antennas. Coverage must be ensured with a minimum transmission rate for each node while keeping the transmitted power at the lowest possible value. To achieve this, it is considered that RIS may be deployed in the environment. This scenario is very general and can be adapted to many scenarios in the 6G-SHINE project, and beyond. As a reference, we considered the industrial subnetwork use case 'Subnetworks Swarms: Subnetwork Co-existence in Factory Hall' described in deliverable D2.2 [2]. Indeed, it requires the connection of many nodes (up to a maximum of 20 units), which we call SNEs, with a control entity deployed within the confines of an edge infrastructure. We analyse the connection between the HC and the SNEs, necessary to dispatch control information. To this aim, the HC should perform advanced management strategies possibly aided by a MIMO transmission system to serve all nodes simultaneously while minimizing latency and interference. Specifically, since the considered subnetwork must interoperate with other similar sub-networks, minimizing power is an important target. Additionally, the HC-SNEs connection must guarantee a minimum data rate of 10 Mbps. Therefore, the two KPIs considered in our case will be a number of SNEs equal to 20 and a minimum data rate of 10 Mbps. Considering the critical role HC plays, it might be worthwhile to have a backup or redundancy mechanism for providing the required performance. Hence, we consider the presence of multiple appropriately optimized RIS which are placed higher than all nodes and obstacles, ensuring a strong Line-of-Sight

(LOS) propagation condition between the nodes (both HC and SNEs) and the RISs. This is the typical situation in which RISs are beneficial for meeting the required KPIs.
Therefore, we address a power minimization problem subject to rate constraints in the downlink, that is, in the connection between HC and SNEs. The considered scenario is illustrated in Figure 23.

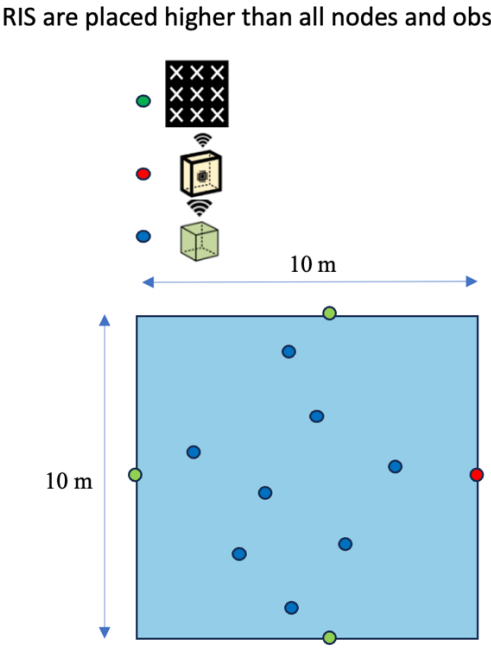

Figure 23. The considered scenario

4.2.3 System model and problem formulation

To remain general, we consider the downlink of a multi-user MIMO system aided by multiple RISs, where one HC equipped with *M* antennas serves N_u single-antenna SNEs, as depicted in Figure 23. The total number of RISs is *Q* and each RIS consists of *C* non overlapping tiles, so that the total number of tiles is $K = Q\,C$. Moreover, each tile is composed by *P* scattering elements. To cope with the concurrent transmissions of several users, the HC employs spatial precoding to enhance the transmission efficiency and to mitigate inter-user interference. The information symbol for the *j* SNE, denoted by $\theta_j \in \mathbb{C}$, is modelled as a zero-mean random variable with unitary mean square value. Different symbols are considered independent and identically distributed (i.i.d.). The *j*-th transmitted data stream $\boldsymbol{x}_j \in \mathbb{C}^M$ is obtained by multiplying the information data by the corresponding precoding vector $\boldsymbol{v}_j \in \mathbb{C}^M$, i.e.,

$$\boldsymbol{x}_j = \boldsymbol{v}_j \theta_j \tag{62}$$

At each of the N_u receivers, the signal is the superimposition of the signals reflected by all the RISs in the system. Accordingly, the signal $z_{i,k,j} \in \mathbb{C}$, received at the *i*-th SNE, reflected by the *k*-th tile, and relative to the *j*-th transmitted stream can be expressed as:

$$z_{i,k,j} = \boldsymbol{t}_{i,k} \boldsymbol{B}_k \boldsymbol{S}_k \boldsymbol{x}_j \tag{63}$$

where $\boldsymbol{t}_{i,k} \in \mathbb{C}^{1xP}$ is the channel vector between the *k*-th tile and the *i*-th receiver, $\boldsymbol{B}_k \in \mathbb{C}^{PxP}$ is a diagonal matrix whose elements are $b_{k,p}$, which models the scattering coefficient of the *p*-th scattering element ($p = 1,\ldots,P$) of the *k*-th tile, and $\boldsymbol{S}_k \in \mathbb{C}^{PxM}$ is the channel matrix between the BS and the *k*-th tile. In modeling the response of the RIS, it is important to consider the element gain, which depends on the area of each individual RIS element and the angles of the incident and reflected waves (see, for example, Deliverable D2.3. This term is incorporated into

the channel gains $\boldsymbol{t}_{i,k}$ and $\boldsymbol{S}_k$, meaning that B includes only the component related to the phase shift introduced by each element. In this regard, we put forth the idea that the vector $\boldsymbol{b}_k = diag(\boldsymbol{B}_k)$ can be represented as a linear combination of an appropriate set of basis vectors. Note that model (63) is based on the assumption of narrowband transmissions, meaning that the coherence bandwidth of the channel is greater than the bandwidth of the signal. This assumption is justified by the fact that, as shown in studies conducted within WP2 of the 6G-SHINE project and described in the Deliverable D2.3 in short-range indoor factory scenarios to which we refer, the delay spread stabilizes at values of a few tens of nanoseconds. Therefore, the coherence bandwidth is on the order of 50-100 MHz, a value that can be considered sufficiently large to assume narrowband transmissions.
By selecting an optimal basis vector, the design of the system can be significantly simplified. Specifically, we assume that $\boldsymbol{b}_k$ can be decomposed using N_u basis vectors, $\boldsymbol{b}_k{}^{(m)} \in \mathbb{C}^{Px1}$, with *m = 1,…, N_u* and the number of basis vectors is set equal to the number of users, i.e.,

$$\boldsymbol{b}_k = \sum_{m=1}^{N_u} \alpha_{m,k}\, \boldsymbol{b}_k{}^{(m)} \tag{64}$$

Assuming that each RIS is a passive device, the amplitude of the reflection coefficient $b_{k,p}$ (*p =1,…,P, k = 1,…,K*) of each unit cell scatters an amount of power that is at most equal to the impinging power, i.e.,

$$\left|b_{k,p}\right|^2 = \left|\sum_{m=1}^{N_u} \alpha_{m,k}\, b_{k,p}{}^{(m)}\right|^2 \leq 1, \tag{65}$$

where the equality holds in absence of losses. This latter case corresponds to consider that each element of the RIS introduces a simple phase shift, i.e., $b_{k,p} = e^{j\phi_{k,p}}$. The constraint in (65) is referred to as global constraint (GC) while $b_{k,p} = e^{j\phi_{k,p}}$ is referred to as local constraint (LC).
Introducing:

$$\widetilde{\boldsymbol{h}}_{i,m,k} = \boldsymbol{t}_{i,k}\boldsymbol{B}_k{}^{(m)}\boldsymbol{S}_k \tag{66}$$

we have from (63)

$$z_{i,k,j} = \sum_{m=1}^{N_u} \alpha_{m,k}\widetilde{\boldsymbol{h}}_{i,m,k}\, \boldsymbol{x}_j \tag{67}$$

Considering also the direct channel $\overline{\boldsymbol{h}}_{\boldsymbol{i}}$ the overall received signal relative to the j-th stream can be formulated as

$$y_{i,j} = \left(\overline{\boldsymbol{h}}_{\boldsymbol{i}} + \sum_{\boldsymbol{k=1}}^{\boldsymbol{K}} \sum_{m=1}^{N_u} \alpha_{m,k}\widetilde{\boldsymbol{h}}_{i,m,k}\right)\boldsymbol{x}_j \tag{68}$$

Let $\widetilde{\boldsymbol{H}}_i \in \mathbb{C}^{N_u K x M}$ the matrix obtained by stacking the channels $\widetilde{\boldsymbol{h}}_{i,m,k}$ (m=1,…,N_u and k = 1,…,K) so that the r-th row of the matrix is r = (k-1)N_u+m. Denoting with $\boldsymbol{\alpha} = \alpha_{1,1}, \dots, \alpha_{N_u,K}$ the row vector obtained by collecting all the coefficients $\alpha_{m,k}$ retaining the same ordering w.r.t. k and m, we can write $y_{i,j} = \boldsymbol{h}_i(\boldsymbol{\alpha})\boldsymbol{x}_j$ where $\boldsymbol{h}_i(\boldsymbol{\alpha}) = \overline{\boldsymbol{h}}_{\boldsymbol{i}} + \boldsymbol{\alpha}\widetilde{\boldsymbol{H}}_i$. Then, the signal received at the i-th SNE is:

$$y_i = \boldsymbol{h}_i(\boldsymbol{\alpha})\boldsymbol{x}_i + \boldsymbol{h}_i(\boldsymbol{\alpha})\sum_{j\neq i} \boldsymbol{x}_j + n_i \tag{69}$$

The corresponding SINR can be written as:

$$SINR_i(\boldsymbol{\alpha}, \mathbf{V}) = \frac{|\boldsymbol{h}_i(\boldsymbol{\alpha})\mathbf{v}_i|^2}{\sum_{j\neq i}\left|\boldsymbol{h}_i(\boldsymbol{\alpha})\mathbf{v}_j\right|^2 + \sigma_i^2} \tag{70}$$

where $\mathbf{V} = [\mathbf{v}_1, \dots, \mathbf{v}_{N_u}]$ is the total precoding matrix. Finally, the achievable rate can be written as:

$$R_i(\boldsymbol{\alpha}, \mathbf{V}) = \log_2\left(1 + SINR_i(\boldsymbol{\alpha}, \mathbf{V})\right) \tag{71}$$

For optimization purposes, it is now convenient to introduce the MSE defined as:

$$E_i(g_i;\boldsymbol{\alpha},\mathbf{V}) = 1 + |g_i|^2\left(\sum_{j=1}^{N_u}\left|\boldsymbol{h}_i(\boldsymbol{\alpha})\mathbf{v}_j\right|^2 + \sigma_i^2\right) - 2\Re(g_i^H\boldsymbol{h}_i(\boldsymbol{\alpha})\mathbf{v}_i) \tag{72}$$

which is minimized when the auxiliary variable g_i is:

$$g_i{}^*(\boldsymbol{\alpha},\mathbf{V}) = \frac{|\boldsymbol{h}_i(\boldsymbol{\alpha})\mathbf{v}_i|^2}{\sum_{j=1}^{N_u}\left|\boldsymbol{h}_i(\boldsymbol{\alpha})\mathbf{v}_j\right|^2 + \sigma_i^2} \tag{73}$$

so that, replacing (73) into (72) yields the equivalence between MMSE and SINR:

$$E_i{}^*(\boldsymbol{\alpha},\mathbf{V}) = E_i(g_i{}^*;\boldsymbol{\alpha},\mathbf{V}) = (1 + SINR_i(\boldsymbol{\alpha},\mathbf{V}))^{-1} \tag{74}$$

4.2.3.1 Basis Vector Design

The basis vectors, which represent an adaptive codebook in this scenario, are designed such that $\boldsymbol{b}_k{}^{(m)}$ is the configuration of tile k that maximizes the amount of reflected power towards node *m* when the signal is transmitted by the BS and there is no direct path. This problem is extensively studied in the literature and many approaches have been proposed [34]. In our case, the solution is based on the assumption that the channel between the BS and the RIS is characterized by a strong LOS component. This assumption is reasonable since the locations of the BS and the RIS are typically fixed and known, and they can be positioned appropriately to ensure a LOS connection that predominates over the multipath. In this setting, it is well known that an RIS configuration design that is reasonably close to optimal consists of directing the scattered signal toward the centre of the BS antenna system, both in the near-field and far-field regimes [35]. This design is also independent of the precoding vector utilized at the BS. To elaborate, let $\mathbf{k}_k \in \mathbb{C}^{Px1}$ be the vector encompassing the LOS component of the link connecting the k -th tile of the RIS to the centre of the BS antenna.
The basic functions are then chosen by solving N_u sub-problems:

$$\boldsymbol{b}_k{}^{(m)} = \text{argmax}_{\mathbf{b}}\left|\boldsymbol{t}_{m,k}\,diag(\boldsymbol{b})\mathbf{k}_k\right|^2 \tag{75}$$

for m = 1,…,N_u. Considering the constraint $\left|b_{k,p}^{(m)}\right| = 1$ the solution of (75) is:

$$b_{k,p} = e^{-j\angle t_{m,k}(p)}e^{-j\angle k_{m,p}} \tag{76}$$

Note that the phase shifts $\angle k_{m,p}$ for p = 1,…,P, are known and, as mentioned, correspond to the physical operation of focusing the signal emitted by the k-th tile of the RIS towards the centre of the BS, and $\angle t_{m,k}(p)$ denotes the phase shifts introduced by the link between the k-th tile and the m-th SNE.

4.2.3.2 Problem formulation

Since the KPI considered in this activity is the minimum bit rate for each connection, we address a power minimization problem subject to rate constraints. Specifically, we consider the following problem:

$$\begin{aligned}(\mathbf{V},\boldsymbol{\alpha}) = \ &\text{argmix}_{\mathbf{V},\boldsymbol{\alpha}}\sum_{i=1}^{N_u}\|\mathbf{v}_i\|^2 \\ \text{s.t. } &SNR_i(\mathbf{V},\boldsymbol{\alpha}) \geq \Sigma_i \quad 1 \leq i \leq N_u \\ &\left|\sum_{m=1}^{N_u}\alpha_{m,k}\,b_{k,p}{}^{(m)}\right|^2 = 1\end{aligned} \tag{77}$$

where Σ_i is the target SINR corresponding to the target rate R^i for the i-th SNE and the third constraint assumes no power losses in the RIS. Problem (77) is non-convex and, therefore, challenging to solve. To this aim, we

decompose it into two sub-problems, both formulated with the goal of minimizing the expended power: *precoding optimization* and *tile configuration optimization*.

Given that both optimization problems are oriented towards achieving the same objective, we can develop an iterative approach rooted in the AO framework, which allows for the sequential refinement of solutions by optimizing one variable set at a time while holding the others fixed, thereby progressively converging towards a (local) optimal solution. Within this framework, iteration t is composed by the sequential optimization of the precoding matrix and tile coefficients, which are denoted as $\mathbf{V}^{(t)} = \left[\mathbf{v}_1^{(t)}, \dots, \mathbf{v}_{N_u}^{(t)}\right]$ and $\boldsymbol{\alpha}^{(t)} = \left[\alpha_{11}^{(t)}, \dots, \alpha_{N_u,K}^{(t)}\right]$, respectively. Specifically, the precoding optimization sub-problem (PO) is:

$$\mathbf{V}^{(t)} = \operatorname{argmix}_{\mathbf{V}} \sum_{i=1}^{N_u} \|\mathbf{v}_i\|^2$$

$$\text{s.t. } SNR_i\left(\mathbf{V}, \boldsymbol{\alpha}^{(t)}\right) \geq \Sigma_i \qquad 1 \leq i \leq N_u \tag{78}$$

In this formulation, PO can be viewed as an instance of a second order cone programming (SOCP) problem and, as such, is convex and its solution can be found by employing standard solvers. As for the RIS configuration optimization, we translate the SINR constraint into an MMSE constraint by exploiting (74) and formulate the optimization problem as the minimization of the sum of MMSE subject to SINR (MMSE) constraints:

$$\boldsymbol{\alpha}^{(t+1)} = \operatorname{argmix}_{\boldsymbol{\alpha}} \sum_{i=1}^{N_u} E_i\left(g_i; \boldsymbol{\alpha}, \mathbf{V}^{(t)}\right)$$

$$\text{s.t. } E_i\left(g_i; \boldsymbol{\alpha}, \mathbf{V}^{(t)}\right) \leq E_i^*(\boldsymbol{\alpha}, \mathbf{V}) \qquad 1 \leq i \leq N_u \tag{79}$$

$$\left| \sum_{m=1}^{N_u} \alpha_{m,k}\, b_{k,p}{}^{(m)} \right|^2 = 1$$

The third constraint still makes the problems non-convex. Hence, we instead consider the convex and less stringent GC in (65), and then obtain a feasible solution that satisfies the LC by projecting the solution onto the unit circle.

4.2.4 Numerical results

In this work, it is assumed that the CSI is known, both for the definition of the bases (or codebooks) discussed earlier and for the solution to the optimal problem (79). On the other hand, the issue of CSI acquisition could be addressed as discussed in the section dedicated to this topic in this deliverable, namely by leveraging knowledge of the positions and considering average rates instead of instantaneous rates. Hence, we consider an HC equipped with M=8 antennas arranged in two linear arrays, each comprising 4 antennas. The antenna elements of the HC and the unit cells of the RIS are spaced by λ/2.

The bandwidth of the considered signal is 10 MHz and it is centred at f_c = 28 GHz (FR2), with a background interference (due to the presence of other systems transmitting in the same band and/or other subnetworks in proximity), including thermal noise, equal to 1pW. Consistent with the KPIs of the considered use case, a rate of at least 10 Mbps has been set for each SNE, which in our case means ensuring a threshold SINR of 3 dB (considering a realistic margin of 3 dB relative to the theoretical Shannon limit). The antenna gains in transmission and reception are 3 dB and the noise figure at the receivers is 8 dB. The results are obtained by averaging several instances for the spatial distribution of 20 single-antenna SNEs, which are placed at a height of 1 m, and are randomly deployed in a rectangular region of size [0,10] x [0, 10] m. Therefore, the results are obtained considering 100 different instances for SNEs positions. The HC is positioned at (10, 5, 2), and 3 RISs are considered, each composed of 800 scattering elements, 40 in the horizontal direction and 20 in the vertical direction. The RIS are positioned on three sides of the considered area, excluding the one where the HC is located, as shown in Fig. 1. Each RIS is composed of C = 4 tiles with dimension 20 x 10 each. As for the channel models, the direct HC-SNEs links are modelled based on the measurements reported in the deliverable D2.3 [3] particularly considering the short-range indoor factory scenario for the NLOS FR2 case.

Such measurements show that the path-loss is comparable, though improved, to that proposed by the 3GPP Indoor Factory NLOS model with Sparse Clutter (3GPP Inf-SL) and it is much lower than that predicted by the 3GPP Indoor Factory NLOS model with Dense clutter (3GPP Inf-DL). Therefore, to remain as general as possible, we decided to use the D2.3 model for P1% of the nodes, assumed to be in advantageous propagation conditions, while P2% are assumed to be subject to the 3GPP Inf-SL NLOS model and P3% to the 3GPP Inf-DL NLOS model. Three different values of P1, P2, and P3 are considered in the simulations, namely P1 = 100% in the Channel #1 case, P2 = 100% in the Channel #2 case and P1 = 95% and P3 = 0.05% in the Channel #3 case.

In the HC-RIS and SNE-RIS connections, one of the two nodes involved in the communication, namely the RIS, is typically positioned at a height greater than the others, as in our case where the RIS is placed at a height of 3 meters. This kind of situation is not reported in the study in D2.3, so it is assumed that these connections are generally modelled as a combination of a LOS Ricean component and a NLOS Rayleigh multipath component. The Ricean factors for the BS-RIS and RIS-UE links are set to 20 and 10, respectively. Finally, for both links, the average path loss is computed according to the free space attenuation model, which is 5-10 dB better than the model derived from the measurements reported in D2.3.

Figure 24 shows the cumulative distribution function (CDF) of the average power required to achieve the minimum rate for each node. The average power is obtained by averaging over several instances generated for each case. For comparison, we also present the performance achieved when the RIS are not present (without RIS), i.e., where communication occurs only through the SNE-HC channel. It is shown that the presence of RIS allows for a significant improvement in performance, particularly when there is even a minimal chance that the direct path is highly attenuated, as in the case of channel #3. The results demonstrate that the power in the D2.3 case is lower than in the 3GPP case, consistent with the fact that the 3GPP model exhibits greater attenuation. Furthermore, the presence of RIS allows for a significant improvement in performance (lower power for the same rate) in all cases; however, when considering the 3GPP model, this improvement is even more evident, particularly in the channel #3 case. Indeed, in this case, the direct HC-SNE paths are subject to greater attenuation, making the presence of RIS even more critical.

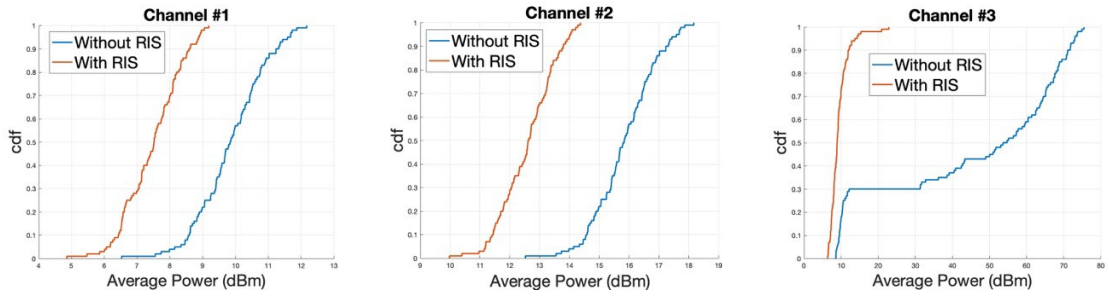

Figure 24 Performance obtained for the three different channels

4.2.5 Summary and conclusion

In this work, we aimed to provide a solution for the optimization of multiple RIS to minimize power consumption while ensuring a minimum transmission rate for each node. Specifically, we referenced the industrial subnetwork use case "Subnetworks Swarms: Subnetwork Co-existence in Factory Hall" described in deliverable D2.2 [2]. This case requires connecting to 20 robot nodes, referred to as Sub-Network Entities (SNEs), with a control entity deployed within edge infrastructure confines. The analysis focuses on the connection between the HC controller and the SNEs to dispatch control information, utilizing a MIMO transmission system to serve all nodes simultaneously while minimizing latency and interference. Given that the subnetwork must interoperate with other similar networks, minimizing power is a critical target. In our study, we consider as KPIs: the number of SNEs, set at 20, and a minimum data rate of 10 Mbps. Therefore, we considered deploying multiple appropriately optimized RIS positioned above all nodes and obstacles, facilitating a strong Line-of-Sight (LOS) propagation

condition between the HC and SNEs and the RISs. This approach effectively addresses the outlined KPIs, demonstrating the benefits of RIS in achieving the desired communication performance in the specified scenario.

5 INTER-SUBNETWORKS RIS OPTIMIZATION STRATEGIES

In this section, scenarios involving one or more subnetworks in the presence of a RIS are explored. The subnetworks operate under the coverage of a 6G-BS cell coverage, where RIS HW is deployed. The presence of the RIS has profound impacts on the channels within the subnetwork, and from the coverage of a 6G-BS to the subnetworks. The RIS may provide coverage from the 6G-BS to the subnetworks which is a benefit, and thus, can be used for cooperative subnetwork scenarios. However, it can also reflect signals from the 6G parent network into areas of the subnetwork where nodes operate and transmit, which may result in undesirable interference in the subnetwork, undermining its performance. An example cooperation is related to encoding and reencoding of packets along its multiple hops towards a central processing server. The dual aspect of the benefits and impairments that the presence of RIS can bring to cooperative subnetwork scenarios, as well as path selection considering recoding operations are addressed in this section.

5.1 Uncoordinated subnetworks

In this work we consider a RIS-aided SN operating within a macrocell. In the SN there are two types of SNEs, those that require RIS-assistance, and those that do not. While there may be an arbitrary number of SNEs within each type, it suffices for our purposes to assume a single SNE of each type. Thus, we consider SNE_1 to be RIS-aided, while SNE_2 is not. However, as we will demonstrate, the presence of the RIS may cause interference for SNE_2 due to undesired reflections from the macrocell. In this work we attempt to mitigate said interference by means of non-diagonal RISs. In Figure 25 the system model is shown.

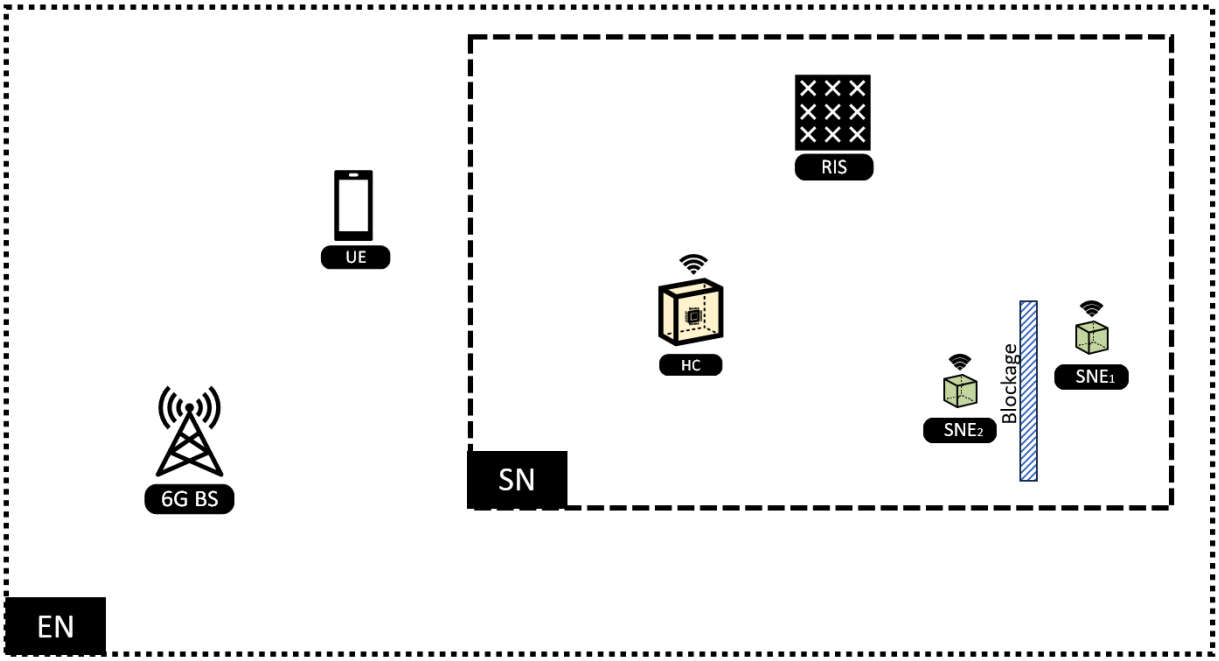

Figure 25. An SN within a macrocell. SNE_1 requires RIS-assistance while SNE_2 can communicate directly with the HC.

Before proceeding further, we lay down the mechanisms that induce interference on SNE_2. As was discussed and elaborated upon in Deliverable D3.2 [1], a standard RIS does not only reflect signals in its configured directions, but in fact from all possible directions. Consider now a RIS configuration enabling the HC to establish connection to SNE_1, this is shown with red arrows in Figure 26. A "RIS configuration" is, essentially, a set of phase shifts that produces an anomalous reflection according to an angle φ; this angle is more strictly a pair of azimuth and elevation angles, but for simplicity we refer to it as only angle. However, the 6G BS is simultaneously serving its connected UE (heavy blue arrow), but a part of this signal may reach the RIS (leftmost thin blue line). Due to the RIS configuration, this latter signal will be reflected by the RIS with reflection angle φ (rightmost thin blue line). In

the worst case, this reflected signal may hit SNE_2, thereby causing potentially heavy interference. We remark that the interference (i.e., the blue arrow) will not interfere with SNE_1 unless the directions of the 6G BS and the HC coincide as seen from the RIS. As this can be avoided at installation of the SN, it is not our main concern. Instead, it is the SNEs not in the need of RIS-assistance that may be the victims of RIS-induced interference, i.e., SNE_2 in our case.

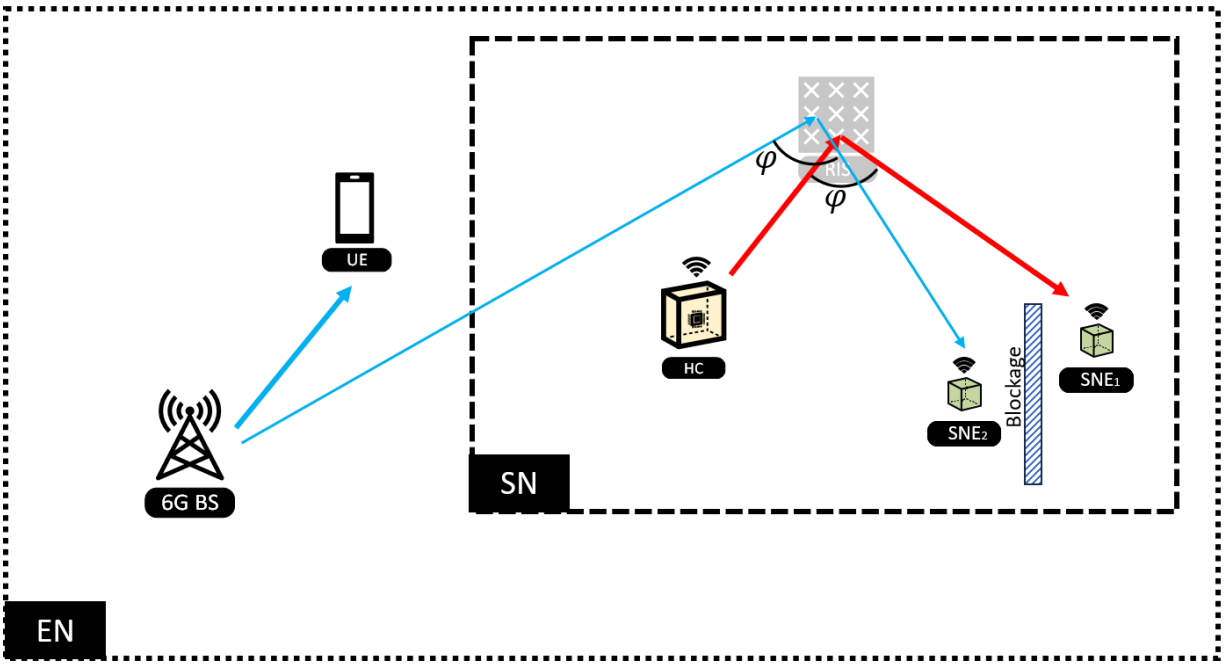

Figure 26. Annotated version of Figure 25. See text for details. The RIS has been made transparent for improved clarity.

Now, if SNE_2 is not served by the HC when the RIS has configuration φ it will not be interfered with by the RIS. Thus, we invoke (at least) one out of two assumptions:

1. The HC serves its SNEs using TDMA, and the RIS maintains its configuration while serving SNE_2.
2. The HC serves its SNEs using FDMA, and the RIS reflects across the entire bandwidth.

Assumption 1 is reasonable as it leads to much less re-configurations at the RIS, thereby saving power and overhead. Assumptions 2 is reasonable since when only SNE_1 is present, it may occupy the entire bandwidth, and then the RIS must be capable of serving the SNE across the entire band.

5.1.1 Interference mitigation through non-diagonal RISs

As was described in Section 3.3, a non-diagonal RIS does, in general, not reflect *any* incoming signal to a well-defined outgoing direction; this only happens for the configured directions. The impinging interference signal, i.e., the leftmost thin blue line in Figure 26, which is not a configured impinging direction will, by no means, be absorbed by a non-diagonal RIS, but rather scattered randomly. The important part here is that the impinging signal *will not be beamformed* by the RIS. In this work, we shall synthesize the permuted RIS architecture, as this is the one developed during the 6G-SHINE project. Hereafter, we shall refer to this architecture as "permuted RIS", or P-RIS for short.

A P-RIS has a reflection pattern that is dependent upon the particular permutation used. In formula, we may refer to the reflection pattern of a P-RIS as $A(\varphi_{\text{in}}, \varphi_{\text{out}}; \sigma, \boldsymbol{\phi})$ where $\varphi_{\text{in}}, \varphi_{\text{out}}$ are the impinging and outgoing directions

(azimuth and elevation), respectively, where σ is the particular permutation used, and ϕ is the phase shift values. It is convenient to not work with angles, but rather with directional cosines (DR) $\boldsymbol{k} = (k_{\mathrm{x}}, k_{\mathrm{y}})$. If we refer to the impinging DR on the RIS as $\boldsymbol{k}_{\mathrm{in}}$ and the outgoing direction $\boldsymbol{k}_{\mathrm{out}}$, then for any set of phase shift values ϕ and the identity permutation, it holds that

$$A(\boldsymbol{k}_{\mathrm{in}}, \boldsymbol{k}_{\mathrm{out}}; \sigma = \mathbb{I}, \boldsymbol{\phi}) = A_{\mathbb{I}}(\boldsymbol{k}_{\mathrm{out}} - \boldsymbol{k}_{\mathrm{in}}; \boldsymbol{\phi}) \tag{80}$$

for a function $A_{\mathbb{I}}(\cdot;\cdot)$ that is easily quantified. This is the mathematical basis for the interference problem illustrated in Figure 26. However, for a general permutation, it is no longer true that the reflection pattern only depends on the difference of DRs. If $\boldsymbol{k}_{\mathrm{HC}}$ and $\boldsymbol{k}_{\mathrm{BS}}$ denote the impinging DRs from the HC and the 6G BS, respectively, on the RIS, and $\boldsymbol{k}_1$ and $\boldsymbol{k}_2$ the outgoing DRs to SNE$_1$ and SNE$_2$, respectively, then it holds that

$$A(\boldsymbol{k}_{\mathrm{HC}}, \boldsymbol{k}_1; \sigma \neq \mathbb{I}, \boldsymbol{\phi}) \neq A(\boldsymbol{k}_{\mathrm{BS}}, \boldsymbol{k}_2; \sigma \neq \mathbb{I}, \boldsymbol{\phi}) \tag{81}$$

despite the fact that we may very well have $\boldsymbol{k}_1 - \boldsymbol{k}_{\mathrm{HC}} = \boldsymbol{k}_2 - \boldsymbol{k}_{\mathrm{BS}}$. In fact, if the phase shift vector is chosen so to maximize $A(\boldsymbol{k}_{\mathrm{HC}}, \boldsymbol{k}_1; \sigma \neq \mathbb{I}, \boldsymbol{\phi})$, i.e., we select it according to

$$\boldsymbol{\phi}^{\mathrm{opt}} = \arg\max_{\boldsymbol{\phi}} |A(\boldsymbol{k}_{\mathrm{HC}}, \boldsymbol{k}_1; \sigma \neq \mathbb{I}, \boldsymbol{\phi})|^2 \tag{82}$$

then it typically holds that $A(\boldsymbol{k}_{\mathrm{BS}}, \boldsymbol{k}_2; \sigma \neq \mathbb{I}, \boldsymbol{\phi}^{\mathrm{opt}}) \approx 0$. However, different permutations σ yield different degrees of interference suppression, i.e., magnitudes of $A(\boldsymbol{k}_{\mathrm{BS}}, \boldsymbol{k}_2; \sigma \neq \mathbb{I}, \boldsymbol{\phi}^{\mathrm{opt}})$. Thus, for each interference situation, one must search for/construct a permutation that eliminates as much as possible of the interference.

5.1.1.1 System model

We assume a narrowband model in which all SNEs have a single antenna, the 6G BS has N antennas, the HC has a single antenna, and the RIS is synthesized as an $M \times M$ uniform planar array. We let

- $\boldsymbol{h}_{\mathrm{HC}}$ denote the $M^2 \times 1$ channel vector from the HC to the RIS,
- $\boldsymbol{H}_{\mathrm{BS}}$ denote the $M^2 \times N$ channel matrix from the 6G BS to the RIS,
- $\boldsymbol{g}_1$ denote the $1 \times M^2$ channel vector from the RIS to SNE$_1$,
- $\boldsymbol{g}_2$ denote the $1 \times M^2$ channel vector from the RIS to SNE$_2$,
- f_2 denote the scalar direct channel between the HC and SNE$_2$; $f_1 = 0$ by assumption, but this is largely irrelevant for our purposes,
- $\boldsymbol{g}_{\mathrm{UE}}$ denote the $1 \times N$ channel vector from the 6G BS to the UE.

The received signal at SNE$_1$ reads (in the absence of noise)

$$y_1 = \boldsymbol{g}_1 \boldsymbol{\Theta} \boldsymbol{h}_{\mathrm{HC}} x \tag{83}$$

where x is the data symbol to be conveyed and $\boldsymbol{\Theta}$ the transfer function of the RIS. Said transfer function may be decomposed as $\boldsymbol{\Theta} = \boldsymbol{P}(\sigma)\mathrm{diag}(\exp(\jmath\boldsymbol{\phi}))$, where $\boldsymbol{P}(\sigma)$ is an $M^2 \times M^2$ permutation matrix representing the permutation σ. For a given maximization, the phase vector is selected so that the link gain is maximized, i.e.,

$$\boldsymbol{\phi}^{\mathrm{opt}} = \arg\max_{\boldsymbol{\phi}} |\boldsymbol{g}_1 \boldsymbol{\Theta} \boldsymbol{h}_{\mathrm{HC}}|^2 \tag{84}$$

This has the (trivial) solution

$$\phi_m^{\mathrm{opt}} = -\angle h_{\mathrm{HC},m} - \angle t_m \tag{85}$$

where $\boldsymbol{t} = \boldsymbol{g}_1 \boldsymbol{P}(\sigma)$. With that, we obtain a channel gain at SNE$_1$ equal to

$$\gamma_1 = |\boldsymbol{g}_1 \boldsymbol{P}(\sigma)\mathrm{diag}(\exp(\jmath\boldsymbol{\phi}^{\mathrm{opt}}))\, \boldsymbol{h}_{\mathrm{HC}}|^2 = \left(\sum_{m=1}^{M^2} |t_m h_{\mathrm{HC},m}| \right)^2 \tag{86}$$

At SNE_2, which is not RIS assisted, we obtain a channel gain (note that we have ignored any RIS-induced contributions) of $\gamma_2 = |f_2|^2$. As the UE has a single antenna, we assume an MRT transmission from the 6G BS to the UE, which implies that the transmitted signal, $\boldsymbol{s}$, from the 6G BS is described by

$$s = \frac{\boldsymbol{g}_{\mathrm{UE}}^{\mathrm{H}}}{\sqrt{\|\boldsymbol{g}_{\mathrm{UE}}\|^2}}\sqrt{P_{\mathrm{BS}}}z \tag{87}$$

where z is a data symbol, and P_{BS} the transmit power of the 6G BS.

With that, both SNEs are subject to interference from the 6G BS, and the interference channel gains are

$$I_k = \left|\boldsymbol{g}_k \boldsymbol{P}(\sigma)\mathrm{diag}(\exp(\jmath\boldsymbol{\phi}^{\mathrm{opt}}))\boldsymbol{H}_{\mathrm{BS}}\frac{\boldsymbol{g}_{\mathrm{UE}}^{\mathrm{H}}}{\sqrt{\|\boldsymbol{g}_{\mathrm{UE}}\|^2}}\sqrt{P_{\mathrm{BS}}}\right|^2, \qquad k = 1,2 \tag{88}$$

As already explained, as the impinging angles from the HC and the 6G BS on the RIS can be assumed different, we may assume $I_1 \approx 0$, whereas $I_2 \gg 0$ for some positions of the SNE_2. Thus, our main interest is to study the SIR at SNE_2 which reads

$$SIR_2(\sigma) = P_{\mathrm{HC}}\frac{\gamma_2}{I_2} = \frac{P_{\mathrm{HC}}|f_2|^2}{\left|\boldsymbol{g}_2\boldsymbol{P}(\sigma)\mathrm{diag}(\exp(\jmath\boldsymbol{\phi}^{\mathrm{opt}}))\boldsymbol{H}_{\mathrm{BS}}\frac{\boldsymbol{g}_{\mathrm{UE}}^{\mathrm{H}}}{\sqrt{\|\boldsymbol{g}_{\mathrm{UE}}\|^2}}\sqrt{P_{\mathrm{BS}}}\right|^2}, \tag{89}$$

where we explicitly expressed the dependency of the SIR on the RIS permutation and P_{HC} is the transmit power of the HC. For a RIS with tuneable permutations, it is our objective to seek the best permutation, i.e.,

$$\sigma^{\mathrm{opt}} = \arg\max_{\sigma} SIR_2(\sigma) = \arg\min_{\sigma}\left|\boldsymbol{g}_2\boldsymbol{P}(\sigma)\mathrm{diag}(\exp(\jmath\boldsymbol{\phi}^{\mathrm{opt}}))\boldsymbol{H}_{\mathrm{BS}}\frac{\boldsymbol{g}_{\mathrm{UE}}^{\mathrm{H}}}{\sqrt{\|\boldsymbol{g}_{\mathrm{UE}}\|^2}}\sqrt{P_{\mathrm{BS}}}\right|^2 \tag{90}$$

As this is a combinatorial optimization, there is no closed form solution. As a remedy, we adopt an alternate coordinate optimization approach summarized next.

- Initialize with an arbitrary permutation (some heuristic methods for this purpose are readily available, but not provided herein.
- For each index of the permutation $1 \le m \le M^2$:
  - For each index $1 \le m' \le M^2, m' \ne m$
    - Construct a permutation σ' by swapping elements $\sigma(m)$ and $\sigma(m')$
    - Compute $SIR_2(\sigma')$
    - Update σ as the σ' with the lowest $SIR_2(\sigma')$
- Repeat until no changes.

This algorithm has a complexity that is at least $\mathcal{O}(M^4)$, but in each iteration the complexity is very low, and, moreover, it converges rapidly. However, to execute the algorithm, we note that all channels must be known, including the effective channel from the 6G BS to the RIS (i.e., including the 6G BS precoding). This is challenging in practice, and future work should address this issue. A possible method would be to continuously alter the permutation over time until less interference at SNE_2 is observed. Another approach would be to develop a codebook of permutations, which are based upon the relative locations of the 6G BS and SNE_2 in relation to the RIS.

5.1.1.2 Numerical experiments

We next turn to numerical experiments. The geometry of our test is shown in Figure 27; the red area shows the possible locations of SNE_2 and a uniform distribution of SNE_2 inside said area is assumed.

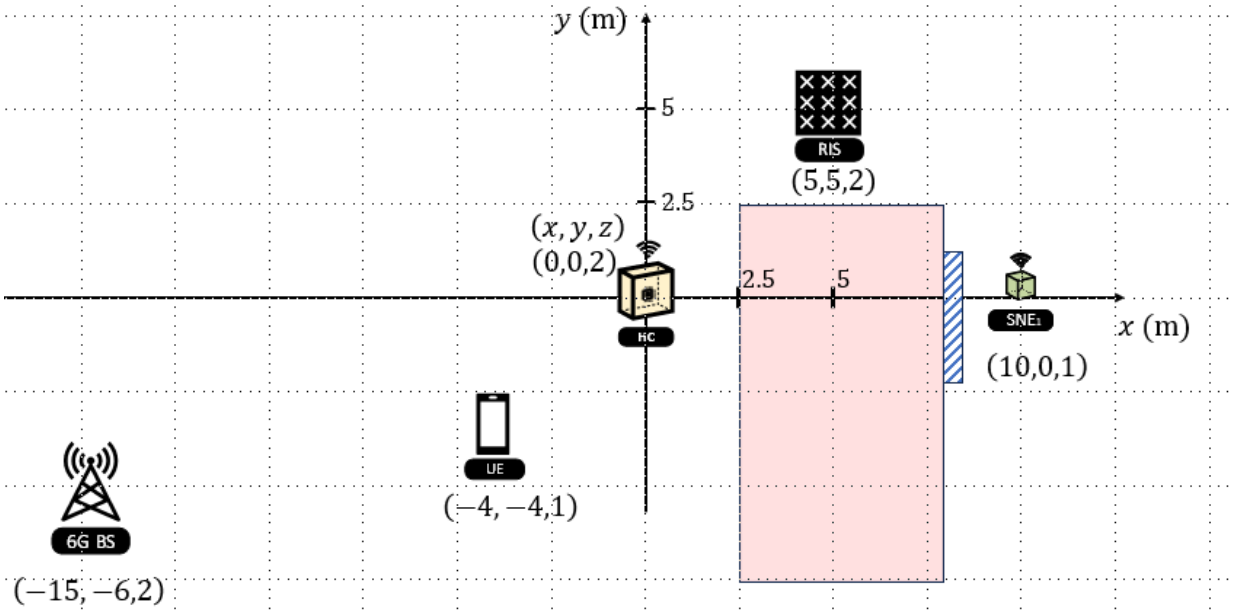

Figure 27. Geometry of numerical experiment. SNE_2 is located inside the read shaded area (uniform distribution).

For the considered setup we report results for the quantity $SIR_2(\sigma^{\text{opt}})/SIR_2(\sigma = \mathbb{1})$, i.e., the increase of SIR using an optimized permutation compared with a standard RIS. Note that this quantity is independent of γ_2, P_{HC}, and P_{BC} and is measuring the decrease of interference on SNE_2. However, it is unaware of whether or not the interference on SNE_2 is severe to start with; but for the setup considered in Figure 27 the interference is indeed considerable when the number of RIS elements is large.

We consider Rician channels in which the channel between any pair of antennas at distance d reads

$$h = \frac{\lambda}{4\pi}\left(\sqrt{\frac{K}{K+1}}e^{\frac{\jmath 2\pi d}{\lambda}} + \sqrt{\frac{K}{K+1}}t\right) \tag{91}$$

where t is a complex Gaussian random variable with variance 1, and K is the Rician factor. This channel model is valid for all channels except for the HC-SNE_1 channel which is assumed to be completely blocked. However, this is irrelevant for our purposes as the interference to SNE_2 is not dependent on the said channel. The results are presented in Figure 28.

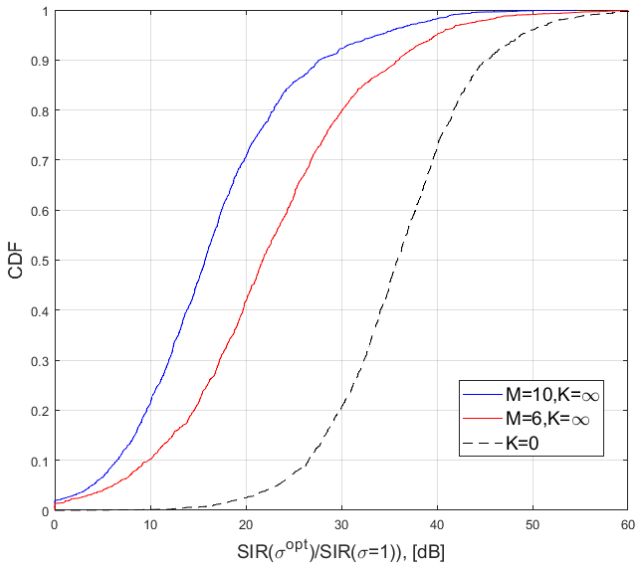

Figure 28. Numerical results for the setup in Figure 27.

We make the following remarks and observations:

- We only present results for $K \in \{0, \infty\}$ with the remark that for intermediate values, the curves fall in between those for $K = 0$ and $K = \infty$.
- For $K = 0$, i.e., a purely Gaussian channel, the value of M becomes irrelevant and therefore only a single curve is presented.
- Based on experiments beyond what is presented, the value of N plays only a very minor role, and the results are therefore generated for $N = 1$.
- Hefty gains are achieved in terms of interference reduction; median values are 16dB and 22dB for $M = 10$ and $M = 6$, respectively.
- The gains reported in Figure 28 cannot be taken as gains in SINR, as they merely measure interference reductions. If the interference is not severe to start with, the gains are irrelevant. However, for the geometrical setup in Figure 27, the interference is indeed large on SNE_2 due to the geometrical setup considered.
- When there is LOS, i.e., $K \approx \infty$, between the HC and the RIS as well as between the RIS and SNE_1, the SINR of SNE_1 is *unaffected* by the permutation. This is so since the transfer function of the RIS can maintain full gain in the configured direction.

5.1.2 Summary and recommendations

As a subnetwork is, ideally, to co-exist with other forms of systems, interference naturally arises. It has been observed herein, that the RIS of a RIS-assisted subnetwork may create interference to the subnetwork itself. This interference impacts SNEs not under direct control of the RIS. However, by changing the traditional RIS architecture into a non-diagonal RIS architecture, and more specifically, the P-RIS architecture, said interference may be eliminated. In this section we have demonstrated interference reductions in the range of 10-30 dBs for realistic subnetwork deployments.

Such gains are of major importance, and our recommendation is that future RIS-assisted subnetworks should deploy P-RISs whenever the scenario is interference limited.

5.2 Coordinated subnetworks aided by RIS deployment

5.2.1 Introduction

In this section, multi-path availability for the subnetwork supported by the RIS are again addressed. It is considered this time the computational constraints in the subnetworks for the coding operations. Methods for optimal FPC packets routing strategies are devised, considering different radio link and data requirements. In this section, the focus is increased reliability, reduced latency and spectrally efficient data routing techniques, such as duplication, split, and selective mappings.

Figure 29 illustrates a cooperative subnetwork scenario, where an HC node in subnetwork 1 exploits the path diversity available to it, with a direct link to the 6G-BS, an indirect link to the 6G-BS via a RIS node, and an HC node in subnetwork 2. Both subnetwork 1 and subnetwork 2 are capable of generating coded packets, where in the case of subnetwork 2, this operation is named recoding. Recoding enables intermediate transport nodes and storage caches to combine coded packets to create new coded packets that are effective representations of all original packets involved in the first coding stage. Cooperative subnetwork scenarios may greatly benefit from the presence of a RIS, that can help increasing coverage for the subnetworks. This is particularly useful in moving subnetworks, and where all subnetworks involved cooperate for the use case and transmission requirement goals. The presence of elements of a second subnetwork that can perform recoding operations, also contributes to the robustness of the coding procedures, allowing for offloading of the FPC coded packet operations.

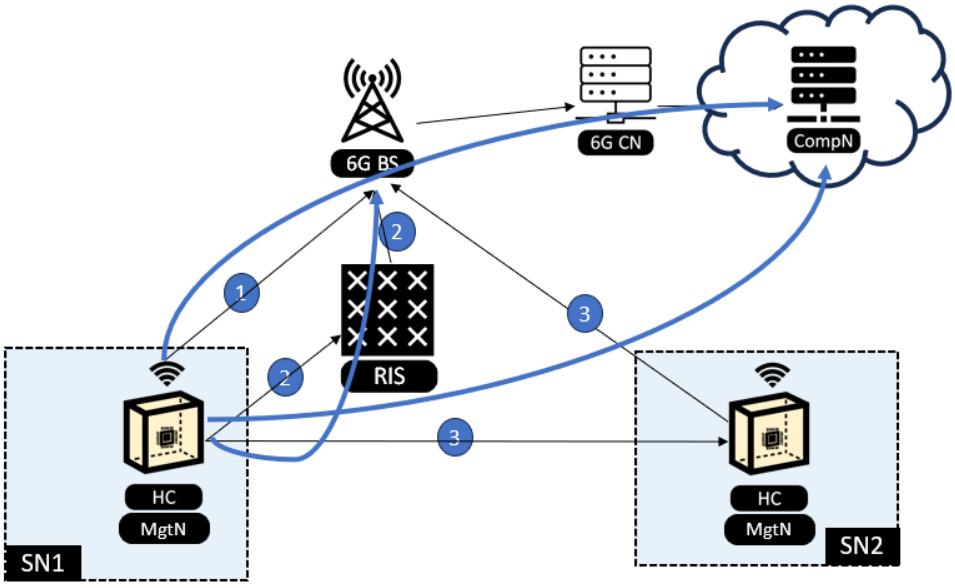

Figure 29. Cooperative subnetwork scenario for coded packet transmission

The blue lines indicate coded packet transmission routes, with the compute end point for data being in the 6G-CN. These lines are representations of channel 1, and cascaded channels 2 and 3. The considered problem and solution design relates to exploitation of the available suitable paths for the HC node transmitter, considering the limitations and characteristics of the deployed RIS, and the strategy to transmit NC PDUs.

5.2.2 Path selection for transmission of NC PDUs

As described in Section 4.1.4, suitable/preferred path for transmission of an NC PDU can be determined based on suitability of the path to meet QoS requirements of the NC PDU, such as reliability and latency. A suitable/preferred path may also be characterized by the presence of an intermediate node that can perform recoding on the original

coded packets received from a source node from another subnetwork. Such paths may be preferred for transmission of NC PDU with high importance to enable retransmission of NC PDUs from the intermediate nodes without requiring retransmission of original NC PDUs from the source node which can be useful, e.g., if there is link failure/loss of connection between source node and intermediate node, or the source node is a power limited node. There may be multiple suitable paths available, which may support different levels of reliability or latency, for transmission of NC PDUs to a destination node. Since NC PDUs associated with an NC generation have different importance, number of paths for transmission of NC PDUs may be selected based on their characteristics or importance, link quality of available paths and the suitability of available paths to meet required QoS level. For instance, if delay budget of NC PDUs associated with an NC generation is below a threshold, all suitable paths are selected for transmission of NC PDUs. Otherwise, single path from multiple suitable paths is selected for transmission of NC PDUs with lower importance and multiple paths are selected for transmission of NC PDUs with higher importance.

5.2.3 Strategy for NC PDUs transmission

There can be several mechanisms to transmit the NC PDUs generated using an NC generation via the suitable paths. These include duplication, split, and selective mapping mechanisms, which are detailed below.

5.2.3.1 Duplication mechanisms

In rule-based duplication, the HC transmitter may use a duplication rule based on one or more of the following characteristics of NC PDUs to determine transmission mechanism of NC PDUs generated using an NC generation via the suitable paths:

- Type of NC PDU, like systematic NC PDU, non-systematic NC PDU, where the HC transmitter may perform duplication of systematic NC PDUs whereas non-systematic NC PDUs may be transmitted via single suitable path.
- Innovativeness of NC PDUs, where the HC transmitter may perform duplication of innovative or more-innovative NC PDUs generated using an NC generation whereas non-innovative or less-innovative NC PDUs may be transmitted via single suitable path.
- Remaining Delay budget of NC PDUs, where the HC transmitter may perform duplication of NC PDUs with low remaining delay budget (e.g. below a threshold) whereas NC PDUs with high remaining delay budget (e.g. above a threshold) may be transmitted via single suitable path.
- Delay budget of NC SDUs i.e. required latency for recovery of NC SDUs associated with the NC generation used to generate NC PDUs, where the HC transmitter may perform duplication of NC PDUs if the remaining delay budget of the NC SDUs associated with the NC generation used to generate the NC PDUs is low (e.g. below a threshold), and whereas NC PDUs can be transmitted via single suitable path if the remaining delay budget of the NC SDUs associated with the NC generation used to generate the NC PDUs is high (e.g. above a threshold).
- Importance of NC PDU (see definition in section 4.1.1), where the HC transmitter may perform duplication of NC PDUs with high importance (e.g. importance above a threshold) whereas NC PDUs with low importance (e.g. importance below a threshold) may be transmitted via single suitable path.
- NC PDU volume based-duplication where the HC transmitter may perform duplication of $X + X_n$, wherein X_n may be positive or negative integer, NC PDUs generated using an NC generation. Whereas remaining $Y - X - X_n$ NC PDUs generated using the NC generation may be transmitted via single suitable path.

5.2.3.2 Split mechanisms

In rule based split mechanisms, the HC transmitter may transmit one or more NC PDUs generated using an NC generation via different paths based on the following:

- Type of NC PDU, like systematic NC PDU, non-systematic NC PDU, where the HC transmitter may transmit systematic NC PDUs, generated using an NC generation, via a first suitable path and transmit non-systematic NC PDUsvia a second suitable path.

- Innovativeness of NC PDUs, where the transmitter may transmit innovative or more-innovative NC PDUs, generated using an NC generation, via a first path and non-innovative or less-innovative NC PDUs, may be transmitted via a second path.
- Remaining delay budget of NC PDUs, where the transmitter may transmit NC PDUs with low remaining delay budget (e.g. below a threshold) via a first whereas NC PDUs with high remaining delay budget (e.g. above a threshold) are transmitted via a second path.
- Delay budget of NC SDUs i.e. required latency for recovery of NC SDUs associated with the NC generation used to generate NC PDUs, where the transmitter may transmit NC PDUs via a first path if the remaining delay budget of the NC SDUs associated with the NC generation used to generate the NC PDUs is low (e.g. below a threshold) where the NC PDUs are transmitted via a second path if the remaining delay budget of the NC SDUs associated with the NC generation used to generate the NC PDUs is high (e.g. above a threshold).
- Importance of NC PDU wherein importance of NC PDU, where the transmitter may transmit NC PDUs, generated using an NC generation, with higher importance (e.g. higher than a first threshold) via a first path (e.g. RLC entity) and transmit NC PDUs, generated using an NC generation, of lower importance (e.g. lower than a first threshold) via a second path.
- NC PDUs volume-based split wherein transmitter may transmit X_{thr} NC PDUs generated using an NC generation via a first path whereas remaining $Y - X_{thr}$ NC PDUs may be transmitted via a second path.

5.2.3.3 Selective mapping mechanisms

Selective mapping mechanisms are hybrid mapping methods where the HC transmitter may transmit a first set of NC PDUs generated using an NC generation via first set of paths, and a second set of NC PDUs generated using an NC generation is transmitted via a second set of wherein a set of paths consists of one or more paths. In this mechanism, a first set of paths does not fully overlap with a second set of paths or vice versa (i.e. there is at least one mutually exclusive path associated with each set of paths). HC transmitter may further perform duplication of the NC PDUs from first set of NC PDUs among the paths forming the first set of paths and the NC PDUs from second set of NC PDUs may be duplicated among the paths forming the second set of paths.

5.2.4 Activation/selection of NC PDU transmission strategy

There can be several reasons for the HC transmitter to activate an NC PDU transmission strategy, i.e., the transmission strategy of the previous section, and those can include the following:

- Configuration of a specific strategy from the 6G-BS.
    - HC transmit node can be configured with an NC PDU transmission strategy, e.g., via RRC signalling.
- An activation signalling for NC PDU transmission strategy
    - HC transmitter may be configured with one or more NC PDU transmission strategies. 6G BS can further activate a specific NC PDU transmission strategy from the configured multiple strategies via control signalling (e.g. MAC CE or DCI).
- Activation of an NC configuration.
    - An HC transmit node may be configured with one or more NC PDU transmission strategies, a set of NC configurations and a mapping between NC configurations and NC PDU transmission strategies. The transmit node may further receive an activation signalling from the network activating an NC configuration. The node determines the associated NC PDU transmission strategy is activated upon reception of signalling form the network activating the NC configuration.

The HC transmit node may also be configured to use multiple NC PDU transmission strategies. The 6G BS can also configure the transmit node with rules or conditions to determine which mechanism to use to transmit NC PDUs generated using an NC generation via the suitable paths. Transmit node can be configured with conditions for use of NC PDU transmission strategies, including the following:

- Radio conditions e.g. link quality based on radio measurements, transmission delay on the air interface, another proxy metrics such as success ratio of NC PDUs transmission, number of L2/L1 retransmissions of the paths.
    - If link quality on available paths is equal or below a configured threshold, transmitter can perform duplication of NC PDUs e.g. rule based duplication, selective mapping etc. to enhance reliability of NC PDU transmission. Otherwise, transmitter may use a split mechanism to transmit the NC PDUs via multiple suitable paths, or the HC may transmit NC PDUs via a single suitable path if link quality is equal or above a configured threshold.
    - If lower latency transmission is required, HC transmitter can consider transmission delay on the air interface on available suitable paths to adapt a transmission strategy for NC PDUs. For example, if transmission delay on air interface is equal or above a configured threshold, transmit node may use a split mechanism e.g. rule based split or selective mapping.
- NC code rate
    - If NC code rate is equal or above a configured threshold, transmit node may perform duplication of NC PDUs e.g. rule based duplication, selective mapping etc. to enhance reliability of NC PDU transmission. Otherwise, it may use a split mechanism to map the NC PDUs to suitable paths. Or, it may map NC PDUs to single path if NC code rate is equal or below a configured threshold.
- Latency requirement of NC PDUs
    - If the remaining delay budget of NC PDUs is equal or below a configured threshold, HC transmit node use a split mechanism e.g. rule based split or selective mapping, where the NC PDUs generated using one or more NC generations are transmitted via two or more suitable paths to support reception of NC PDUs within a certain delay bound. Otherwise, it may use a strategy where it performs duplication of NC PDUs across two or more suitable paths. Or transmit node HC may transmit NC PDUs via a single suitable path if remaining delay budget of NC PDUs is equal or above a configured threshold.
- Required latency for recovery of NC SDUs associated with the NC generation used to generate NC PDUs
    - If required latency to recover NC SDUs associated with the NC generation used to generate NC PDUs is equal or below a configured threshold, transmit node may use a split mechanism e.g. rule based split or selective mapping, where the NC PDUs generated using the NC generations are transmitted via two or more suitable paths to support recovery of NC SDUs associated with the NC generation within a certain delay bound. Otherwise, it may use a mechanism wherein it may perform duplication of NC PDUs across two or more suitable paths, or it may transmit NC PDUs via a single suitable path if required latency to recover NC SDUs associated with the NC generation used to generate NC PDUs is equal or above a configured threshold.

5.2.5 Transmission of NC PDUs via suitable paths

An HC transmit node can determine how to transmit each NC PDU generated using an NC generation via available paths based on the activated (e.g. signalled by the 6G-BS or selected by the transmit node) NC PDU transmission strategy and/or the associated NC related conditions which may be a function of one or more of the following factors:

- Link quality between transmitter and receiver, including the RIS
- NC PDU characteristics e.g. type, importance, innovativeness etc.
- NC PDU transmission attempt e.g. first transmission or retransmission.
- NC SDU transmission attempt e.g. first transmission or retransmission.
- NC PDU volume threshold e.g. (pre)-configured or determined by HC.
- NC code rate of the NC generation.
- Lower layers configuration e.g. carrier type, cell group type, radio link control (RLC) mode of data transfer, allowed grant attributes (e.g. NC PDU characteristics, MCS values, grant type etc.) configured for the RLC entities etc.

Specifically, the HC transmit node may determine how to route the NC PDU to suitable paths based on the following:

- Link quality between transmitter and receiver.
    - For example, selective mapping for transmission of NC PDUs may be activated, transmit node HC may determine whether to perform duplication of a set of NC PDUs among a set of suitable paths based on link quality between transmitter and receiver. For example, if link quality on one or more paths is below a threshold, transmit node may duplicate NC PDU from first set of NC PDUs across the suitable paths in a first set of paths and it may duplicate NC PDU from second set of NC PDUs across the suitable paths in a second set of paths. Otherwise, transmitter may duplicate NC PDUs from first set of NC PDUs across the suitable paths in a first set of paths and transmit NC PDUs from a second set of NC PDUs to one suitable path from the second set of paths.
    - For example, if channel condition (e.g. based on radio measurement etc.) on the available paths is above a threshold (i.e. good channel condition), HC transmit node may transmit NC PDUs of a first set of NC PDUs (e.g. NC PDUs with high importance or importance above a threshold) via one or more associated with a first set of lower layers configuration and NC PDUs of a second set of NC PDUs (e.g. NC PDUs with low importance or importance below a threshold) are transmitted via one or more paths associated with a second set of lower layers configuration, where the first set of lower layers configuration provide higher transmission reliability than the second set of configuration e.g. via higher number of configured grant repetitions, aggregation factor, a first set of (e.g. lower order) MCS values etc.
- NC PDU characteristics e.g. type, importance, innovativeness etc.
    - A strategy which supports duplication (such as selective mapping, rule-based duplication etc.) of NC PDUs may be activated e.g. due to poor radio conditions on available paths. Transmit node may duplicate an NC PDU across two or more suitable paths if the NC PDU is e.g. systematic, more innovative, has high importance etc. Whereas, if the NC PDU is e.g. non-systematic, less innovative, has low importance, etc, it is transmitted via one suitable path.
    - Assuming a split mechanism is activated, if NC PDU is of first type (e.g. systematic NC PDU, more innovative etc.), it may be transmitted via a first set of one or more paths with better link quality (e.g. based on radio measurement) than a second set of paths. Whereas NC PDU of second type (e.g. non-systematic NC PDU) is transmitted via second set of paths.
- NC PDU transmission attempt e.g. first transmission or retransmission.
    - Assuming duplication mechanism for transmission of NC PDUs is activated (e.g. due to poor radio conditions), transmit node can determine whether to perform duplication based on whether it is retransmitting the NC PDU or not. Specifically, it may duplicate NC PDUs if they are being retransmitted. Otherwise, it may not duplicate NC PDUs across multiple paths.
    - Transmit node may perform initial transmission of an NC PDU via one or more suitable paths which provide a certain level of transmission reliability. Whereas it may perform retransmission of NC PDU via a set of suitable paths which provide higher transmission reliability than the paths used for initial transmission.
- NC PDU volume threshold e.g. configured by the network or determined by transmit node.
    - Assuming a mechanism which supports duplication of NC PDUs is activated e.g. due to poor radio conditions on available paths, transmit node may duplicate $X + X_n$ NC PDUs out of Y NC PDUs generated using an NC generation across suitable paths, whereas it may transmit remaining, i.e. $Y - X - X_n$, NC PDUs generated using the NC generation via single suitable path. Herein, X_n is the number of NC PDUs, in addition to the minimum number of NC PDUs required to recover NC SDUs, which are duplicated across multiple suitable paths. X_n can be configured by the network and its actual value used by the transmit node may be a function of radio conditions.
    - Assuming a split mechanism to transmit NC PDUs generated using an NC generation via different sets of paths is activated e.g. to meet delay budget requirement of the NC generation used to generate NC PDUs, the HC transmit node may route X_{thr} NC PDUs out of, e.g., Y NC PDUs generated using an NC generation to first set of suitable paths, whereas it may route $Y - X_{thr}$ NC PDUs generated using the NC generation to second set of suitable paths, whetein threshold X_{thr} can be indicated by the network. First set of paths may provide transmission with higher

reliability (e.g. better link quality, configured with data transmission for higher reliability such as lower order MCS etc.) than the second set of paths or vice versa.

- NC code rate of the NC generation.
    - Assuming a mechanism which supports duplication of NC PDUs is activated e.g. due to poor radio conditions on available paths, the HC transmit node may determine whether to perform duplication based on NC code rate of the generation used for generating NC PDU. For instance, it may duplicate an NC PDU across the suitable paths, if NC code rate of the generation used to generate the NC PDU is above a threshold. Otherwise, it transmits NC PDU via only one suitable path.
    - Assuming a split mechanism is activated e.g. due to large transmission delay on available paths, the HC transmit node can determine to map NC PDUs generated using an NC generation to one or more paths, based on code rate of NC generation used to generate NC PDUs. Specifically, if NC code rate of an NC generation used to generate NC PDUs is below a threshold, it may map NC PDUs to a first set of paths. Otherwise, if code rate of NC generation used to generate NC PDUs is above a threshold, it may map NC PDUs to a second set of paths wherein the second set of RLC entities may be configured with lower layer configurations which may provide higher transmission reliability than the lower layer configuration configured for the first set of RLC entities.
    - For example, if NC code rate of an NC generation used to generate NC PDUs is below a threshold, the HC transmit node may map a first set of NC PDUs (e.g. NC PDUs with high importance) to one or more paths associated with a first set of lower layers configuration where it may map second set of NC PDUs (e.g. NC PDUs with low importance) to one or more paths associated with a second set of lower layers configuration, wherein the first set of lower layers configuration may provide higher transmission reliability than the second set of configuration.

5.2.6 Conclusion

FPC can provide higher reliability benefits to transfer large volumes of data in the context of subnetworks. FPC and FPC coded PDU routing techniques presented in this section can be applied to any radio layer, providing additional flexibility in deployment. Current cellular systems do not yet operate with FPC strategies and procedures, and their deployment in subnetwork topologies, where transmitting nodes have to, in many instances, transmit high volumes of data, can be vital for their adoption in future cellular system releases. Adaptive mapping of NC PDUs to links configured for data transfer with higher reliability, as a function of radio conditions and characteristics of NC PDUs can increase probability of successful data transmission within a certain delay bound and reduce waste of system resources.

6 RIS DESIGN FOR ULTRAWIDE BANDWIDTH SIGNALS

An interesting by-product of the activity of RISs developed in project is related to the exploitation of RISs in the context of ultrawide bandwidth (UWB) signals for particular applications falling within the consumer category. Even though such topic and applications were not originally foreseen in the project proposal, the study addressed novel aspects of RIS design that have been overlooked so far and might have an important impact for next-generation RIS technology.

Although the to-be-presented solution has been studied in the context of the 'public transport fare collection' use case as studied by the Fine Ranging Alliance (FiRa), it can be used for use cases where a large density of entities (e.g., humans, robots, etc.) may affect the communication with a central node due to obstructions.

6.1 RIS for UWB fare collection (and other similar) systems

Recently there has been some interest in adopting RISs for UWB systems. One prominent such example is within the FiRa where specifications are developed to support the "public transport fare collection" use case, see [36].

Let us first provide a few further details around this use case. In many cities public transport networks form a critical part of the infrastructure that allows the inhabitants to travel to their wanted destinations. Especially during rush hours, public transport networks are under constant strain with about one person per second per gate. Figure 30 summarizes the high-capacity requirements, assuming up to two passengers per square meter.

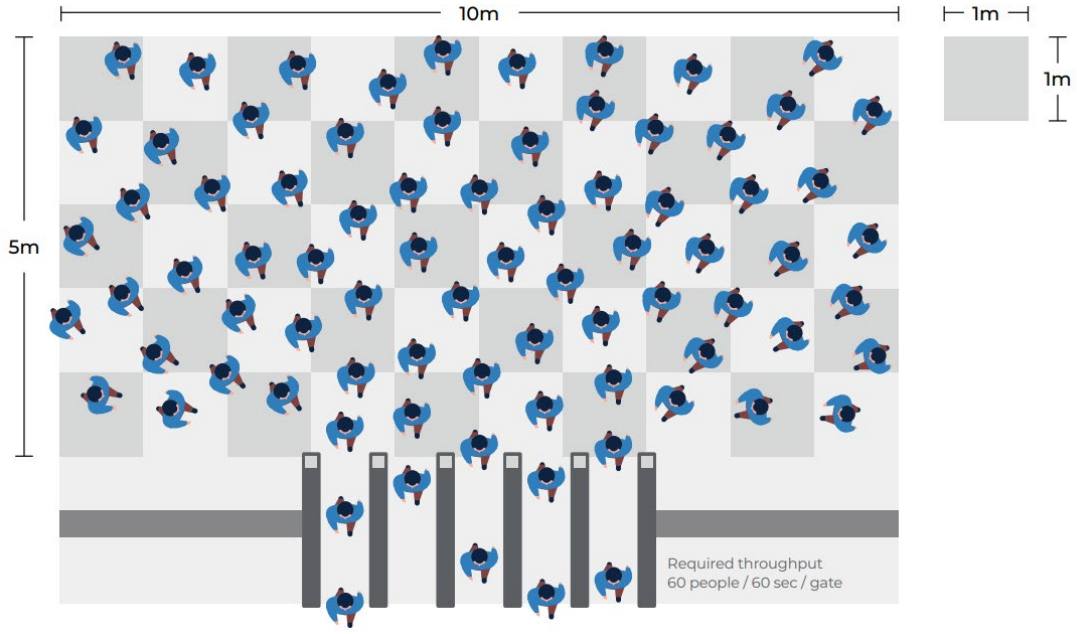

Figure 30. A passenger flow in a public transport station.

Legacy technology requires passengers to manually tap in and out of the system. Removing the manual interaction speeds up the process and makes the entire transport experience more streamlined. Passengers using a UWB-based touchless fare transaction system simply walk through the gate, immediately obtaining access with the

appropriate ticket. Such a system enables transport operators to improve throughput while providing a superior and seamless access experience to their customers.

A challenge for UWB-based fare collection is to achieve sufficient performance to allow the UWB devices at the transit gates to position and communicate with passengers that are blocking the line-of-sight path for each other as they approach the gates (see Figure 31).

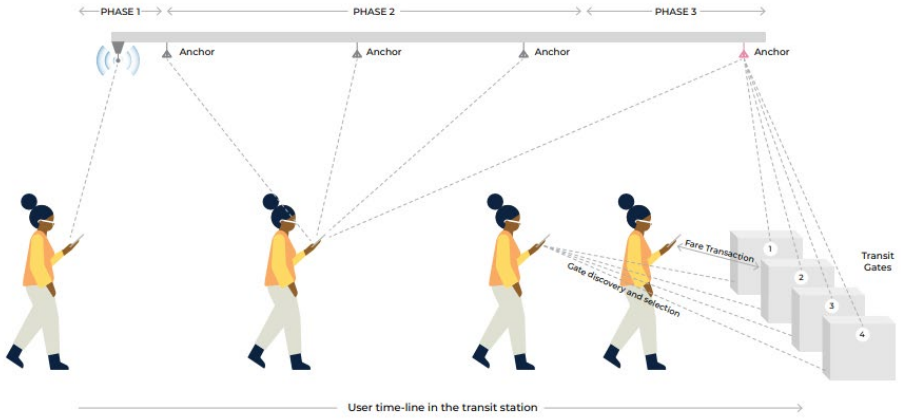

Figure 31. Passenger obstructing LOS for persons behind

For this, and similar use cases, RISs may potentially mitigate shortcomings that have been identified by FiRa. However, as we shall shortly see, there are severe issues with positioning applications for UWB based on RIS technology.

6.1.1 RIS in UWB systems: The narrowband assumptions are no longer valid

A general assumption in wireless communications is the *narrowband assumption*; RISs are almost always studied on this basis. However, for systems with wide bandwidths and/or RISs with large aperture, the narrowband assumption breaks. This brings about new challenges, but also opportunities.

Let us briefly discuss the narrowband assumption for a RIS. Assume that a signal $s(t)$ is transmitted from a transmitter towards an N-element RIS and consider the reflected signal received at a receiver point. The transmitted signal may be expressed as

$$s(t) = \exp(\jmath 2\pi f_c t)\beta(t) \tag{92}$$

where f_c is the RF carrier and $\beta(t)$ is the information bearing signal whose bandwidth, W, satisfies $W \ll f_c$. Each of the N element receives the signal, applies a phase shift, and then re-radiates the signal. Altogether, this produces a signal at the receiver, in the absence of noise, which reads

$$r(t) = \alpha \sum_{n=1}^{N} s(t-\tau_n)\exp(\jmath\theta_n) \tag{93}$$

where α is a common path loss for all elements, τ_n is the total propagation delay the signal undergoes through RIS element n, and θ_n is said phase shift at element n.

Inserting (92) into (93) produces

$$r(t) = \alpha \exp(\jmath 2\pi f_c t) \sum_{n=1}^{N} \exp(-\jmath 2\pi f_c \tau_n)\beta(t-\tau_n) \exp(\jmath\theta_n) \tag{94}$$

The narrowband assumption consists of arguing that $\tau_n \ll 1/W$. Loosely speaking, the quantity $1/W$ measures the rate of change of the signal $\beta(t)$, and the narrowband assumption implies that the signal $\beta(t)$ "does not change much" during τ_ℓ seconds. Thus, approximately, we have $\beta(t-\tau_\ell) \approx \beta(t)$. Thus

$$r(t) \approx \alpha \exp(\jmath 2\pi f_c t)\beta(t) \sum_{n=1}^{N} \exp(-\jmath 2\pi f_c \tau_n) \exp(\jmath \theta_n) \tag{95}$$

An optimal RIS configuration is $\theta_n = 2\pi f_c \tau_n$ which results in

$$r(t) \approx \alpha N \exp(\jmath 2\pi f_c t)\beta(t) = \alpha N s(t) \tag{96}$$

By outright inspection, one may observe that the received signal $r(t)$ is an undistorted version of the transmit signal $s(t)$, but where an amplitude scaling of N is achieved. Unfortunately, the narrowband assumption breaks for large bandwidth and/or large aperture RISs.

Example 1. Consider a UWB system according to any of the IEEE802.15.4 specs. The bandwidth is $W = 500\text{MHz}$ and a 2ns duration pulse shape is used. In Figure 32 the use case/subnetwork of particular interest to Sony is shown. A user (in pink uniform) is to connect to a hub by means of where LOS is blocked. The propagation path "b" is $\approx 0.77\text{m}$ longer than propagation path "a"; the height of the user is 1.5m. This implies a $\approx 2.6\text{ns}$ time difference between these two paths. Now, with a 2ns pulse duration, it is obvious that the narrowband assumption $\beta(t - 2.6 \times 10^{-9}) \approx \beta(t)$ is not applicable. ■

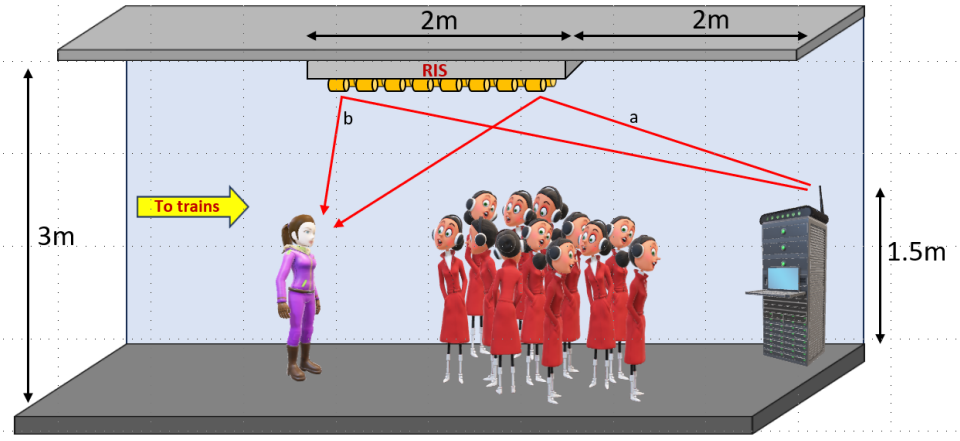

Figure 32. The use case discussed in Example 1, and by FiRa public transport fare collection system.,

The difference is propagation delay across the RIS is not a consequence of the short distances between the RIS and the transmitter/receiver. A difference in propagation distance very similar to the 2.6 ns of Figure 32 emerges almost independently of the location of the receiver/transmitter. Whether or not the narrowband assumption may be invoked for a RIS depends on (the interplay of) two items: a) The bandwidth W, b) The aperture of the RIS.
So, why does all of this matter? The answer to this is manyfold, and we list a few reasons next.

1. **Loss of beamforming gain.** The power gain of an N-element RIS is N^2. But a precondition for this gain is that the narrowband assumption holds, otherwise a radical reduction of beamforming gain occurs.
2. **Loss of positioning and synchronization accuracy**, in both synchronization and positioning, the receiver should correlate the received signal with the transmit. But as the received waveform is distorted due to differences in propagation delays, a performance loss occurs.
3. **Complexity increases at the receiver and worse throughput.** Large propagation delay differences imply inter symbol interference (ISI). Unmitigated ISI at the receiver has devastating consequences. Unfortunately, countermeasures computationally and anyway yield a performance degradation that may be substantial.

6.1.2 A tunable hardware architecture for mitigating propagation delays. In some scenarios there is no need for tunability.

In UWB systems all elements at the RIS cannot be considered to give the same propagation delay. However, the differences in propagation delay are sufficiently small for compensating for them by means of delay lines. In the example outlined in Figure 32, the difference in propagation delay is a mere $0.77\mathrm{m}$. This would correspond to an additional delay line of $\approx 0.385\mathrm{m}$ which is feasible to be implemented. Thus, with UWB we are in a situation where RIS compensation for propagation delays are meaningful and feasible at the same time.

Contemplating upon the example in Figure 32, one may realize that the differences in propagation delays depend on the geometry. If the RIS beamforms to another direction the propagation delays change. Thus, it is desirable that the delay compensation is tunable. A RIS element with L different delays is shown in Figure 33. The RIS element is tuned by configuration of the $L-1$ switches.

For the implementation of delay line, multiple variants can be used, including Microstrip Delay Lines, lumped element delay line, Surface Acoustic Wave (SAW) Delay Lines, etc. Microstrip delay line is one of simplest implementation where the RIS element is terminated with multiple microstrip lines with different length as depicted in Figure 33. However, such an implementation usually requires a large footprint, and may cause high insertion loss if the substrate under the microstrip line is lossy. Instead of using lumped element or SAW component to create delays, it can effectively reduce the footprint size compared to microstrip line approach. In addition to those passive delay lines, active delay lines by using a single or multiple transistors is also possible, which its delay can be controlled by the biased voltage or current via the transistors.

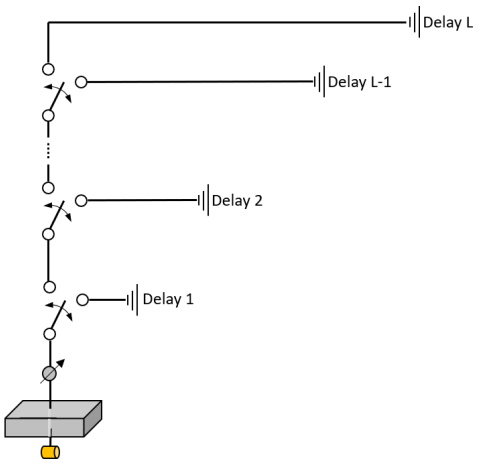

Figure 33. A RIS element with tuneable delay (L different delays)

6.1.3 Necessary signalling for enabling positioning functionality for the modified RIS

For positioning/ranging applications based on a RIS with delay compensation, standardized signalling is needed. To see why this is the case, let us first go through how it is carried out conventionally.

Consider the case of two single antenna SNEs, 1 and 2. Based on two-way-ranging, these two SNEs may establish the distance between them. A two-way-ranging procedure is carried out according to Figure 34. SNE 1 transmits an initial “poll” signal. This poll is received at SNE 2, which transmits a signal towards SNE 1. SNE 1 receives the response signal and transmits a second signal. Finally, the time-of-flight can be determined by simple calculation according to the formula shown in Figure 34.

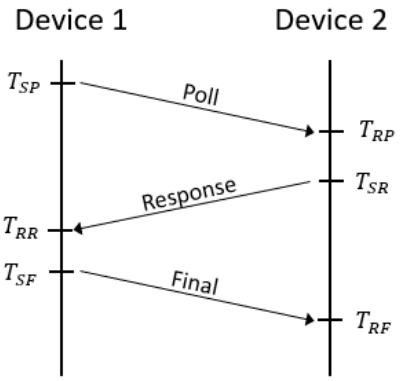

$$\text{Distance} = \text{TOF} \times (\text{speed of light})$$

$$\text{TOF} = \frac{(T_{RR} - T_{SP}) - (T_{SR} - T_{RP}) + (T_{RF} - T_{SR}) - (T_{SF} - T_{RR})}{4}$$

Figure 34. Two-way-ranging protocol and computations

Unfortunately, this computation does not carry over to delay-compensating RISs. Assume that each RIS element adds a delay ν_n. The received signal at SNE 2, from a transmitted signal at SNE 1 reads

$$r(t) = \alpha \exp(\jmath 2\pi f_c t)\beta(t - \tau_n - \nu_n) \sum_{n=1}^{N} \exp(-\jmath 2\pi f_c(\tau_n + \nu_n)) \exp(\jmath\theta_n) \tag{97}$$

Define $\tau_{\max} = \max_n \tau_n$. This is the largest delay across the RIS and represents the longest propagation distance from SNE 1 to SNE 2 via any RIS element. We may now take ν_n as $\nu_n = \tau_{\max} - \tau_n$ to reach

$$\begin{aligned} r(t) &= \alpha \exp(\jmath 2\pi f_c t)\beta(t - \tau_n - \nu_n) \sum_{n=1}^{N} \exp(-\jmath 2\pi f_c(\tau_n + \nu_n)) \exp(\jmath\theta_n) \\ &= \alpha \exp(\jmath 2\pi f_c t)\beta(t - \tau_{\max}) \sum_{n=1}^{N} \exp(-\jmath 2\pi f_c \tau_{\max}) \exp(\jmath\theta_n) \end{aligned} \tag{98}$$

To maximize the SNR, the phase shifts are $\theta_n = 2\pi f_c \tau_{\max}, \forall n$. Thus, $r(t) = \alpha N \exp(\jmath 2\pi f_c t)\beta(t - \tau_{\max})$. This implies that the entire RIS may be seen as a single reflection point from the perspective of the receiving SNE. As such, a single reception time, say, T_{RP} for the "poll" signal is defined. However, the difference $T_{RP} - T_{SP}$ no longer corresponds to the actual propagation time between SNE 1 and SNE 2.

To resolve the situation, one may define a reference element at the RIS; for simplicity element 1. We may now define a RIS processing delay as the RIS added delay for this reference element, i.e.,

$$\Delta = \tau_{\max} - \tau_1 \tag{99}$$

The implication of this is that the quantity $T_{RP} - T_{SP} - \Delta$ *represents the time of flight between SNE 1 and SNE 2, via the RIS, where the RIS is a single point located at the reference element.*

A TOF may now be computed in a similar manner to the computation made in Figure 34. We show the amended protocol in Figure 35.

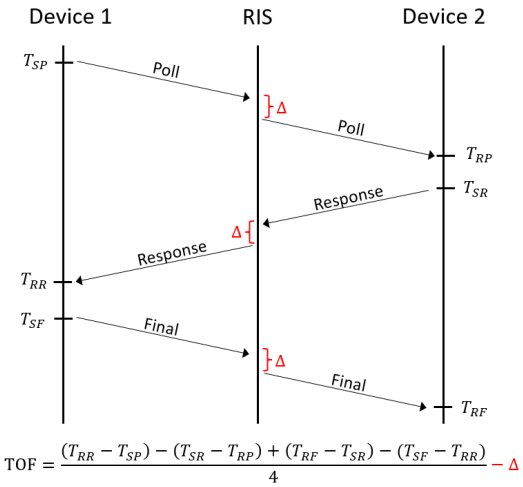

Figure 35. RIS assisted two-way-ranging protocol and computations. The diagram is made for the reference element, but this is equivalent to a situation in which the entire RIS is represented as a single point at said reference element's location

The so computed TOF represents the time of flight for the signal path:

$$SNE\ 1 \rightarrow RIS\ reference\ element \rightarrow SNE\ 2 \tag{100}$$

To utilize this TOF for positioning applications the value Δ must be known. But this value depends on the RIS geometry and the configured beam direction and may be known only to the RIS. In certain scenarios this may not pose any issues. For example, in private subnetworks, where the RIS and all anchor nodes are jointly installed, the value of Δ would be at hand to the anchor nodes. But in other applications, the devices may have no knowledge of the RIS implementation wherefore Δ is not known. Moreover, the value of Δ is beam specific. When the RIS beam changes, the associated value of Δ also changes. This has consequences for positioning applications.

6.1.4 Discussion and numerical experiments

The fact that RIS elements experience different delays may be an advantage in some cases. As discussed earlier, a RIS naturally offers a beamforming power gain of N^2. However, a second, additional, beamforming gain emerges from a delay-compensating RIS. This appears to be an unrecognized fact in contemporary literature and is noteworthy.

Consider a signal $\beta(t)$ acting as a synchronization signal. The objective for the receiver is to determine when (and if) the transmitter has transmitted signal $\beta(t)$. The standard way for doing so is to, after down conversion to baseband, perform a correlation between the received baseband signal and $\beta(t)$.

Ignoring noise and the path loss α, the output of the correlator reads

$$\rho(t) = \int_{-\infty}^{\infty} r(\tilde{t})\beta^*(\tilde{t} - t)\,\mathrm{d}\tilde{t} =$$

$$= \sum_{n=1}^{N} \exp\left(-\jmath 2\pi f_c(\tau_n + \nu_n)\right) \exp(\jmath\theta_n) \int_{-\infty}^{\infty} \beta(\tilde{t} - \tau_n - \nu_n)\beta^*(\tilde{t} - t)\,\mathrm{d}\tilde{t} \tag{101}$$

Whenever the narrowband assumption is valid, we obtain

$$\rho_{\mathrm{NB}}(t) = \lambda(t - \tau_1) \sum_{n=1}^{N} \exp(-\jmath 2\pi f_c(\tau_n)) \exp(\jmath\theta_n) \tag{102}$$

where

$$\lambda(t) = \int_{-\infty}^{\infty} \beta(x+t)\beta^*(x)\,\mathrm{d}x \tag{103}$$

The receiver analyzes the signal $\rho_{\mathrm{NB}}(t)$ and determines that a signal is present at time $t = t_0$, where

$$t_0 = \arg\max_t \rho_{\mathrm{NB}}(t) \tag{104}$$

if $|\rho_{\mathrm{NB}}(t_0)| > T$. From the Cauchy-Schwarz inequality, it readily follows that the maximum of $\rho_{\mathrm{NB}}(t)$ occurs at $t = \tau_1$. Two aspects now determine the error performance of this detector, namely: (i) the beamforming gain, and (ii) the sharpness of the function $\lambda(t)$. As the function $\lambda(t)$ is not impacted by the number of RIS elements, N, it follows that the SNR experiences a "single" beamforming effect, namely, that from said beamforming gain. Let us now assume that the RIS beamforming weights are fixed and targets a specific location in physical space. Whenever the receiver is located exactly at this very position we have $\rho_{\mathrm{NB}}(t) = \lambda(t-\tau_1)N$. Consider now a perturbation of the receiver's position; this alters the delays τ_n into variables $\tilde{\tau}_n$. As the variable θ_n remains constant, it follows that we now have

$$\rho_{\mathrm{NB}}(t) = \lambda(t-\tilde{\tau}_1)\sum_{n=1}^{N} \exp(-\jmath 2\pi f_{\mathrm{c}}\tilde{\tau}_n)\exp(\jmath\theta_n) = \lambda(t-\tilde{\tau}_1)\widetilde{N} \tag{105}$$

where $\widetilde{N}$ is beamforming gain at the new position, and $|\widetilde{N}| < N$. Note that, since $\theta_n = 2\pi f_{\mathrm{c}}\tau_n$, we have

$$\widetilde{N} = \sum_{n=1}^{N} \exp(-\jmath 2\pi f_{\mathrm{c}}(\tilde{\tau}_n - \tau_n)) \tag{106}$$

Error performance is now governed by the new beamforming gain $\widetilde{N}$ and, as before, the sharpness of $\lambda(t)$ - but this is unaffected by the perturbation of the receiver's location.

With RIS delays, the situation changes. After the perturbation we have

$$\rho_{\mathrm{RISdelay}}(t) = \sum_{n=1}^{N} \exp(-\jmath 2\pi f_{\mathrm{c}}(\tilde{\tau}_n + \tau_{\max} - \tau_n))\exp(\jmath\theta_n)\int_{-\infty}^{\infty} \beta(\tilde{t} - \tilde{\tau}_n + \tau_n - \tau_{\max})\beta^*(\tilde{t}-t)\,\mathrm{d}\tilde{t} \tag{107}$$

By recalling that $\theta_n = 2\pi f_{\mathrm{c}}\tau_{\max}, \forall n$, this reduces to

$$\rho_{\mathrm{RISdelay}}(t) = \sum_{n=1}^{N} \exp\big(-\jmath 2\pi f_{\mathrm{c}}(\tilde{\tau}_n - \tau_n)\big)\,\lambda(t - \tilde{\tau}_n + \tau_n - \tau_{\max}) \tag{108}$$

Although somewhat complicated to see, this expression describes a ***double beamforming effect.*** Whenever the receiver is not in the exact location of the RIS beam, the correlation properties of the pulse $\beta(t)$ change. We may note that the complex exponentials, which describe the traditional beamforming effect, remain unaltered compared with the narrow band assumption. But, different from the narrowband assumption, there is not a unique time point where all pulses $\lambda(\cdot)$ are aligned. This implies that the magnitude of $\rho_{\mathrm{RISdelay}}(t)$ is in general smaller than that of $\rho_{\mathrm{NB}}(t)$ whenever the receiver is not at the exact center of the RIS beam. This is, in some cases, a desired effect. For example, in applications where the system should determine whether or not a device is in an *exact* spot, it is beneficial that the statistic forming the basis of the detection peaks when the device is at said spot and reduces sharply whenever it is not. With the narrowband assumption, the beamforming effect accomplishes this, but with RIS delays, we have the additional effect that the pulses $\lambda(\cdot)$ are misaligned outside of the RIS beam center. This fact may prove itself valuable in many future applications. Finally, we remark that without the RIS-compensating delays, the pulses $\lambda(\cdot)$ would not even be aligned at the RIS beam center. Thus, to furnish for a

situation in which the double beamforming effect comes into play, mitigating differences in propagation delays is crucial.

We provide a numerical example of the double beamforming effect next. In Figure 36 we show an example setup. A 41-element RIS (linear array assumed) is deployed 2m above ground and 8 meters horizontally away from the transmitter; said transmitter has an "x"-coordinate of 0m and is placed at floor level. The transmitter suffers from blockage so there is no LOS to area just behind the blockage. The beamforming configuration of the RIS is set to point downwards. A user is assumed to move along the axis labeled x_0, and we assume that the user moves from the marker "7m" to the marker "9m". In doing so, said user will pass by the exact RIS center (at "8m").

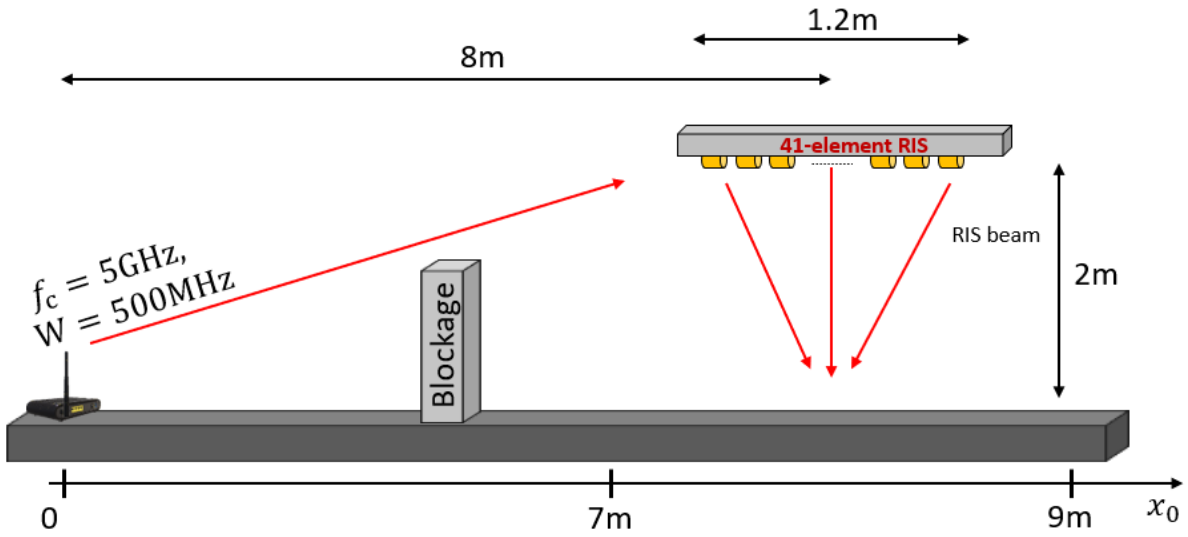

Figure 36. Geometrical setup for the numerical example discussed

As the user moves along its trajectory, we show the resulting functions $\rho(t)$. As these are now functions of x_0, we use notation $\rho_{\text{RISdelay}}(t; x_0)$, $\rho_{\text{RIS}}(t; x_0)$, and $\rho_{\text{NB}}(t; x_0)$. The function $\rho_{\text{RIS}}(t; x_0)$ is the corresponding function for a RIS without any delay compensation. Furhter, $\rho_{\text{NB}}(t; x_0)$ is entirely artificial; this is what would have happened if the bandwidth W could be assumed small in comparison with the RIS delay differences. It serves the purpose of a benchmark.

In Figure 37-Figure 39, we show said three functions. The double beamforming effect is clearly visible by comparing the sidelobes in Figure 37, Figure 38. Loosely speaking, the more pronounced the main peak is, the better the performance in detecting when a user is exactly under the RIS. In Figure 39 we may observe grossly reduced performance compared with our proposal (we remind the reader that Figure 38 is not a real comparison, as this is the result if the narrowband assumption would hold, which it does not). Thus, for ranging/positioning applications, the reader should compare Figure 37 and Figure 39, and observe that the peak in Figure 37 is much less prone to noise (as it has much higher curvature).

To summarize our findings, we mention that we have discovered a double beamforming effect of RISs in UWB. At first, UWB is problematic for RISs due to the differences in propagation delays. However, by engineering a RIS which mitigates said differences, the drawback is turned into a benefit through the double beamforming effect. Further research is needed to fully draw upon this new phenomenon.

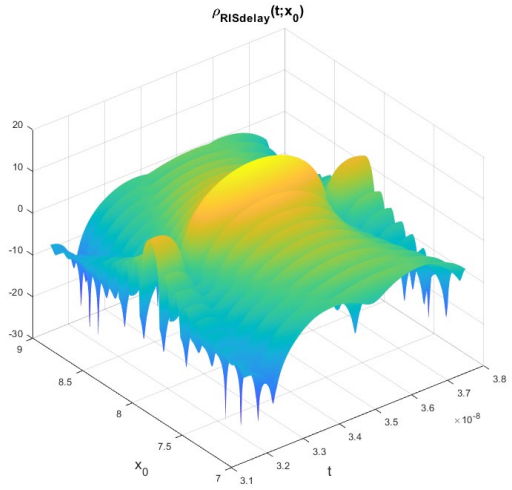

Figure 37. The function $\rho_{RISdelay}(t;x_0)$ for the setup in Figure 36

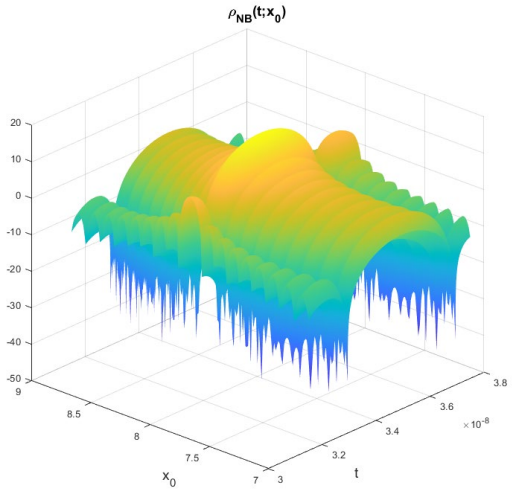

Figure 38. The function $\rho_{NB}(t;x_0)$ for the setup in Figure 36

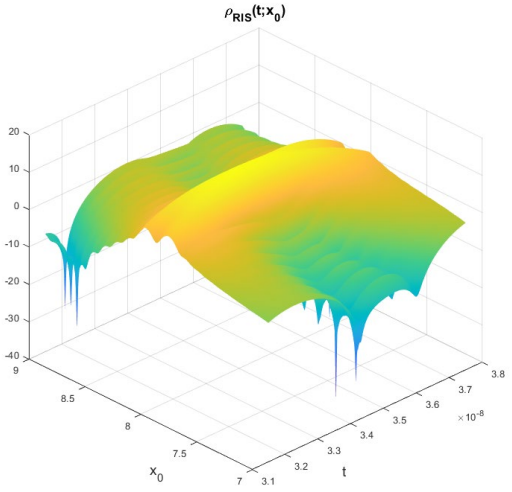

Figure 39. The function $\rho_{RIS}(t;x_0)$ for the setup in Figure 36

7. CONCLUSIONS

Reconfigurable intelligent surface (RIS) is a promising technology to tackle energy efficiency, latency, complexity, and reliability issues in subnetworks. However, it has been shown that the introduction of RISs in subnetworks might lead to several challenges such as the availability of physically-consistent models, signalling overhead, configuration complexity and rate, and the presence of uncontrolled interference both within a subnetwork and between subnetworks, especially if they are uncoordinated.

6G-SHINE has addressed the above issues at modelling, technological, and algorithmic levels by introducing several significant advancements. It developed more sophisticated models for RISs, grounded in multi-port theory, which became the foundation for subsequent analyses and allowed for offline optimization of the RIS, relying solely on statistical knowledge of the channel, thus reducing the required overhead for CSI up to a factor of *N*, i.e., the number of elements of the RIS. The project also developed and validated macroscopic ray-based models for RIS through comprehensive measurement campaigns conducted within WP2. Beyond modelling, novel RIS structures were designed - notably non-diagonal RISs - which offer enhanced flexibility for mitigating interference and support the formation of wide communication beams. Ad hoc optimization approaches were proposed to reduce interference between subnetworks, leveraging the advanced capabilities of non-diagonal RIS. Specifically, it has been found that in the consumer use case 'Indoor interactive gaming', 20-30 dB reduction of interference levels for RIS assisted subnetworks can be achieved with non-diagonal RISs compared to conventional RISs. Moreover, a RIS providing a wide beam is essential for reaching the goal of 20 nodes in the Industrial use case 'Subnetwork Swarm: Coexistence in Factory Hall'.
The project devised and examined optimization strategies aimed at minimizing power consumption while maintaining data rate requirements, particularly in subnetworks featuring multiple RISs and subnetwork elements (SNEs). The studies indicate that a power saving ranging from 5 dB to 60 dB is achievable in the 'Subnetworks Swarms' use case (Industrial subnetworks) while satisfying the target KPIs, when the RIS is properly optimized using the developed models, compared to the scenario where RISs are not present.

Complementing these efforts, new flexible packet coding strategies exploiting the presence of RISs were explored to improve the reliability of communication links. In the Industrial subnetwork use case 'Visual inspection unit', the proposed flexible packet coding strategies provide an approximatively x10 improvement in spectral efficiency. In addition, the activity carried out on RIS technologies and signal processing methodologies has spurred some by-products, initially not foreseen in the project proposal, which could have an impact especially in consumer applications. Specifically, double beamforming effect of RISs when used in conjunction with UWB signals has been discovered and turned from a potential issue into a benefit by properly engineering the RIS so that it can manage around 5 times the bandwidth compared with normal RISs.

REFERENCES

[1] 6G SHINE Project, Work Package 3, Deliverable D3.2 "RIS technologies and models for in-X subnetworks". Available: RIS technologies and models for in-X subnetworks [Accessed: May 28, 2025].

[2] 6G SHINE Project, Work Package 2, Deliverable D2.2 "Refined definition of scenarios, use cases and service requirements for in- X subnetworks". Available: Refined definition of scenarios, use cases and service requirements for in- X subnetworks [Accessed: May 28, 2025].

[3] 6G SHINE Project, Work Package 2, Deliverable D2.3 "Radio propagation characteristics for in-X subnetworks". Available: Radio propagation characteristics for in-X subnetworks [Accessed: May 28, 2025].

[4] European Telecommunications Standards Institute, "Reconfigurable Intelligent Surfaces (RIS); Use Cases, Deployment Scenarios and Requirements" ETSI GR RIS 001 V1.2.1, 2025-02. Online]. Available: [GR RIS 001 - V1.2.1 - Reconfigurable Intelligent Surfaces (RIS); Use Cases, Deployment Scenarios and Requirements. [Accessed: May 22, 2025].

[5] E. M. Vitucci, M. Albani, S. Kodra, M. Barbiroli, V. Degli-Esposti, "An Efficient Ray-Based Modeling Approach for Scattering from Reconfigurable Intelligent Surfaces," *IEEE Transactions on Antennas and Propagation*, vol. vol. 72, no. no. 3, pp. pp. 2673-2685, March 2024.

[6] M. Albani, G. Carluccio, and P.H. Pathak "Uniform Ray Description for the PO Scattering by Vertices in Curved Surface with Curvilinear Edges and Relatively General Boundary Conditions," *IEEE Trans. Antennas Propag.*, vol. 59, no. 5, pp. 1587-1596, May 2011.

[7] E. M. Vitucci, N. Cenni, V. Degli-Esposti, and M. Albani, "Uniform Ray Description for PO Scattering from Reconfigurable Intelligent Surfaces," in Proc. 25th International Symposium on Electromagnetic Theory (URSI-B EMTS 2025), Bologna, Italy, 23-27 June 2025.

[8] TR. 38.867, "Study on NR Network-controlled Repeaters", version 18.0.0, Sept. 23, 2022 [Online]. Available: https://www.3gpp.org/ftp/Specs/archive/38_series/38.867/38867-i00.zip [Accessed: May 22, 2025].

[9] M. Nerini, S. Shen, H. Li, and B. Clerckx, "Beyond diagonal reconfigurable intelligent surfaces utilizing graph theory: Modeling, architecture design, and optimization", *IEEE Transactions on Wireless Communications*, vol. 23, no. 8, pp. 9972-9985, Aug. 2024.

[10] Z. Wu and B. Clerckx, "Beyond diagonal RIS in multiuser MIMO: Graph theoretic modelling and optimal architectures with low complexity", *arXiv preprint https://arxiv.org/abs/2502.16509*. Uploaded Feb. 23, 2025.

[11] F. Rusek, J. Flordelis, E. Bengtsson, K. Zhao, O. Zander, "Spatially selective reconfigurable intelligent surfaces through element permutation" In Proc. IEEE International Conference on Communications (ICC), Denver (CO), 2024.

[12] S. O. Petersson and B. G. Johannisson, "A method of designing weight vectors for a dual beam antenna with orthogonal polarizations," Published by Wipo. International publication number WO 2011/095184 A1, May 2011.

[13] Petersson, Sven O., and Maksym A. Girnyk. "Energy-Efficient Design of Broad Beams for Massive MIMO Systems," *arXiv preprint https://arxiv.org/abs/2012.02768* (2020).

[14] P. Ramezani, M. A. Girnyk, and E. Björnson, "On Broad-Beam Reflection for Dual-Polarized RIS-Assisted MIMO Systems" *arXiv preprint* https://arxiv.org/pdf/2410.07134 . Uploaded Nov. 24, 2024.

[15] X. Wei, D. Shen, and L. Dai, "Channel estimation for RIS assisted wireless communications -part II: An improved solution based on double-structured sparsity," *IEEE Communications Letters*, vol. 25, no. 5, pp. 1403-1407, 2021.

[16] G. Zhou, C. Pan, H. Ren, P. Popovski, and A. L. Swindlehurst, "Channel estimation for RIS-aided multiuser millimeter-wave systems," *IEEE Transactions on Signal Processing*, vol. 70, pp. 1478-1492, 2022.

[17] T. L. Jensen and E. De Carvalho, "An optimal channel estimation scheme for intelligent reflecting surfaces based on a minimum variance unbiased estimator," in *ICASSP 2020 - 2020 IEEE International Conference on Acoustics, Speech and Signal Processing (ICASSP)*, 2020, pp. 5000-5004.

[18] J. Chen, Y.-C. Liang, H. V. Cheng, and W. Yu, "Channel estimation for reconfigurable intelligent surface aided multi-user mm-wave MIMO systems," *IEEE Transactions on Wireless Communications*, vol. 22, no. 10, pp. 6853-6869, 2023.

[19] A. de Jesus Torres, L. Sanguinetti, and E. Björnson, "Electromagnetic interference in RIS-aided communications," *IEEE Wireless Communications Letters*, vol. 11, no. 4, pp. 668-672, 2022.

[20] W.-X. Long, M. Moretti, L. Sanguinetti, and R. Chen, "Channel estimation in RIS-aided communications with interference," *IEEE Wireless Communications Letters*, vol. 12, no. 10, pp. 1751-1755, 2023.

[21] M.-M. Zhao, Q. Wu, M.-J. Zhao, and R. Zhang, "Intelligent reflecting surface enhanced wireless networks: Two-timescale beamforming optimization," *IEEE Transactions on Wireless Communications*, vol. 20, no. 1, pp. 2-17, 2021.

[22] F. Jiang, A. Abrardo, K. Keykhosravi, H. Wymeersch, D. Dardari, and M. Di Renzo, "Two-timescale transmission design and RIS optimization for integrated localization and communications," *IEEE Transactions on Wireless Communications*, vol. 22, no. 12, pp. 8587-8602, 2023.

[23] A. Abrardo, A. Toccafondi, and M. D. Renzo, "Analysis and optimization of reconfigurable intelligent surfaces based on s-parameters multiport network theory," *IEEE Transactions on Wireless Communications*, November 2024.

[24] J. Hoydis, S. ten Brink, and M. Debbah, "Massive MIMO in the UL/DL of cellular networks: How many antennas do we need?" *IEEE Journal on Selected Areas in Communications*, vol. 31, no. 2, pp. 160-171, 2013.

[25] T. Demir, E. Björnson, and L. Sanguinetti, "Channel modeling and channel estimation for holographic massive MIMO with planar arrays," *IEEE Wireless Communications Letters*, vol. 11, no. 5, pp. 997-1001, 2022.

[26] E. Björnson and L. Sanguinetti, "Rayleigh fading modeling and channel hardening for reconfigurable intelligent surfaces," *IEEE Wireless Communications Letters*, vol. 10, no. 4, pp. 830-834, 2021.

[27] Mao, W., Yeh, S.-P., Zhu, J., Nikopour, H., & Talwar, S. (n.d.). Delay-optimal linear packet-level coding for URLLC on multi-path wireless networks. Intel Corporation, Santa Clara, United States.

[28] 6G SHINE Project, Work Package 3, Deliverable D3.1 "Preliminary results on PHY and MAC enablers for in-X subnetworks". Available: Preliminary results on PHY and MAC enablers for in-X subnetworks [Accessed: May 28, 2025].

[29] 3GPP. (2018). Study on channel model for frequency spectrum above 6 GHz (3GPP TR 38.900 V15.0.0).

[30] B. Sihlbom, M. I. Poulakis, and M. Di Renzo, "Reconfigurable intelligent surfaces: Performance assessment through a system-level simulator," *IEEE Wireless Commun.*, vol. 30, no. 4, pp. 98-106, 2022.

[31] Y. Yuan, Y. Huang, X. Su, B. Duan, N. Hu, and M. Di Renzo, "Reconfigurable intelligent surface (RIS) system level simulations for industry standards," *arXiv preprint:* https://arxiv.org/abs/2409.13405 (2024).

[32] A. Albanese, F. Devoti, V. Sciancalepore, M. Di Renzo, and X. Costa- Perez, "Marisa: A self-configuring metasurfaces absorption and reflection solution towards 6G," in IEEE INFOCOM 2022 - IEEE Conference on Computer Communications, 2022, pp. 250-259.

[33] M.Najafi, V.Jamali, R.Schober, and H.V.Poor, "Physics-based modeling and scalable optimization of large intelligent reflecting surfaces," *IEEE Trans. Commun.*, vol. 69, no. 4, pp. 2673-2691, 2021.

[34] A. Abrardo, D. Dardari, and M. Di Renzo, "Intelligent reflecting surfaces: Sum-rate optimization based on statistical position information," *IEEE Trans. Comm.*, vol. 69, no. 10, pp. 7121-7136, July 2021.

[35] G. Bartoli, A., N. Decarli, D. Dardari, M. Di Renzo, "Spatial multiplexing in near field MIMO channels with reconfigurable intelligent surfaces," *IET Signal Processing*, 23 March 2023.

[36] FIRA Consortium, "The Ultra-Wideband Revolution for Transport Fare Collection", July 2023. [Online]. Available: https://www.firaconsortium.org/sites/default/files/2023-07/the-ultra-wideband-revolution-for-transport-fare-collection-july-2023.pdf [Accessed: May 22, 2025].